Seismic tomography for velocity and attenuation model reconstruction

Ying Rao *B.E., M.Sc.*

Submitted for a degree of Doctor of Philosophy of Imperial College London

July 2007

Centre for Reservoir Geophysics
Department of Earth Science and Engineering
Imperial College London

Abstract

Seismic tomography becomes an effective tool for determining wave velocities in the presence of lateral velocity variations. In crosshole seismic tomography, waveform tomography attempts to use the first arrival wavelets, transmitted and scattered energy in the recorded seismic data to reconstruct a velocity model. It gets rid of the assumption of asymptotic rays in traveltime tomography and exploits more data information.

The generation of an initial model for waveform tomography is an essential requirement. Traveltime tomography is used to build the initial velocity model for waveform tomography, since it is typically more robust, easier to implement, and computationally much cheaper than waveform tomography. For the traveltime inversion of crosshole seismic data, I present some working solutions to the following three issues related to the real data application: how to suppress the effect of data errors, how to balance the data contribution and a reference model, and how to properly set the geological constraint in an inversion.

Waveform tomography is implemented in the frequency domain. Compared to a time-domain version, the frequency-domain version enables the use of distinct frequency components to adequately reconstruct the subsurface velocity field, and thereby dramatically reduces the input data quantity required for the inversion process. For real data application, I have found that the following three issues are essential. (a) A good initial model is necessary for waveform tomography. As real data are often band limited with missing low frequencies, we need a good initial model to fill in the gap of low frequencies before the inversion of available frequencies. (b) A group of frequencies should be used simultaneously at each iteration, to suppress the effect of data noise in the frequency domain. (c) A smoothness constraint on the model is also needed in the inversion, to cope with the effect of uneven distribution of ray coverage, and the effect of strong sensitivities to short wavelength model variations.

As for all geophysical inversions, it is important to make a quality assessment of the reconstructed model, to identify which parts of the model are well-resolved and can confidently be used for geological interpretation. I use checkerboard tests to provide a

quantitative assessment of the performance of waveform tomography and the reliability of the inverted velocity model. Such tests can also act as a guide for designing appropriate inversion strategies.

In this thesis, I use waveform tomography to invert for not only the velocity model but also the attenuation model, and to investigate the attenuation effect caused by fracture distribution. I have shown that location of strong attenuation closely correspond to the location of high fracture density. When the fracture size is much smaller than the wavelength, the apparent attenuation anomalies are elliptical in sharp. The attenuation factor is sensitive to both fracture length and fracture orientation. When the length of fracture increases, the attenuation is enhanced. When the fractures are parallel to the source/receiver string, they act as small reflection subsurfaces in seismic response. Parallel fractures produce the strongest attenuation in the results of crosshole waveform tomography. When fractures are perpendicular to the source/receiver string, they act as scattering points in the seismic response. They show weaker apparent attenuation in the results of crosshole waveform tomography.

Acknowledgement

I would like to express my deep and sincere gratitude to my supervisor, Professor Yanghua Wang. His wide knowledge and his logical way of thinking have been of great value for me. I am deeply grateful to his guidance, his detailed and constructive comments, and his important support throughout this work.

I would like to acknowledge the sponsors of the Centre for Reservoir Geophysics, Imperial College London, for supporting my PhD studies. I also acknowledge the funding of the Janet Watson Scholarship, and the partial funding of the Overseas Research Scholarship.

I am grateful to Professor Mike Warner and Dr Joanna Morgan for their constructive suggestion. I am also grateful to Dr Iven Štekl for his valuable advice and friendly assistance. Their extensive discussions around my work have been very helpful for this study.

I would also like to give special thanks to my colleagues in the Centre of Reservoir geophysics of Imperial College London for their comradeship and encouragement. Thanks to Shoudong, Xiaolin, Fiona, Cao, Nasher, Feng and Di for creating an amiable and supportive working environment, for their helpful discussion in group meeting, and for their essential assistance in reviewing part of the patient file of this study.

Finally, I dedicate this thesis to my parents. I am grateful to my parents for the support in the last three years I have had from them.

Contents

List of figures

Chapter 1

Introduction and review

1.1 Introduction

Seismic tomography, which is an effective tool for determining wave velocities in the presence of lateral velocity variations, attracts many geophysicists and mathematicians devoting to this research area. In seismic tomography, traveltime inversion is an early inversion approach which attempts to use wave arrival times to construct a velocity distribution of the region of the survey. However, the recorded seismic data not only contain information on transmitted energy but also scattered energy, which is not utilized in traveltime inversion. Therefore, waveform tomography attempts to get rid of the assumption of asymptotic rays and to make use of all of the data information.

The researches of waveform tomography include two parts. One is forward modelling the propagation of seismic waves and the other is waveform inversion inverting for the subsurface velocity distribution. For waveform inversion, the frequency-domain version enables the use of distinct frequency components and thereby reduces the quantity of data required for processing (Sirgue and Pratt, 2004). It emerges as an efficient imaging tool, capable of being used on a production basis for practical problems.

In this thesis, I will start with investigation of traveltime inversion on real crosshole seismic data, so that I will have a reliable initial estimate for the subsequent waveform tomography. Then I discuss issues and working solutions of waveform tomography for real seismic data. These issues related to real crosshole seismic data include (a) limited frequency band, (b) low signal-to-noise ratio, and (c) uneven distribution of ray coverage. When I obtain the velocity image from waveform tomography, I will estimate the reliability of the result by analyzing the resolution of waveform tomography. Finally, I will use waveform tomography to investigate the attenuation effect caused by fracture distribution.

1.2 Traveltime tomography

Although I will focus on waveform tomography in this thesis, I also need to consider traveltime tomography in crosshole seismic, as it provides a reliable initial model for the further waveform tomography. Traveltime tomography is one effective way to determine wave velocity in exploration seismic for it is typically robust, easy to implement, and computationally inexpensive (Worthington, 1984; Bording *et al.*, 1987).

Seismic traveltime inversion for velocity structure is a nonlinear problem since seismic rays, acting as the integral paths in a tomographic inversion, depend also on the medium velocity. To model practical physical phenomena, the ray path is calculated by ray-tracing in the reference model. Virieux and Farra (1991) described a shooting method for the two point ray-tracing problem by treating it as an initial value problem, with a specified starting path point and trial propagation direction, and then iteratively adjusting the propagation direction until the target end point is reached as Figure 1.1a shown. The main problem with this approach is that determination of a two-point ray within a single ray history is usually a trivial task. Sneider and Spencer (1993), Wang and Houseman (1994, 1995), among many others, solved this problem method by bending method. The bending method, as Figure 1.1b shown, determines the ray path by iteratively perturbing an initial path estimate with two fixed end-points until it satisfies the ray equations. However, although bending methods are fast, they are ill-suited for reliably calculating multi-valued traveltimes.

Instead of determining the unknown ray paths and the unknown velocity structure simultaneously, an iteratively linearized solution is to solve for the model perturbation rather than the model parameters directly (Bording *et al.*, 1987). If the model perturbations are small enough, one can then consider the relationship between the model perturbation and the corresponding residual to be linear. Once the model perturbations have been found, they are added to the current model to produce the model for the following iteration until result converges.

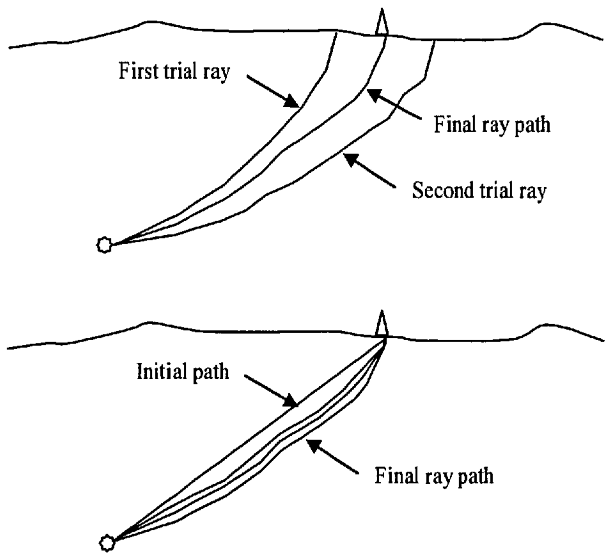

Figure 1.1 (a) The shooting method determines the ray path by treating it as an initial value problem, with a specified starting path point and trial propagation direction, and then iteratively adjusting the propagation direction until the target end point is reached. (b) The bending method determines the ray path by iteratively perturbing an initial path estimate with two fixed end-points until it satisfies the ray equations.

In practice, seismic data always contain a considerable amount of noise. For traveltime data, finite reading precision is a main source of data errors. To reduce the errors, one pre-processing method is to average the traveltime data from similar ray paths (Röhm *et al.*, 2000), but this method may only work on teleseimic tomography as the errors are relatively small compared to the actual traveltime data. To mitigate the data errors, Wang *et al.* (2000) winnowed the noisy data using a locally weighted regression to get rid of the outliers or down-weight the large picking errors. To reduce the effect of data errors during the inversion, Scales *et al.* (1988) used weighting coefficients as the function of the traveltime residual in an iteratively reweighted least-squares scheme. Such residual-based weights however are subjective, since the data errors in practice might be non-Gaussian distributed and thence the data residual might be biased. The observation from real crosshole seismic data, as shown in Chapter 2, indicates that the real data signal-to-noise ratio is likely depending on the vertical offset between a source and a receiver and then, logically enough, I suggest set the weight based on the vertical offset, a reflection of our confidence in the accuracy of picked traveltime. This idea is similar to Berryman's (1989) scheme, in which a smaller weight was given to the long ray path that is affected by many different pixel slownesses (inverse velocities).

In geophysical applications, sources and receivers can rarely be placed on all sides of the imaging region, resulting in some subregions having very poor ray coverage. Under these circumstances, one of the practical solutions is obtained by applying additional constraints to the inverse problem, e.g., upper and lower limits of reconstructed velocities (van Wijk *et al.*, 2002). It involves searching for a solution that not only satisfies the data but also is "close", in some adjustable sense, to some initial model that must be specified.

There are number of methods to solve traveltime inversion problem. An algebraic reconstruction technique (ART) (Herman *et al.* 1973, Mason 1981, Peterson *et al.* 1985) is an early developed method, which is row action method. Developed from the ART, the simultaneously iterative reconstruction technique (SIRT) (Dines and Lytle, 1979; Gilbert 1972, Ivansson 1983) is updated only after all equations have been processed. Conjugate gradient method is also widely applied to traveltime tomography (Gersztenkorn *et al.*, 1986; Scales, 1987).

The researches on traveltime tomography are extended from 2-D to 3-D (Washbourne *et al.*, 2002). The researches on traveltime tomography are also extended to include anisotropy (Chapman and Pratt, 1992; Pratt and Chapman, 1992; Wu and Lees, 1999; Alkhalifah, 2002; Slawinski *et al.*, 2004). On the other hand, many researches try to incorporate other seismic information into recent algorithms in order to avoid the high frequency assumption and first break picking (Luo and Schuster, 1991; Bergman *et al.*, 2004).

1.3 Waveform tomography

Full wave theoretical techniques aim to make use of all the information in the wavefield and therefore to deal with more complicated structure at higher resolution (Mora, 1989; Pratt and Goulty, 1991).

The research works are divided into two parts. One is modelling the propagation of seismic waves and predicting the response at seismic receivers. The other is looking for the subsurface model that fits the real data.

1.3.1 Forward modelling

Modelling the propagation of seismic waves and predicting the response at seismic receivers is an essential step in the interpretation or, formal inversion, of data from seismic experiments.

Wave-equation-based numerical methods begin from the late 1960's. Theories of wave propagation are produced in the early works. But these works are limited to simple cases. To deep understand the wave propagation in the media, some numerical methods are used in forward modelling, such as Finite Element Method (FEM), Boundary Element Method (BEM) and Finite Difference Method (FDM). Using those numerical methods, the arbitrarily shaped objects and the complex material can be flexibly handled.

The wave equation modelling has been divided into two methods that work in the time and frequency domains respectively. The time domain is like the trace on an oscilloscope where the vertical deflection is the signal amplitude, and the horizontal deflection is the time variable (Virieux, 1986; Lavander, 1988; Juhlin, 1995). Time domain method is suitable if the full time domain seismic section for a single source or for a small number of sources. Frequency domain is like the trace on a spectrum analyser, where the horizontal deflection is the frequency variable and the vertical deflection is the signals amplitude at that frequency (Song and Williamson, 1995).

The forward modelling is implemented in one-dimension (1-D) condition at the beginning. Then it has been extended to two-dimensions (2-D) to gain qualitative understanding of wave propagation processes. This method includes an assumption that the source extends infinitely in the out-of-plane direction and results in waveforms and amplitude behaviour which differ significantly from those for true point sources (Song and Williamson, 1995). This source mismatch due to the modelled wavefield, is inconsistent with the observed data. For crosshole data, the source and receivers are restricted to a plane. Pratt (1990a) proposed a 2.5D finite difference modelling method, which started from the 3D acoustic wave equation, and performed a spatial Fourier transform in the out-of-plane direction. Song and Williamson (1995) used a Fourier transform with respect to the out-of-plane coordinate to reduce the problem of modelling in 3D to repeatedly solving a 2D equation, which they accomplished using finite differences. As a result of advances in computer technology, some researchers have been able to carry out full 3-D finite difference modelling for realistic (but small) models. For example, Yoon and McMechan (1992) modelled waves in and around a single borehole. However, the computational requirements are still extreme.

To realise forward modelling, choice of boundary condition is one critical problem in forward modelling. Generally, a limited area should be chosen for forward modelling of wave propagation in the earth. The boundaries of this limited area will bring significant reflections back into the computational domain, as shown in Figure 1.2. Generally, an artificial boundary is used to keep computation down to a manageable size and the reflections are undesirable. Actually, the wave should only propagate outward near the boundary, as shown in Figure 1.3. Therefore, some boundary conditions that simulate the outward radiation of energy should be set. Depending upon the problem, following boundary conditions are generally used on the edges: absorbing boundary conditions for simulating an infinite medium, stress-free condition (free-surface), or zero-velocity conditions equivalent to zero-displacement conditions (rigid-surface) etc.

Absorbing boundary condition may be generally implemented in three ways. A standard absorbing boundary condition is radiation condition, based on one-way wave equation, which is the second-order condition, derived by Clayton and Engquist (1977). This boundary condition is based on a paraxial approximation. Along the boundary, the wave can outward-moving in the condition of the grid "transparent". (Clayton and Engquist, 1977; Stacey, 1988). Then, the accuracy of these boundary conditions can be increased by simply taking higher-order paraxial approximations. An alternative approach is the sponge boundary condition, based on absorbing layers. In this method, seismic waves inside the artificial boundary are attenuated by a gradual reduction of amplitudes. Shin (1995) realised this method in frequency domain modelling. Perfectly matched layer (PML) is developed by Berenger (1994). This method has been proved to be efficiently absorbing reflection energy over a wide range of angles and is insensitive to frequency, compared with other two methods (Komatitsch and Tromp, 2003). This method has been applied to wave propagation by Qi and Geers (1998), Hasting et al. (1996) and Komatitsch and Tromp (2003).

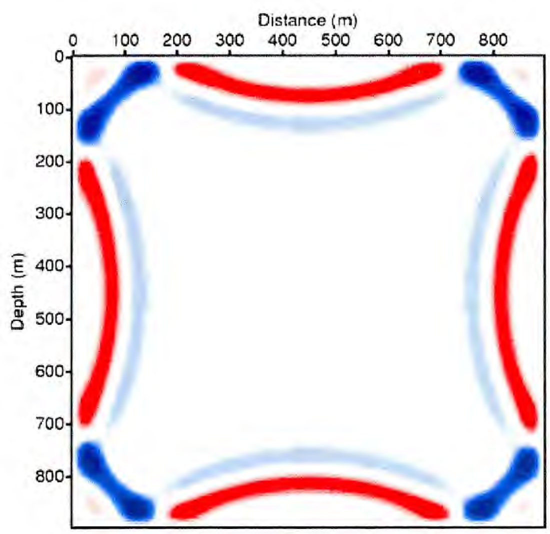

Figure 1.2 Snapshot from forward modelling in limited area with setting rigid boundary condition. Significant reflection is back toward the computational domain.

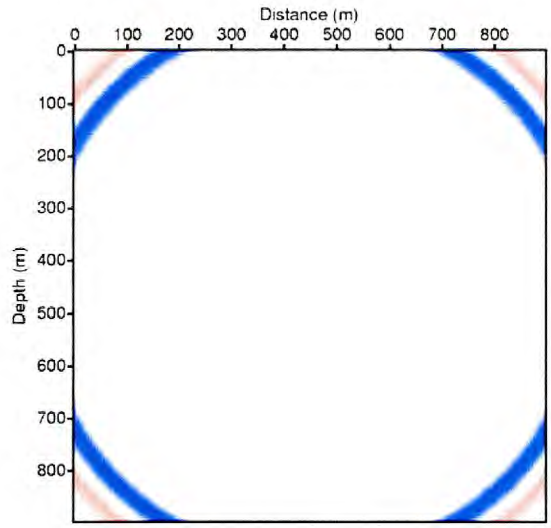

Figure 1.3 Snapshot from forward modelling in limited area with setting absorb boundary condition. The wave should propagate outward near the boundary.

To improve the resolution of forward modelling, one choice is to use a higher-order accurate operator. However, the higher-order will increase the computational expense and the memory requirement. Fortunately, Štekl and Pratt (1998) used rotated operators to improve the accuracy and efficiency of 2D isotropic, frequency-domain seismic modelling extended to the viscoelastic case. They use a differencing operator in a rotated coordinate frame and a lumped mass term, which are combined with ordinary second order finite-difference operators in an optimal manner. Using these two operators, the resulting second-order differencing scheme is no more expensive than an ordinary second-order differencing scheme. Furthermore, the number of grid points required per smallest wavelength is approximately 4, instead of approximate 15 in the conventional method. This improvement makes frequency domain forward modelling more attractive.

To model increasingly general physical phenomena, Song *et al.* (1995) successfully model wave propagation using the acoustic wave equation. Pratt (1990a) has realized forward modelling of the elastic wave equation. Then Štekl and Pratt (1998) extended it to visco-elastic wave equation. All these methods are in frequency domain.

The wave propagation is also carried out in the time domain by acoustic wave equation (Clayton and Engquist, 1977). Lavander (1988) and Juhlin (1995) use a staggered-grid approach to elastic wave equation. This formulation became dominant (Virieux, 1986) for time domain schemes, due to the fact that it was the only known scheme that enabled the simulation of elastic waves in models with liquid-solid interfaces (Kerner, 1990). Based on these works, the wave propagation in complex materials can be simulated. Vlastos et al. (2003) simulate wave propagation in media with distribution of discrete fractures. Hong and Kennett (2004) model the wave propagation in media with a random distribution of fluid-filled cavities. Vlastos et al. (2006) test the effect of pore pressure in a fracture network for wave propagation. These works are very helpful for understanding the complicated nature of seismic wave propagation in complex media.

1.3.2 Waveform inversion

In exploration geophysics the main problem is not to model the data but to find the model which "fit" the data collected at the site. Waveform inversion seeks to reconstruct the earth model parameters, e.g. velocity and density, from the waveform data.

(1) *Waveform tomography versus travel time tomography*

Waveform inversion takes account of all acoustic wave modes automatically. No travel time picking or sophisticated data processing (such as wavefield separation) is required. In conventional traveltime inversion method, first arrival traveltime may be difficult to pick due to a significant amount of noise in the data (Wang *et al.* 2000). Even in the cases where there is no significant noise problem, the picked first arrival traveltimes are subjective to some extent. It is not a directly recorded parameter. The consistency of the picks may be systematically affected by subjective choices. On the other hand, the data used in wavefield inversion are directly measured. There is no subjective transformation involved in the processing which will affect the data (Pratt and Shipp 1999).

(2) *Waveform tomography in the frequency domain*

Waveform tomography can be applied in the time domain (Tarantola, 1986; Mora, 1987; Bunks et al., 1995; Shipp and Singh, 2002) and in the frequency domain (Pratt and Worthington, 1990; Liao and McMechan, 1996; Sirgue and Pratt, 2004). Compared with time domain methods, the frequency domain method is more efficient. Marfurt (1984) pointed out that the frequency domain method is particularly suitable for finite-difference/finite-element modelling with multi-source. Once the response is calculated for first source, there is little extra cost for additional sources. Because only one frequency component is inverted at a time, the inversion is efficient. It is also convenient to accomplish the strategy of using gradually low to high frequency components. Because low frequency data are more linear with respect to the model perturbations than high frequency data, using progressively low to high frequency components makes the frequency domain method more suitable for wide-band inversion (Sirgue and Pratt, 2004).

The gradient method, which avoids the expensive inversion of large matrices, is generally used in waveform inversion to obtain the minimization of residuals. Through repeated calculation of the local gradient, the direction of minimization of the objective function is formed. This descent direction can lead to the objective function being zero in ideal conditions. Lailly (1984) and Tarantola (1984) have done important works for waveform inversion by posing that the steepest descent direction for the inverse problem could be calculated without computing the partial derivatives explicitly. Through their method, the gradient of the misfit function could be computed by "back-propagating" the data residuals and correlating the result with forward-propagated wavefield (Pratt et al., 1998). Then this method has been applied in frequency domain by Pratt and Worthington (1990) and Song et al. (1995). In these methods, because conjugate gradient method has quadratic convergence, it is generally used to accelerate the convergence speed. But it still takes a significant number of iterations before quadratic convergence is established. Fortunately, Newton algorithms, such as Gauss-Newton method and full Newton method (Santosa, 1987), which has been feasible to implement by the developments in computer technology, has more rapid convergence, particularly during the early stage of iterative inversions (Tarantola and Valette, 1982; Pratt *et al.*, 1998). Sheen et al (2006) present an inversion example based on the Gauss-Newton method in the time domain. Hicks and Pratt (2001) present an inversion example based on the Gauss-Newton method.

Another way to directly reduce calculation expense is to select a few frequencies to yield the result, representative of all frequencies. This method can be realised in frequency domain because the frequency domain inversion has the ability to provide an unaliased image using a very limited number of frequencies (Pratt and Worthington, 1988; Liao and McMechan, 1996; Sirgue and Pratt, 2004). Pratt (1990b) has observed that large aperture seismic surveys could be inverted effectively using only a limited number of frequency components. Based on the that larger offset data require fewer frequencies components, Sirgue and Pratt (2004) showed that frequency-domain inversion of the Marmousi data example using only a few frequencies could yield a result which is comparable to full time-domain inversion. Brenders and Pratt (2007) employ this strategy with real data. Their results, using four carefully selected frequency components, are nearly equivalent to the results obtained, using 57 frequency components. The computation time is reduced 88.3 per cent.

Full wavefield information is used in the inversion so that the method combines the advantages of (qualitative) migration and (quantitative) tomography. The frequency domain method can obtain generally higher resolution than that from the travel time tomography. The optimum resolution is half a wavelength, relative to the chosen frequency, which can be higher than the dominant frequency (Pratt and Worthington, 1990).

To improve resolution of waveform inversion, Shin and Min (2006) present a logarithmic method to compute the steepest-descent direction by the back-propagation. The wavefield obtained by dividing the logarithm of the ratio of the modelled data to the measured data by the modelled wavefield is used, instead of back-propagating the residuals between the measured and modelled data in conventional method. In this method, the objective function can be separated to preferentially match the amplitude, phase or both amplitude and phase respectively. Some synthetic examples, with and without noise, show the advantage of this method.

Estimating the low-wavenumber "background" velocity in the inversion of seismic-reflection data is a classic problem. It has been investigated by Mora (1989), Cao *et al.* (1990) and Varela *et al.* (1996). Pratt *et al.* (1998) illustrate the use of the Newton method to solve this problem effectively. The inversion procedure includes two steps for the high and low wavenumbers of velocity. In each iteration of the inversion procedure, the reflectors are inverted by using the back-propagation method first. Then background velocities are inverted by using a much smaller number of parameters using the Newton method. By careful parameterization of the problem, either the high or the low model wavenumbers case can be inverted by using both local descent method and a single waveform misfit criterion (Hicks and Pratt, 2001). In the example, presented by Hicks and Pratt (2001), background velocities and reflectors have been recovered correctly.

Frequency-domain waveform tomography can easily be adapted to include the attenuation effect. To do so, we may simply replace the real-valued velocities with complex velocities and do not add more calculation expense. The acoustic attenuation factor has been introduced in both the Conjugate gradient method (Song et al., 1995) and the Newton method (Hicks and Pratt, 2001). The factor corresponds with regions of increased fracturing. These regions may have acted as gas migration pathways.

1.4 Overview of chapters in this thesis

This thesis begins with the generation of a synthetic initial model for waveform tomography, which is an essential requirement to reduce nonlinear effects in waveform inversion. Hence in chapter 2, following this introductory chapter, I use a traveltime tomography approach, which is typically much more robust, easier to implement, and computationally much cheaper, to build the initial velocity model for future waveform tomography. I document working solutions to the following three issues in the traveltime inversion related to real data application: how to suppress the effect of data errors, how to balance the data contribution and a reference model, and how to properly set the geological constraints in an inversion.

After I get a reliable initial model for waveform tomography, I move to waveform tomographic techniques in Chapter 3. I demonstrate the inversion of a real seismic dataset. I document the following three steps before the waveform inversion of crosshole seismic tomography with real data: pre-processing the field data in order to force the inversion to fit the critical constraints on the low and intermediate wavenumbers in the model, spectral analysis for choosing the optimum frequency bands, and traveltime inversion obtain an initial velocity model. For real data inversion, in order to mitigate the effect of data noise, I invert a group of frequencies simultaneously at each inversion stage. The result is much better than that obtained by using single frequencies. Using this scheme, I combine sonic logging velocities and the velocity field obtained from the travel time tomography to constrain the initial model in the waveform inversion. The results achieved have shown clear improvement of the vertical resolution, compared to the traveltime result.

As for all inversions of geophysical data, it is important to make an assessment of the final model, to determine which parts of the model are well-resolved and can confidently be used for geological interpretation. Hence, in chapter 4, I use checkerboard tests to provide a quantitative estimate of the performance of the inversion and the reliability of the final velocity model. I use the output from the checkerboard tests to determine resolvability across the velocity model. Such tests can act as good guides for designing appropriate inversion strategies. Here I discovered that, by including both reference-model and smoothing constraints in initial inversions, and then relaxing the smoothing constraint for later inversions, an optimum velocity image was obtained. Additionally, I noticed that the performance of the inversion was dependent on a relationship between velocity perturbation and checkerboard grid-size: larger velocity perturbations were better solved when the grid-size was also increased. My results suggest that model assessment is an essential step prior to interpreting features in waveform tomographic images.

In chapter 5, I use waveform tomography to invert also for the attenuation model. Frequency domain waveform tomography can easily include the attenuation in calculation. Because the magnitude of attenuation factor on average is equal to 0.01, a starting model with constant value 0 for the attenuation factor, is a safe choice for waveform inversion. It is suitable in the case of real data to invert for the real-part of the velocity model by fixing the attenuation factor model first, and then fixing the real-part of the velocity model to invert for attenuation, because the real part velocity and attenuation factor have different magnitude and different weights of contribution in the objective function. The strategy of alternately fixing one part of the model and inverting for the other part can successfully avoid the effect of the trade-off of two parameters of different magnitude.

In chapter 6, I use waveform tomography to investigate the attenuation effect caused by fracture distribution. The attenuation factor is sensitive to both fracture length and fracture orientations. When the typical length of fracture increases, the attenuation is enhanced. When the fractures are parallel to the source/receiver string, they act as small reflecting surfaces in seismic response and they cause the strongest attenuation in the results of waveform tomography. When fractures are perpendicular to the source/receiver string, they act as scattering points in the seismic response and show the weakest attenuation in the results of waveform tomography.

Finally, conclusions of the thesis are given in Chapter 7. Possible further research topics are also discussed in this chapter.

Chapter 2

Traveltime inversion with working solutions to the practical issues

2.1 Introduction

Traveltime tomography is needed for a reliable initial model for waveform tomography. Traveltime tomography attempts to use the first arrival times to reconstruct a velocity distribution in the region of the survey. However, the objective function is nonlinear. In this chapter, I start with a simple derivation from a nonlinear inversion objective function to a linearized inverse equation, so as to recap the physical meaning of the following three parameters in an inverse problem: (a) a data covariance matrix, denoted as $\mathbf{C}_\mathrm{D}^{-1}$, (b) a trade-off parameter μ, and (c) a model covariance matrix denoted as $\mathbf{C}_\mathrm{M}^{-1}$. Keeping their physical meaning in mind, then I attempt to offer a working definition for each of these three parameters, which are sometime mathematically tedious in the inverse theory.

The material in chapter 2 has been published in *Journal of Geophysics and Engineering*, 2005, Vol. **2**, 139-146.

2.2 Linear inverse problem

The least-squares inverse problem is to infer a model that minimizes the difference between the theoretical prediction and the observed data set, and meanwhile, is close to a reference model. The objective function is given as (Tarantola, 2005)

$$J(\mathbf{m}) = [f(\mathbf{m}) - \mathbf{d}]^\mathrm{T} \mathbf{C}_\mathrm{D}^{-1} [f(\mathbf{m}) - \mathbf{d}] + \mu(\mathbf{m} - \mathbf{m}_0)^\mathrm{T} \mathbf{C}_\mathrm{M}^{-1} (\mathbf{m} - \mathbf{m}_0), \qquad (2.1)$$

where $\mathbf{m}$ is the model vector, $f(\mathbf{m})$ is the forward prediction, $\mathbf{d}$ is the vector of the observed data set, $\mathbf{C}_{\mathrm{D}}$ is called the data covariance matrix with physical units of $(data)^2$, $\mathbf{m}_0$ is a reference model, $\mathbf{C}_{\mathrm{M}}$ is called the model covariance matrix with units of $(model\ parameter)^2$, and the scalar μ is a trade-off parameter that controls the relative weights of the data contribution and the reference information. In this chapter, I choose start model as the reference model $\mathbf{m}_0$.

To solve this minimization problem by setting $\partial J / \partial m_j = 0$, for $j = 1, 2, \ldots N$, I obtain

$$\mathbf{G}^{\mathrm{T}}\mathbf{C}_{\mathrm{D}}^{-1}[f(\mathbf{m})-\mathbf{d}]+\mu\mathbf{C}_{\mathrm{M}}^{-1}(\mathbf{m}-\mathbf{m}_0)=0, \tag{2.2}$$

where $\mathbf{G} = \nabla_{\mathbf{m}} f(\mathbf{m})$ is the matrix of the Fréchet derivatives of the forward modelling $f(\mathbf{m})$ with respect to the model parameters $\mathbf{m}$. For ray-based travel time modelling,

$$f(\mathbf{m})=\mathbf{A}\mathbf{m}, \tag{2.3}$$

where $\mathbf{A}$ is the $M \times N$ matrix with element a_{ij} denoting the ray length of the i-th ray in the j-th cell of a subdivision of the model space, and $\mathbf{m}$ is the N-vector whose element m_j is the slowness (inverse velocity) in the j-th cell. Therefore, I have

$$\mathbf{A}^{\mathrm{T}}\mathbf{C}_{\mathrm{D}}^{-1}[\mathbf{A}\mathbf{m}-\mathbf{d}]+\mu\mathbf{C}_{\mathrm{M}}^{-1}(\mathbf{m}-\mathbf{m}_0)=0. \tag{2.4}$$

As the ray path that constitutes matrix $\mathbf{A}$ in equation (2.3) is also model $\mathbf{m}$ dependent, traveltime inversion (2.4) is a non-linear problem. Given a perturbation to the model, i.e. $\mathbf{m} = \mathbf{m}_0 + \delta\mathbf{m}$, equation (2.4) becomes

$$(\mathbf{A}^{\mathrm{T}}\mathbf{C}_{\mathrm{D}}^{-1}\mathbf{A}+\mu\mathbf{C}_{\mathrm{M}}^{-1})\delta\mathbf{m}=\mathbf{A}^{\mathrm{T}}\mathbf{C}_{\mathrm{D}}^{-1}[\mathbf{d}-\mathbf{A}\mathbf{m}_0], \tag{2.5}$$

where $\delta\mathbf{m}$ is the vector of model perturbation (slowness updating) and can be given explicitly as the following linear solution

$$\delta\mathbf{m}=\left(\mathbf{A}^{\mathrm{T}}\mathbf{C}_{\mathrm{D}}^{-1}\mathbf{A}+\mu\mathbf{C}_{\mathrm{M}}^{-1}\right)^{-1}\mathbf{A}^{\mathrm{T}}\mathbf{C}_{\mathrm{D}}^{-1}\delta\mathbf{d}, \tag{2.6}$$

and $\delta \mathbf{d} \equiv \mathbf{d} - \mathbf{A}\mathbf{m}_0$ is the vector of data residual. In this chapter, I solve this linear equation using a conjugate gradient method.

The simple derivation summarized in this section shows clearly that the three parameters, $\mathbf{C}_\mathrm{D}^{-1}$, μ and $\mathbf{C}_\mathrm{M}^{-1}$, in the linear equation (2.6) are from the non-linear inversion objective function (2.1). Thus, each of these three parameters in the linear equation (2.6) has an explicit physical meaning: (a) $\mathbf{C}_\mathrm{D}^{-1}$ is the data covariance matrix, (b) μ is the trade-off parameter, and (c) $\mathbf{C}_\mathrm{M}^{-1}$, the model covariance matrix. In the following three sections, I attempt to provide a working definition to each of them, associated with real data applications of crosshole traveltime tomography.

2.3 Description of seismic data

The dataset was acquired from two boreholes of Shengli Oilfield in China. The real seismic dataset was acquired from two parallel boreholes 300 meters apart. The borehole penetrate a sequence of alternating mudstones and sandstones, which are horizontally layered thin-sheet lake-environment sedimentary, and igneous rock at bottom. A string of 58 hydrophone receivers at 1.52 meter spacing was placed in one borehole. Small explosive charges were fired successively in the other borehole at 0.38 meters intervals. Coverage was then extended by repositioning the hydrophone string in the receiver borehole, with one receiver position overlap for tying, and repeating the shot sequence. The triggering signal for the seismograph was obtained by wrapping a wire around the end of the detonator. This blows open-circuit when the shot was fired, providing an accurate time break.

There are total of 378 shot positions at the well No. 1 (Luo151-1), ranging in depth from 2399.4 m to 3073.9 m, and 350 receiver positions at the well No. 2 (Luo151-11), ranging from 2397.9 m to 2908.5 m. For experiments in this chapter, the actual solution domain is from 0 to 300 m in the x direction and 2,490 to 3,030 m in the z direction. In the ray-based tomographic inversion, I divide it into 100×180 cells with cell size of 3 m.

2.4 Suppressing the effect of data errors

In this section, I attempt to suppress the effect of data errors in the least-squares problem, by defining a so-called confidence matrix pragmatically, i.e. a working solution for the inverse of data covariance matrix, $\mathbf{C}_D^{-1}$.

When I seek a model **m** that minimizes the difference between the theoretical prediction $f(\mathbf{m})$ and the observation $\mathbf{d}$ in a least-squares sense, the objective function is given as

$$J(\mathbf{m}) = [f(\mathbf{m}) - \mathbf{d}]^T \mathbf{C}_D^{-1} [f(\mathbf{m}) - \mathbf{d}], \tag{2.7}$$

the first term only in the expression (2.1). The linear solution can be written as

$$\delta\mathbf{m} = \left(\mathbf{A}^T \mathbf{C}_D^{-1} \mathbf{A}\right)^{-1} \mathbf{A}^T \mathbf{C}_D^{-1} \delta\mathbf{d}. \tag{2.8}$$

The observed data $\mathbf{d}$, which are first arrival times in this case, unavoidably contain errors from different sources such as noise disturbance, and traveltime picking errors etc.. Their actual values remain indeterminate, but if errors can be treated as random variables, their statistical properties such as the expected value, variances and covariance can be estimated. In the least-squares formula (2.7), errors are implicitly treated as random variables. This is usually the basis for estimating the data covariance matrix $\mathbf{C}_D$.

For teleseismic tomography, mispicks of onsets or incorrect phase association can be treated as random errors that may not yield any significant bias to the tomographic model parameters, because these errors are so small compared to the traveltime measurement (Röhm *et al.*, 2000). In crosshole seismic tomography, however, these data-picking errors may not be treated as random variables with a Gaussian distribution and the solution may therefore be biased. Figure 2.1a is a sample shot gather on which first arrivals of the far offset traces cannot be clearly identified and thus the picked times are not reliable at all. If those traveltimes were used in the inversion, the resultant image would have strong artefacts, as shown in Figure 2.1b.

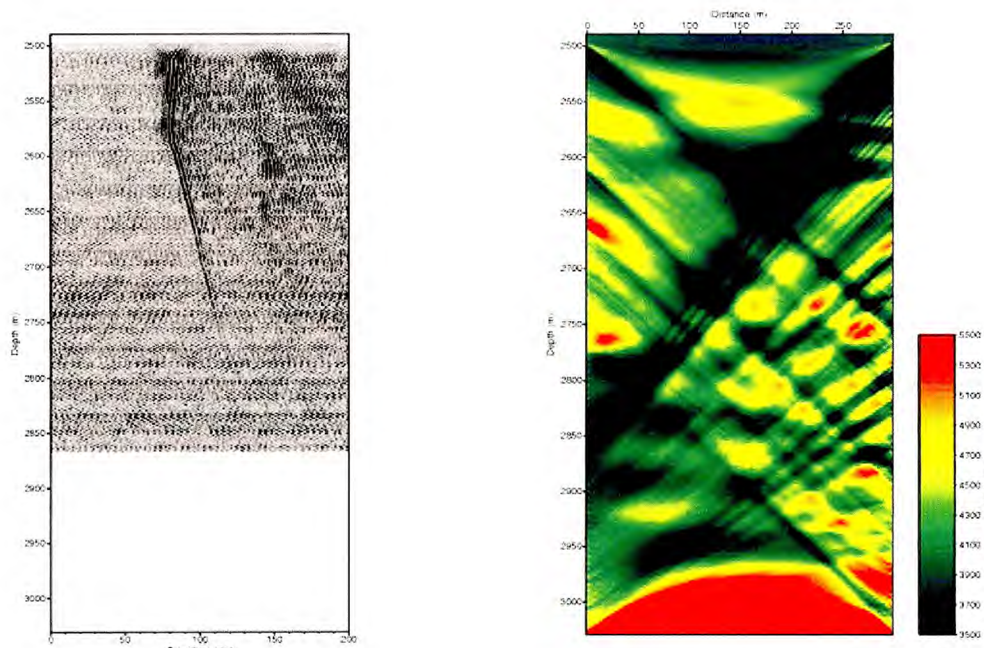

(*a*) (*b*)

Figure 2.1 (*a*) A sample shot gather of crosshole seismic, with 350 receivers, shows the uncertainty of the first arrival in the far offset traces. (*b*) Preliminary result of travel time inversion which shows strong artefacts due to travel time picking errors.

In this chapter, I attempt to suppress these erroneous traveltimes in the inverse problem by properly setting the matrix $\mathbf{C}_\mathrm{D}^{-1}$ in the least-squares formula (2.7). Matrix $\mathbf{C}_\mathrm{D}^{-1}$ here is no longer an explicit statistic measurement of the data errors. Instead, I define it pragmatically as a diagonal matrix with positive definite elements, representing our confidence in each individual traveltime pick, as

$$\mathbf{C}_\mathrm{D}^{-1} = \mathrm{diag}\{c_i\} \quad , \tag{2.9}$$

where c_i is the estimated certainty of the i-th measurement. For the i-th ray between a source at (x_s, z_s) and a receiver at (x_r, z_r), as shown in Figure 2.2a schematically, the data certainty is defined in terms of the vertical offset as

$$c_i = \begin{cases} 1, & \text{for } \ l \le l_a, \\ 0.51 + 0.49\cos\left(\dfrac{l - l_a}{l_b - l_a}\pi\right), & \text{for } \ l_a < l \le l_b, \\ 0.02, & \text{for } \ l \ge l_b, \end{cases} \tag{2.10}$$

where l is the normalized vertical offset $l = |z_r - z_s|/|x_r - x_s|$ for the source-receiver pair. The smaller the vertical offset is, the more certain the observation should be, since the overall attenuation will typically be smaller for a shorter ray path. Another argument given for such weights is that the ray paths with small vertical offset are more likely to correspond to real ray paths that remain completely in the image plane for two-dimensional reconstruction problems. In fact, this was the motivation for Berryman's (1989) weighting scheme in which rays of greatest length were weighted least in the reconstruction.

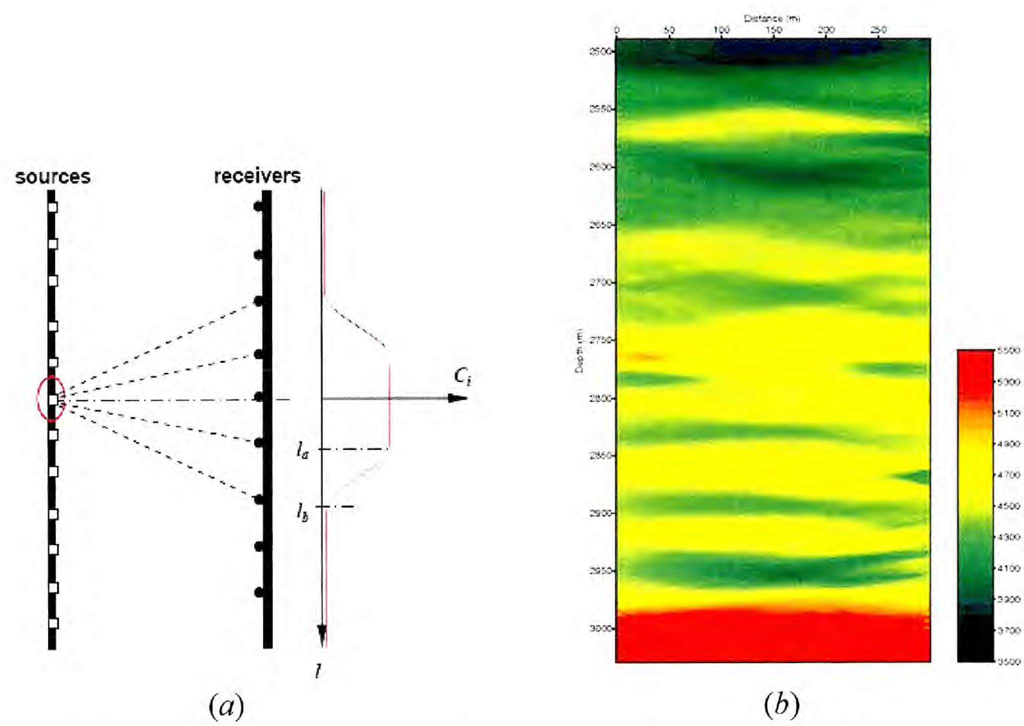

Figure 2.2 (*a*) The data certainty, c_i, of the i-th traveltime picking is defined in terms of the (normalized) vertical offset l, and is used to build the data confidence matrix, which is conventionally referred to as the inverse of data covariance matrix. (*b*) The inversion result suggests that the data-error effect has been suppressed successfully, by using the data confidence matrix.

The choice of parameters l_a and l_b in expression (2.10) can be somewhat arbitrary, but here I set them based on a limited number of experiments, in which l_a is more or less fixed but l_b is the parameter that is adjusted according to the inversion result. For the rest of this chapter, the images shown are obtained with l_a = 0.2 and l_b = 0.5. By using this working solution, I produce an encouraging result as shown in Figure 2.2b, in which the layered structure has been reconstructed and some velocity anomalies have been shown clearly.

2.5 Balancing the contribution of data minimization and the *à priori* model

In this section, I attempt to somehow quantitatively balance the contribution from the data minimization and from the *à priori* model, by testing the trade-off parameter, μ.

Given *à priori* model $\mathbf{m}_0$, the objective function is given as expression (2.1), and the linear solution is written as equation (2.6), in which parameter μ acts as a dimensionless damping factor, introduced to stabilize the inverse procedure. In this section where I am testing the parameter μ, I simply set $\mathbf{C}_{\mathrm{M}}^{-1} = \kappa\mathbf{I}$, where $\mathbf{I}$ is the identity matrix with units of (*model parameter*)$^{-2}$, κ is a dimensionless normalizing factor given by (Wang and Pratt 1997)

$$\kappa = \frac{\mathrm{trace}\left(\mathbf{A}^{\mathrm{T}}\mathbf{C}_{\mathrm{D}}^{-1}\mathbf{A}\right)}{n_r}, \tag{2.11}$$

and n_r is the total number of ray paths. The *à priori* model in this test as shown in Figure 2.3a is built from traveltime back-projection (Worthington 1984) with the data confident matrix $\mathbf{C}_{\mathrm{D}}^{-1}$ described above to suppress the effect of traveltime picking errors. By using the normalizing factor κ, any value I set for the trade-off parameter μ will has an objective value relative to data and model specification (Wang 2003).

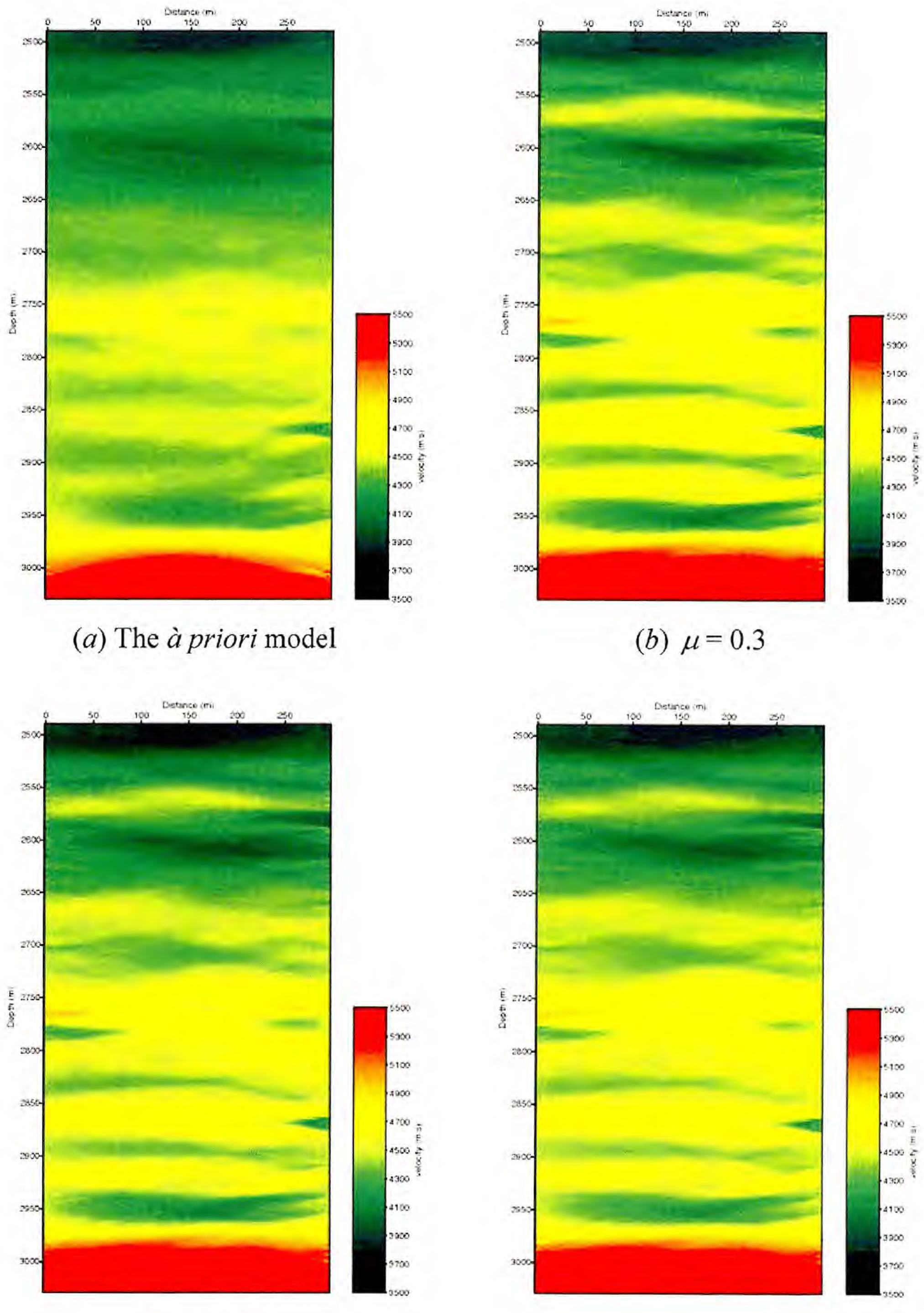

(*a*) The *à priori* model (*b*) $\mu = 0.3$

(*c*) $\mu = 0.5$ (*d*) $\mu = 0.7$

Figure 2.3 The *à priori* model and images obtained from traveltime tomography with different values for the μ parameter.

The motivation for using the model constraint term in the objective function (2.1) is that, although there may be many "solutions" to the inverse problem, the ones with least deviation from some prescribed background, $\mathbf{m}_0$, are most likely to have no spurious structure. The trade-off parameter μ thus controls the similarity of the final inversion result and the initial the *à priori* model. Using the normalization factor κ, parameter μ is then chosen within the interval $[0.0, \ 1.0]$.

Figures 2.3b, 2.3c and 2.3d show resultant images with μ = 0.3, 0.5 and 0.7, respectively. When μ increases, the resultant velocity model is more and more similar to the *à priori* model. The top and bottom parts are more similar to the elliptic character of the *à priori* model; the 2600-2750 m depth portion is more similar to the cloudy character of the reference model.

From the convergence rates, as shown in Figure 2.4, I can see that when μ = 0.1, the inversion has a steady convergence, even after 16 iterations. It potentially has a risk to mis-interpret spurious noise in the data as a geological feature. When μ = 0.3, 0.5 and 0.7, the inversions show clear dependence on the *à priori* model. For μ = 0.7 the convergence rate decreases after 4 iterations. For μ = 0.5 the convergence rate decreases after 6 iterations. For μ = 0.3 the convergence rate decreases after 8 iterations. Therefore, in the rest of these tests, I choose μ = 0.3 and the image of the 8^{th} iteration as the final result. After 8 iterations, the data misfit is small and spurious noise in the data has not caused significant erroneous structure in the model.

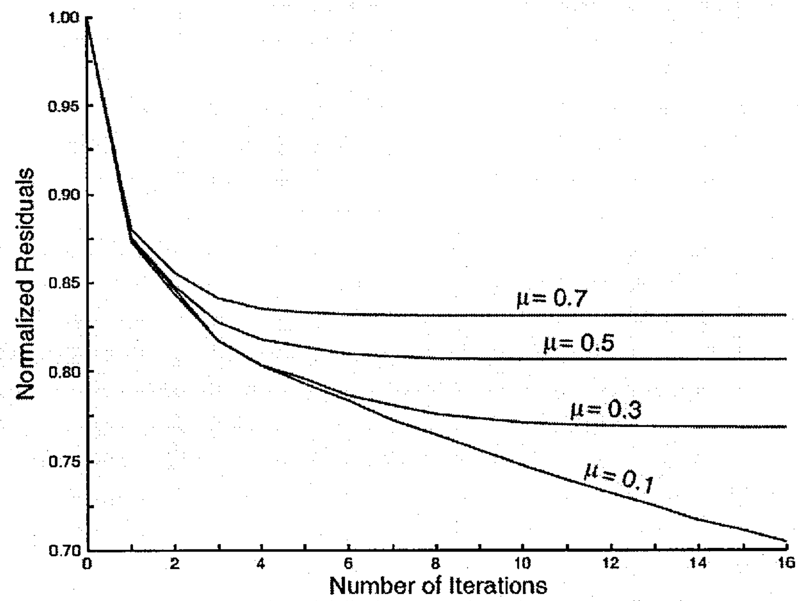

Figure 2.4 Convergence rates with different μ values.

2.6 Well-log constraint in the inversion

For use of sonic logging information as a geological constraint in the inverse problem, I discuss two schemes in this section.

In the first scheme, I construct an initial model by combining the sonic logging velocity obtained from both source and receiver wells and the velocity field obtained from the traveltime back-projection. The j-th velocity in the initial model, $v_j^{(\text{init})}$, is given by

$$v_j^{(\text{init})} = \omega_j v_j^{(\text{log})} + (1-\omega_j) v_j^{(\text{t})} , \tag{2.12}$$

where $v_j^{(\text{log})}$ is the logging velocity, $v_j^{(\text{t})}$ is the velocity obtained from travel time back projection, and ω_j is the weighting coefficient. In this chapter, I set the weight ω_j here as an estimated certainty of the j-th measurement. It is defined in terms of the position of the centre of j-th cell in the x direction, relative to the position of the logged hole:

$$\omega_j = \begin{cases} 0.5 - 0.5\cos\left(\dfrac{x_a - x_j}{x_a}\pi\right), & \text{for } x_j \le x_a, \\ 0, & \text{for } x_a < x_j < x_b, \\ 0.5 - 0.5\cos\left(\dfrac{x_j - x_b}{X - x_b}\pi\right), & \text{for } x_j \ge x_b. \end{cases} \tag{2.13}$$

where x_j is the centre point position of j-th cell in the x direction, X is the distance between two wells. In this experiment, X = 300 m. I set x_a= 50 m, and x_b= 250 m, which means I use the logging information as a constraint at a 50 m range in the vicinity of each of two boreholes. Figure 2.5 shows the diagrammatic curve of the relation between ω_j and x_j.

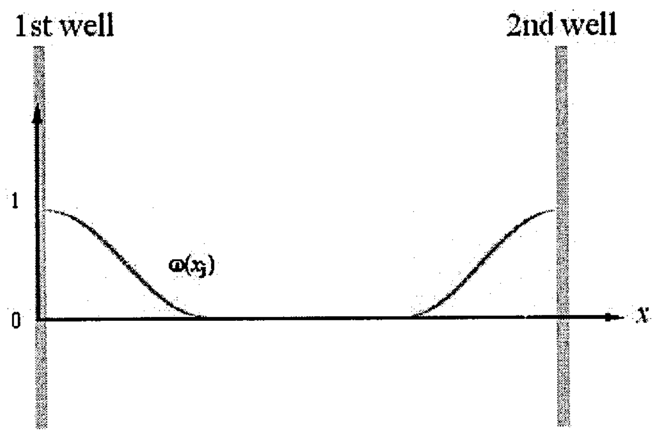

Figure 2.5 The diagrammatic curve of the relation between the weight coefficient ω_j and the horizontal distance x_j.

Figure 2.6a is the initial velocity built with well-log constraints. As the initial velocity model is the mixture of the logging information and the time back-projection model, in the inversion I set $\mathbf{C}_{\mathrm{M}}^{-1}$ as an identity matrix. Using the same data certainty

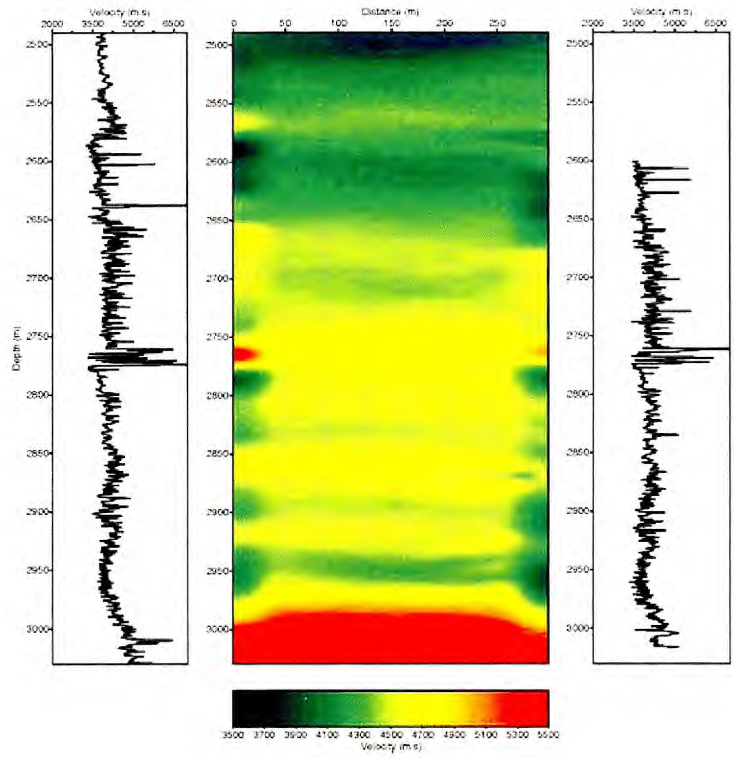

(*a*)

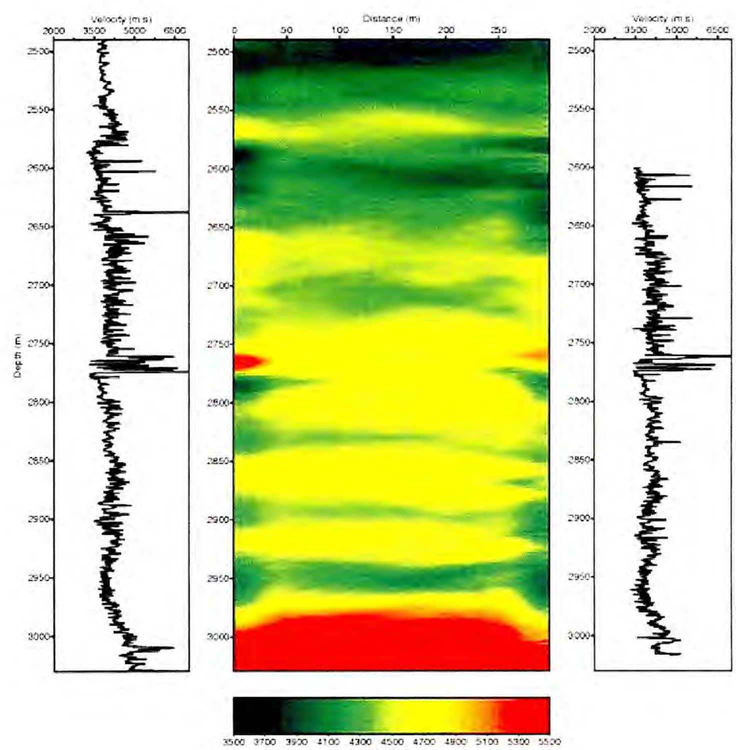

(*b*)

Figure 2.6 Well-log constraint scheme 1: (*a*) The initial velocity model is the weighted mixture of logging information from both boreholes and the velocity model derived from travel time back-projection. (*b*) The tomographic image with $\mu = 0.3$.

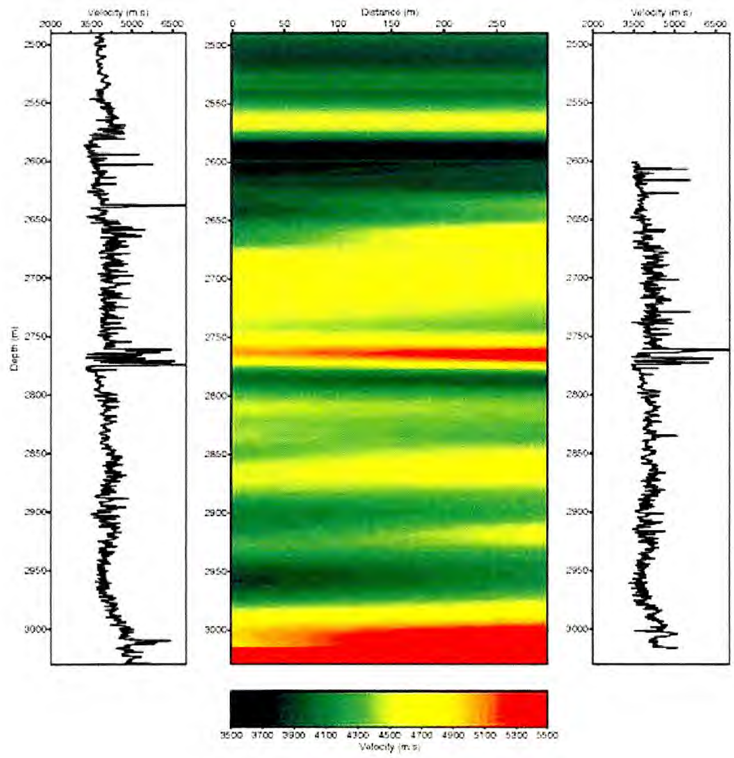

(*a*)

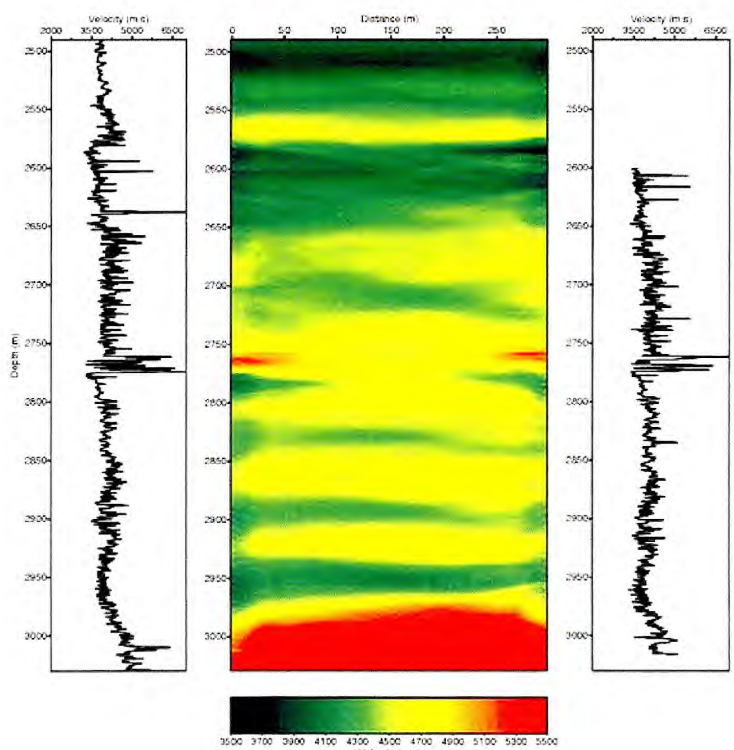

(*b*)

Figure 2.7 Well-log constraint scheme 2: (*a*) The initial model is simply a linear interpolation between the sonic logging curves for two boreholes. (*b*) The tomographic image with the initial model of figure (*a*) and a model covariance matrix defined as in Equation 2.14.

matrix $\mathbf{C}_\mathrm{D}^{-1}$ and the same parameter μ as in the previous experiment to solve equation (2.6), I obtain the well-log constrained velocity image as shown in Figure 2.6b.

The second scheme defines the initial model based purely on the logging information. As shown in Figure 2.7a, the velocity field between two wells is given by a simple linear interpolation between the two sonic logging curves. However, in the inversion, I defined the model covariance matrix as a diagonal weight matrix

$$\mathbf{C}_\mathrm{M}^{-1} = \kappa[\mathrm{diag}\{\omega_j\}] \ , \qquad (2.14)$$

where κ is estimated from equation (2.11). The arguments given for using such weighting coefficients are that the inversion solution should have least deviation from "hard" geological evidence, such as the sonic logging information. The remaining part of the survey region may be an constrained by the a prior model, since the true velocity might differ more from the initial velocity estimate, as it is far away from the actual measurement (well logging), and the true ray paths might deviate more from the initial ray path estimates.

Using the same data certainty matrix $\mathbf{C}_\mathrm{D}^{-1}$ and the same value for parameter μ=0.3 as in the previous experiment, I obtain the well-log constrained velocity image as shown in Figure 2.7b, in which the distinct layered structure with high/low velocities corresponds to the high and low velocity intervals in the well logs. Generally speaking, Figures 2.6b and figure 2.7b are quite similar in terms of spatial velocity variation.

2.7 Conclusions

To address issues in real data tomography of crosshole seismic, I have adopted a step-by-step strategy, which I believe is both practical and sensible:

(1) *Non-linearity problem.* I perform the crosshole traveltime inversion here as a linear inverse problem that solves the slowness update, rather than the slowness field directly as in the classic crosshole traveltime inversion.

(2) *The effect of data errors.* I manage to suppress the effect of the first arrival picking errors by providing a working definition to the conventional data covariance matrix, which is defined here explicitly as a data confidence matrix in terms of the vertical offset between source and receiver.

(3) *The balance between the data contribution and the à priori model.* I control it explicitly by the trade-off parameter μ in the inversion. To make the choice of μ meaningful, I use the normalizing factor κ systematically in advance.

(4) *Logging constraint.* After I have solved the above three issues, I start to bring in the logging information as geological constraint in the inversion.

By addressing these issues step by step, I am confident that the final tomographic image, which shows clear layered structure with high and low velocity layers corresponding to the sonic logging curves, is not biased by any strong constraints.

Chapter 3

Waveform tomography for real crosshole seismic data

3.1 Introduction

The traveltime tomography in the previous chapter, making use solely of the arrival times, is based on the asymptotic high frequency rays. However, the recorded data not only contain information on transmitted energy but also scattered energy, which is not utilized in traveltime inversions. Waveform tomography removes the assumption of asymptotic rays and makes use of all of the data.

Seismic waveform tomography, especially when using transmission data, is able to provide a quantitative image of physical properties in the subsurface, not only a structural image as in conventional seismic migration. It has the potential to image the velocity field with significantly improved resolution, useful for time-lapse, high-resolution imaging of the reservoir. In crosshole seismic tomography, traveltime inversion uses first arrival times to reconstruct a velocity distribution of the survey region (Lytle and Dines, 1980; McMechan, 1983; Beydoun and Mendes, 1989; Bregman *et al.*, 1989; Washbourne *et al.*, 2002; Bergman *et al.*, 2004; Rao and Wang 2005). However, recorded seismic data contain not only first arrival time information but also scattered energy waveforms, not utilized in traveltime inversion. Waveform inversion attempts to use these waveforms for velocity model reconstruction (Pratt and Worthington, 1990; Song *et al.*, 1995; Pratt *et al.*, 1998; Pratt, 1999; Charara *et al.*, 2000; Zhou and Greenhalgh, 2003; Ravaut *et al.*, 2004; Sirgue and Pratt, 2004; Pratt *et al.*, 2005). The process generally starts with an initial model and then updates it iteratively by minimizing the differences between the observed data wavefield and the theoretical data wavefield. This results in an efficient imaging tool, capable of being used on a production basis for practical problems.

For waveform inversion, the frequency-domain version enables the use of distinct frequency components and thereby reduces the quantity of data required for processing (Pratt and Worthington, 1990; Sirgue and Pratt, 2004). Although in principle all frequencies may be modelled to fit the observations (equivalent to 'time domain' waveform inversion), in practice adequate reconstructions may be obtained with a reduced set of frequencies ('frequency domain' waveform inversion). Marfurt (1984) pointed out that the frequency domain could be the method of choice for finite-difference/finite-element modelling if a significant number of source locations were involved. Pratt and Worthington (1990) pointed out that large aperture seismic surveys could be inverted effectively using only a limited number of frequency components. Recently Sirgue and Pratt (2004) further showed that frequency-domain inversion of reflection data using only a few frequencies could yield a result that is comparable to full time-domain inversion.

To demonstrate this point, I set up a synthetic example, as shown in Figure 3.1a. The synthetic model I designed contains some realistic geological features: channels, a fault, and a dipping layer. For crosshole traveltime tomography, it is almost impossible to recover a vertical structure with a sharp velocity change between the left and right (Bregman *et al.*, 1989). I set up this extreme feature as an attempt to test the limits of waveform inversion. Traveltime inversion, with proper handling of data errors, model constraints etc., is capable of producing a smooth approximation of the velocity structure, that is, the low-wavenumber background of the actual velocity variation, as shown in Figure 3.1b, but can't reconstruct vertical and dipping structures. What I am expecting from waveform inversion is that it should be able to reconstruct those geological features clearly and accurately. In the waveform inversion, I use the traveltime tomographic image as the initial model in an iterative procedure.

Taking advantage of the frequency-domain waveform inversion, I selected only eight frequencies between 200 and 900 Hz with increment of 100 Hz in the inversion. After tomographic inversion of only the 200 Hz data component, I see that the blurred fault and dipping layer starts to appear, as shown in Figure 2.1c. After tomographic inversion using all of the eight selected frequencies recursively, I see that the reconstructed velocity image shows clear interfaces between different velocity blocks, as shown in Figure 3.1d. It has essentially the same structural characteristics and velocity values as the true model I designed.

When dealing with real seismic data, there are three problems at least that affect waveform tomography: (1) limited bandwidth, especially missing low frequency data components; (2) poor signal-to-noise ratio; (3) limited unevenly distributed ray coverage. For successful application of waveform tomography on real crosshole seismic data, based on our experience, against the three problems above, there are three critical requirements as follows. All of these three requirements are equally important.

First, a good starting model is critical for waveform tomography. The lowest frequency available in real crosshole seismic data is for instance around 190 Hz in the case of the Shengli dataset. For waveform inversion, frequencies between 0 and 190 Hz are absent, and I have to rely on an accurate traveltime tomography to generate an initial model for waveform tomography. The method of traveltime tomography used in dealing with real crosshole seismic data is described in chapter 2, in which I have discussed some working solutions to several practical issues relevant to crosshole traveltime inversion.

Second, for real data application, a group of frequencies should be used for each individual iteration of the inversion procedure. Although I have used a single frequency component of the data for each iteration and produced an adequately good image in the synthetic example of Figure 3.1, to combat the noise in real seismic data, I do need to use a group of frequencies simultaneously in the inversion (Pratt and Shipp 1999). Simultaneously using neighbouring frequencies from the same spatial imaging position may have an averaging effect that suppresses data noise to the input of the inversion. For a fixed number of model parameters, using more data in the inversion means that the inverse problem is much better determined.

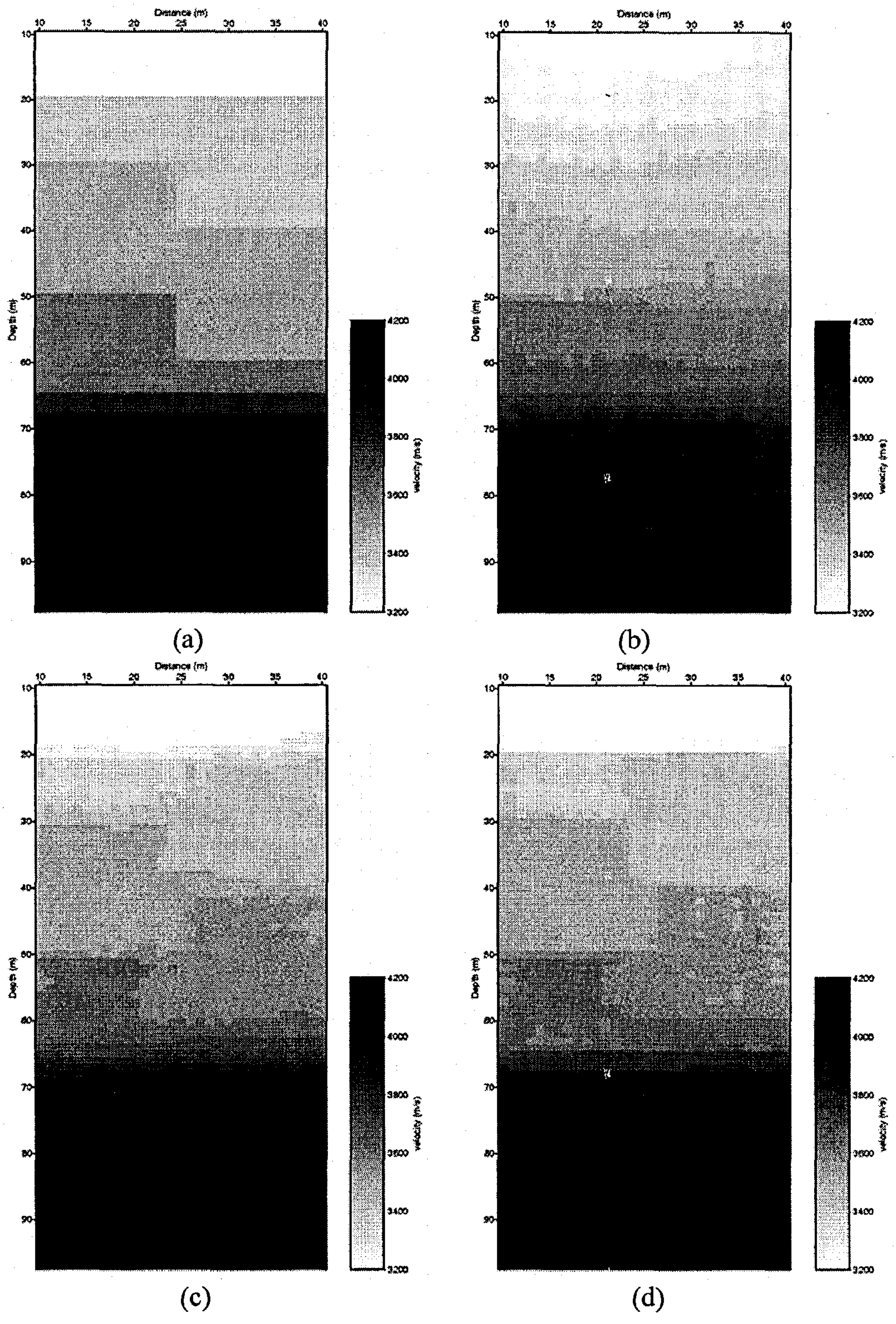

Figure 3.1 (a) A synthetic model consisting of vertical and dipping features for testing the waveform tomography approach. (b) Traveltime tomography result which is used as the initial model for waveform tomography. (c) Reconstruction of the velocity image after using only the 200 Hz component in the tomographic inversion. (d) The final reconstructed model after using eight selected frequencies between 200 Hz and 900 Hz with 100 Hz interval.

Third, a model smoothness constraint must be used in waveform tomography in order to produce a reasonable image from real crosshole seismic data. As ray coverage is not evenly distributed, the data residual may attribute more to some cells of the model and less to others. Using a smoothness constraint, I force the inversion to update the model evenly in space. However, use of a smoothness constraint may slow down the convergence of the inversion. I will discuss this issue in chapter 4, where I set up a series of resolution analysis tests using checkerboard waveform tomography.

In addition, there have been several publications showing other critical problems with real data waveform tomography, particularly that of anisotropy (Pratt and Shipp, 1999) as well as that of attenuation (Pratt *et al.,* 2005), which are not covered in this chapter.

3.2 The inverse problem

In this section, I summarize the inverse theory for frequency-domain waveform tomography, for the sake of completeness. For a detailed theoretical background, readers may refer to Tarantola (1984). But for the frequency domain treatments, see Pratt and Worthington (1990) and Pratt *et al.* (1998).

In the inverse problem, the objective function is defined as

$$J(\mathbf{m}) = \frac{1}{2}\left\{[\mathbf{P}(\mathbf{m}) - \mathbf{P}_{\text{obs}}]^{\text{H}} \mathbf{C}_{\text{D}}^{-1} [\mathbf{P}(\mathbf{m}) - \mathbf{P}_{\text{obs}}] + \mu[\mathbf{m} - \mathbf{m}_0]^{\text{H}} \mathbf{C}_{\text{M}}^{-1} [\mathbf{m} - \mathbf{m}_0]\right\}, \qquad (3.1)$$

where $\mathbf{P}_{\text{obs}}$ is an observed data set, $\mathbf{m}$ is the model to invert for, $\mathbf{P}(\mathbf{m})$ is a modelled data set, $\mathbf{C}_{\text{D}}$ is the covariance operator in the data space with units of $(data)^2$, defining the uncertainties in the data set, $\mathbf{m}_0$ is a reference model. In this chapter, I choose start model as the reference model $\mathbf{m}_0$. $\mathbf{C}_{\text{M}}$ is called the model covariance matrix with units of $(model\ parameter)^2$, and μ is a scalar that controls the relative weights of the data contribution and the model constraint in the objective function. In equation (3.1), the superscript $^{\text{H}}$ denotes the complex conjugate transpose.

For minimizing the objective function (3.1), I use a gradient method (Tarantola 1984, 2005), starting with the differentiation of the objective function with respect to the model parameters:

$$\frac{\partial J}{\partial \mathbf{m}} = \mathbf{L}^{\mathrm{H}}\mathbf{C}_{\mathrm{D}}^{-1}\delta\mathbf{P} + \mu\mathbf{C}_{\mathrm{M}}^{-1}\delta\mathbf{m}, \tag{3.2}$$

where $\delta\mathbf{m} = \mathbf{m} - \mathbf{m}_0$ is the model perturbation, $\delta\mathbf{P} = \mathbf{P}(\mathbf{m}) - \mathbf{P}_{\mathrm{obs}}$ is the data residual, and $\mathbf{L}$ is a matrix of the Fréchet derivative of $\mathbf{P}(\mathbf{m})$ at the point $\mathbf{m}$. The first term in equation (3.2) is the gradient direction of the data misfit:

$$\hat{\gamma} = \mathbf{L}^{\mathrm{H}}\mathbf{C}_{\mathrm{D}}^{-1}\delta\mathbf{P} = \mathbf{L}^{\mathrm{H}}\delta\hat{\mathbf{P}}, \tag{3.3}$$

where $\delta\hat{\mathbf{P}} = \mathbf{C}_{\mathrm{D}}^{-1}\delta\mathbf{P}$ is a weighted data residual. Setting $\partial J/\partial\mathbf{m} = 0$ in equation (3.2), I obtain the following equation

$$\delta\mathbf{m} = -\alpha\mathbf{C}_{\mathrm{M}}\hat{\gamma}, \tag{3.4}$$

where α is an update step length that needs to be determined.

In order to evaluate the gradient $\hat{\gamma}$ using equation (3.3), I need to know the Fréchet matrix $\mathbf{L}$, which is obtained from the following linear formula,

$$\delta\mathbf{P} = \mathbf{L}\delta\mathbf{m}. \tag{3.5}$$

This is the first term in a Taylor's series for $\delta\mathbf{P}$ and relates the data perturbation $\delta\mathbf{P}$ to the model perturbation $\delta\mathbf{m}$. However, the direct computation of $[\mathbf{L}]_{ij} = \partial P_i / \partial m_j$ is a formidable task when P_i are seismic waveforms. Instead, Tarantola (1984) showed that the action of matrix $\mathbf{L}^{\mathrm{H}}$ on the weighted data residual vector $\delta\hat{\mathbf{P}}$ (equation 3.3) can be computed by a series of forward modelling steps, summarized as follows.

The frequency domain acoustic wave equation for a constant density medium with velocity $c_0(\mathbf{r})$ is

$$\left(\nabla^2 + \frac{\omega^2}{c_0^2(\mathbf{r})}\right)P_0(\mathbf{r}) = -S(\omega)\delta(\mathbf{r} - \mathbf{r}_0), \tag{3.6}$$

where $\mathbf{r}$ is the position vector, $\mathbf{r}_0$ locates the source position, $S(\omega)$ is the source signature of frequency ω, and $P_0(\mathbf{r})$ is the (pressure) wavefield of this frequency. If the velocity is perturbed by a small amount $\delta c(\mathbf{r}) << c_0(\mathbf{r})$, that is, $c_0(\mathbf{r}) \to c(\mathbf{r}) = c_0(\mathbf{r}) + \delta c(\mathbf{r})$, then the total wavefield is correspondingly perturbed to $P_0(\mathbf{r}) \to P(\mathbf{r}) = P_0(\mathbf{r}) + \delta P(\mathbf{r})$. Following wave equation (3.6), δP approximately satisfies

$$\left(\nabla^2 + \frac{\omega^2}{c_0^2(\mathbf{r})}\right)\delta P(\mathbf{r}) = 2\omega^2 P_0(\mathbf{r}) \frac{\delta c(\mathbf{r})}{c_0^3(\mathbf{r})}. \tag{3.7}$$

Considering $2\omega^2 P_0(\mathbf{r})\delta c(\mathbf{r}) / c_0^3(\mathbf{r})$ as a series of 'virtual sources' over $\mathbf{r}$, the integral solution for $\delta P(\mathbf{r})$ can be expressed as

$$\delta P(\mathbf{r}) = -\int_M \delta c(\mathbf{r}') \frac{2\omega^2}{c_0^3(\mathbf{r}')} P_0(\mathbf{r}') G(\mathbf{r}, \mathbf{r}') d\mathbf{r}', \tag{3.8}$$

where $G(\mathbf{r},\mathbf{r}')$ is the Green's function for the response at $\mathbf{r}$ to a point source at $\mathbf{r}'$ for the original velocity field. Note that in the acoustic case where I assume density to be constant, and define the model by the velocity field only, $\mathbf{m} \equiv \mathbf{c}$. Then comparing equation (3.8) against the matrix-vector form of equation (3.5), I see that the Fréchet matrix is defined with element $L(\mathbf{r},\mathbf{r}') = -\left[2\omega^2 / c_0^3(\mathbf{r}')\right] P_0(\mathbf{r}') G(\mathbf{r},\mathbf{r}')$. Substituting this Fréchet kernel into equation (3.3), I obtain

$$\hat{\gamma}(\mathbf{r}) = \left(\frac{2\omega^2}{c_0^3(\mathbf{r})}\right)^* \int_D P_0^*(\mathbf{r}') G^*(\mathbf{r}, \mathbf{r}') \delta \hat{P}(\mathbf{r}'). \tag{3.9}$$

where the superscript * denotes conjugate.

Replacing the integral over the data space with a summation over source and receiver pairs, denoted by s and g respectively, as the source and receiver positions are inherently discrete and finite in number, I can obtain

$$\begin{aligned}\hat{\gamma}(\mathbf{r}) &= \left(\frac{2\omega^2}{c_0^3(\mathbf{r})}\right)^* \sum_{s,g}\left(P_0^*(\mathbf{r};\mathbf{r}')G^*(\mathbf{r},\mathbf{r}')\delta\hat{P}(\mathbf{r}')\right) \\ &= \left(\frac{2\omega^2}{c_0^3(\mathbf{r})}\right)^* \sum_{s}\left(P_0^*(\mathbf{r};\mathbf{r}_s)\sum_{g}G^*(\mathbf{r},\mathbf{r}_g)\delta\hat{P}(\mathbf{r}_g;\mathbf{r}_s)\right) \\ &= \left(\frac{2\omega^2}{c_0^3(\mathbf{r})}\right)^* \sum_{s}\left(P_0^*(\mathbf{r};\mathbf{r}_s)P_b^*(\mathbf{r};\mathbf{r}_s)\right),\end{aligned} \tag{3.10}$$

where

$$P_b(\mathbf{r};\mathbf{r}_s) = \sum_{g} G(\mathbf{r},\mathbf{r}_g)\delta\hat{P}^*(\mathbf{r}_g;\mathbf{r}_s) \tag{3.11}$$

representing the wavefield generated by a series of virtual sources $\delta\hat{P}^*(\mathbf{r}_g;\mathbf{r}_s)$, corresponding to a single source $\mathbf{r}_s$. Note that wavefield $P_b(\mathbf{r};\mathbf{r}_s)$ is not calculated directly from equation (3.11), but is computed using the same forward modelling scheme as used for the wave equation (3.6) with the virtual sources $\delta\hat{P}^*(\mathbf{r}_g;\mathbf{r}_s)$, a procedure often referred to as data residual back-propagation. In this chapter, I solve the frequency-domain wave equation using a finite-difference scheme (Alford, Kelly and Boore, 1974; Kelly, Treitel and Alford, 1976; Virieux, 1986; Pratt, 1990; Song, Williamson and Pratt, 1995; Štekl and Pratt, 1998; Pratt, 1999; Min *et al.,* 2000).

In summary, frequency domain waveform tomography is performed iteratively and, for each iteration, the inversion procedure may be divided into three steps:

Step 1 - calculating the synthetic wavefield $\mathbf{P(m)}$ for given initial model.

Step 2 - back-propagating the weighted data residual $\delta\hat{\mathbf{P}} = \mathbf{C}_\mathrm{D}^{-1}\delta\mathbf{P}$, to get the gradient direction $\hat{\gamma}$.

Step 3 - estimating the model update $\delta\mathbf{m} = -\alpha\mathbf{C}_\mathrm{M}\hat{\gamma}$, where the optimal step length α can be found by using the linear approximation or simply line search for a minimum of the objective function (Tarantola 2005).

3.3 The real data example

Here I use the same data as in Chapter 2. Figure 3.2a displays an example common-receiver gather at 2600 m depth, with the shot depth ranging from 2497 m to 2950 m. The data contain clear and coherent first arrivals, and the tube waves generated in the shot borehole. The tube waves appear to have a linear moveout in the common-receiver gather, with velocity of about 1460 m/s. The common-receiver gather after tube wave attenuation using an f - k filter is shown in Figure 3.2b, which also shows the repeatability of the source (Pratt *et al.*, 2005).

The common-receiver gathers then are re-sorted into common-shot gathers. Figure 3.2c displays a common-shot gather at 2600 m depth, which contains much stronger tube waves. The strong tube waves are generated by the interaction of the direct body waves with discontinuities in the receiver borehole. Figure 3.2d is the result after tube wave attenuation using an *f-k* filter. In the shot gather, the receiver spacing is 1.52 m and the Nyquest wavenumber is $k_{Nyq} = 0.329$ (1/m). For the tube waves with $dz/dt = 1470$ (m/s), any frequency component $f > k_{Nyq}(dz/dt) \approx$ 485 Hz is severely aliased. Thus, I simply filter out the frequencies higher than 485 Hz. Data noise has been reduced by a form of forward-backward linear prediction filtering in the frequency-space domain (Wang, 1999).

Figure 3.3a displays the frequency spectra of all traces within the example common-shot gather at 2600 m depth. Based on the frequency spectrum, which shows there is no energy for frequencies lower than 190 Hz, I choose the frequency band between 190 Hz and 485 Hz for the inversion. Note here that I use a real-valued frequency in waveform inversion. When considering wave attenuation effects, one may use a complex-valued frequency, see for example Pratt *et al.* (2005). Figure 3.3b is the source wavelet that I used in waveform inversion. It is estimated directly from first arrival.

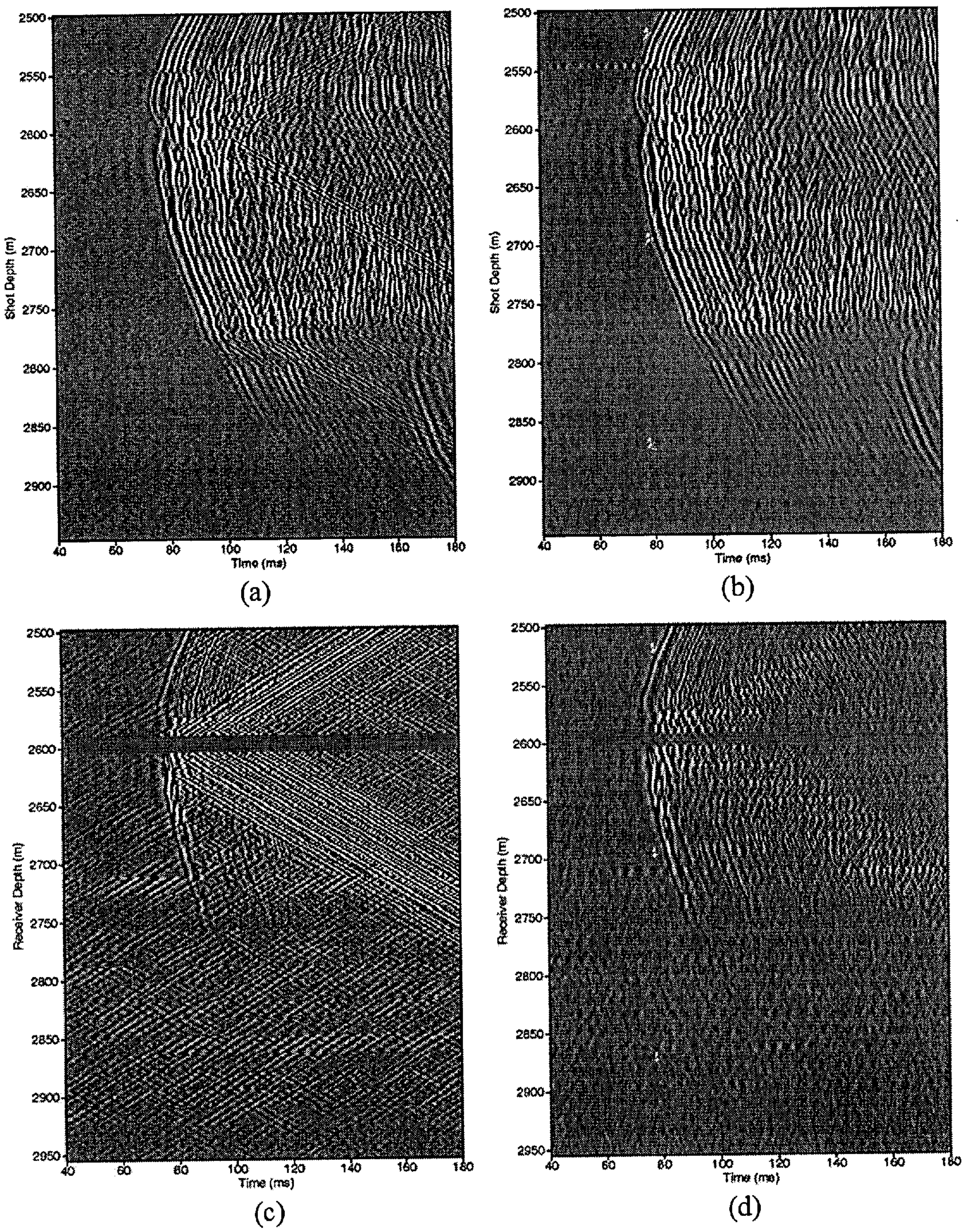

Figure 3.2 (a) An example common-receiver gather at depth 2600 m that shows weak tube waves. (b) The common-receiver gather after *f-k* filtering for tube wave attenuation. (c) An example common-shot gather at depth 2600 m which evidently shows strong tube waves. (d) The shot gather after *f-k* filtering for tube wave attenuation.

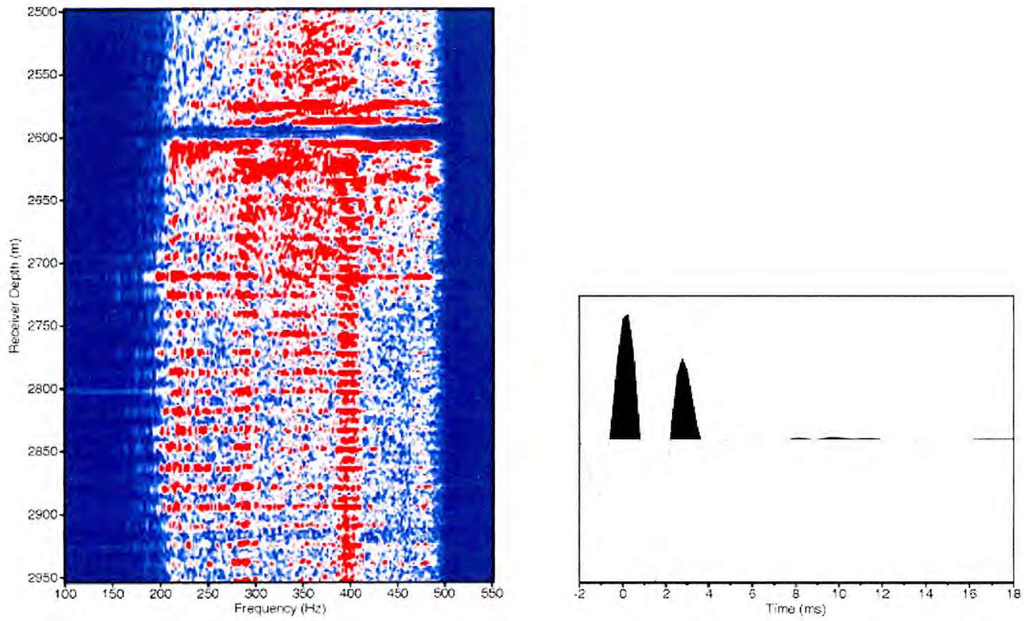

(a) (b)

Figure 3.3 (a) The amplitude spectrum of a typical shot gather at 2600 m (Figure 3.2d). It has frequency bandwidth between 190 Hz and 485 Hz. (b) Source wavelet estimated from real data. It is used in waveform inversion.

After tube wave suppression, I apply windowing to the data to mute any energy arriving later than a few cycles following the direct arrivals (Pratt and Shipp 1999; Pratt *et al.* 2005). After muting, only the first arrival and transmission waveforms remain in the crosshole seismic data. Windowing also serves to exclude remaining shear wave energy from the data. This pre-processing step is primarily required to precondition the data in order to force the inversion to fit the direct arrivals, which contain the critical information on the low and intermediate wavenumbers in the model. At a later stage, if needed the window size can always be increased in time to include more of the data.

Figure 3.4a shows an example shot gather (at depth 2758 m) after data windowing. The window length is selected to be as short as possible to enhance the signal-to-noise ratio and to eliminate shear waves, but still to include the visible diffractions and transmission associated with the direct arrival. For comparison, Figure 3.4b shows modelled shot gather calculated from the final tomography model. Although a frequency-domain waveform inversion approach uses only a number of selected frequencies, the data comparison reveals that the inversion model indeed is a good representation of the subsurface earth model.

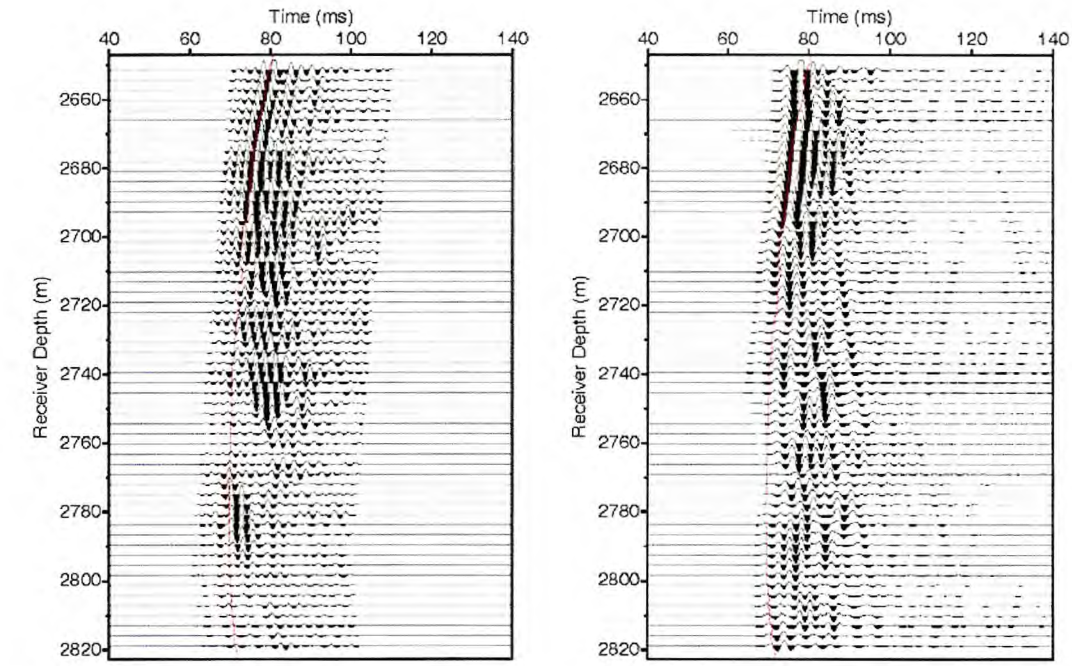

(a) (b)

Figure 3.4 (a) An example shot gather of the real data set after data windowing. (b) Modelled shot gather generated from the waveform inversion model. The red curve is the first arrival time line picked from real data.

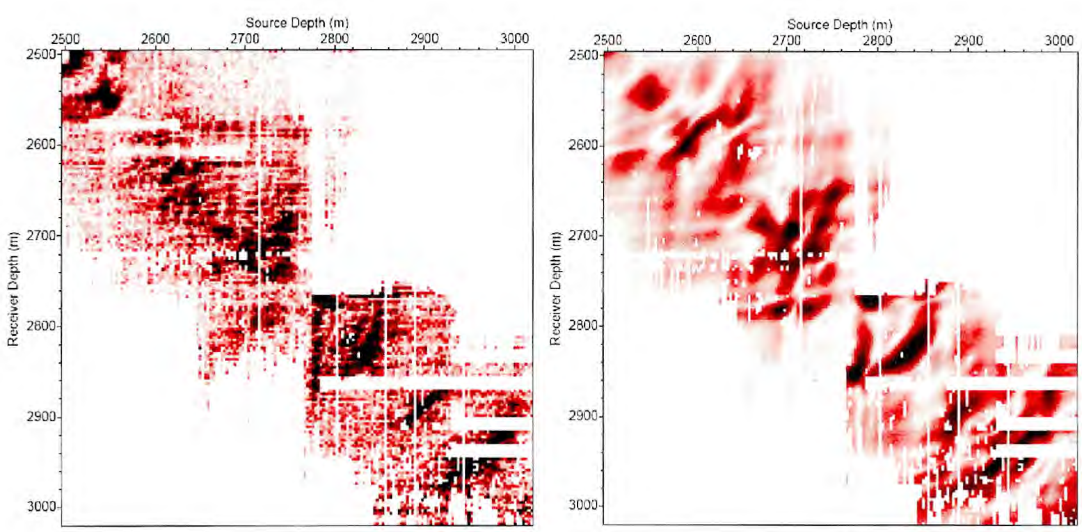

(a) (b)

Figure 3.5 (a) A frequency slice of the amplitudes of the observed crosshole seismic data. (b) The frequency slice of modelled data, at the same frequency (260Hz), generated from the final velocity model obtained by waveform tomography.

Figure 3.5a is an example frequency slice (at 260 Hz) of the amplitudes of the real data set and, for comparison, Figure 3.5b shows the corresponding frequency slice of the amplitudes of the modelled data set from waveform tomography. In the inversion, the amplitude of real frequency components $\mathbf{P}_{obs}$ is normalized base on the maximum amplitude of the estimated frequency components $\mathbf{P}(\mathbf{m})$. I start from lower frequencies. For low frequencies the inversion method is more tolerant of velocity errors, as these are less likely to lead to errors of more than a half-cycle in the waveforms. As the inversion proceeds, I move progressively to higher frequencies.

3.4 Waveform inversion of real data

For the inversion of this real data set, I make the velocity model discrete in cells with cell size 3 m to satisfy the criterion of four cells per wavelength for the highest frequency (485 Hz) that I use in the inversion. The depth range that I choose to invert for is from 2497 to 3022 m. Therefore, there are altogether 100 rows and 175 columns in the grid.

At the beginning of the waveform inversion scheme, an adequate starting model is necessary. This model should be capable of describing the time domain data to within a half of the dominant period, in order to avoid fitting the wrong cycle of the waveforms (Pratt *et al.* 2005). The lower the frequency, the less accurate the starting model needs be. However, all real data are band limited, and thus certain accuracy is required for the starting model. As shown in Figure 3.3, this real data set has a frequency gap between 0 and 190 Hz. The lack of low-frequency information makes the waveform inversion strongly dependent on the initial model. For waveform tomography I use the traveltime inversion result as an initial model and proceed with waveform inversion using the different frequencies.

Figure 3.6a displays the initial model, the result of traveltime tomography reported in Figure 2.2a. Figure 3.6b is the ray density, the (normalized) total length of ray segments across each single cell, a direct indicator of the confidence in the traveltime inversion solution, where a curved ray path is re-traced iteratively along with velocity updating. This measurement of certainty, being proportional to the ray density, can also be used in waveform tomography to build a diagonal matrix to be used as the model covariance matrix $\mathbf{C}_{\mathrm{M}}^{-1}$. The latter is applied to the gradient vector $\hat{\gamma}$ before model updating (see step 3 above).

In waveform tomography when dealing with real data, a model smoothness constraint is a necessity. A number of real data experiments I conducted indicate that, if I did not use a smoothness constraint in the inversion, waveform tomography would not converge at all, although I do not need such a constraint in synthetic data examples (Figure 3.1). Therefore, the primary cause is presumably the effect of data noise, which is not necessarily white in the frequency domain. Outliers might have a strong and biased influence on the model update. As the frequency domain data samples are complex valued, it is not easy to mitigate the data noise using the method of winnowing traveltimes and amplitudes described by Wang, White and Pratt (2000). Waveform inversion is a highly non-linear problem but if, in a linearized procedure, strong outliers are transferred linearly to strong model updates, the inversion procedure will be unstable and divergent.

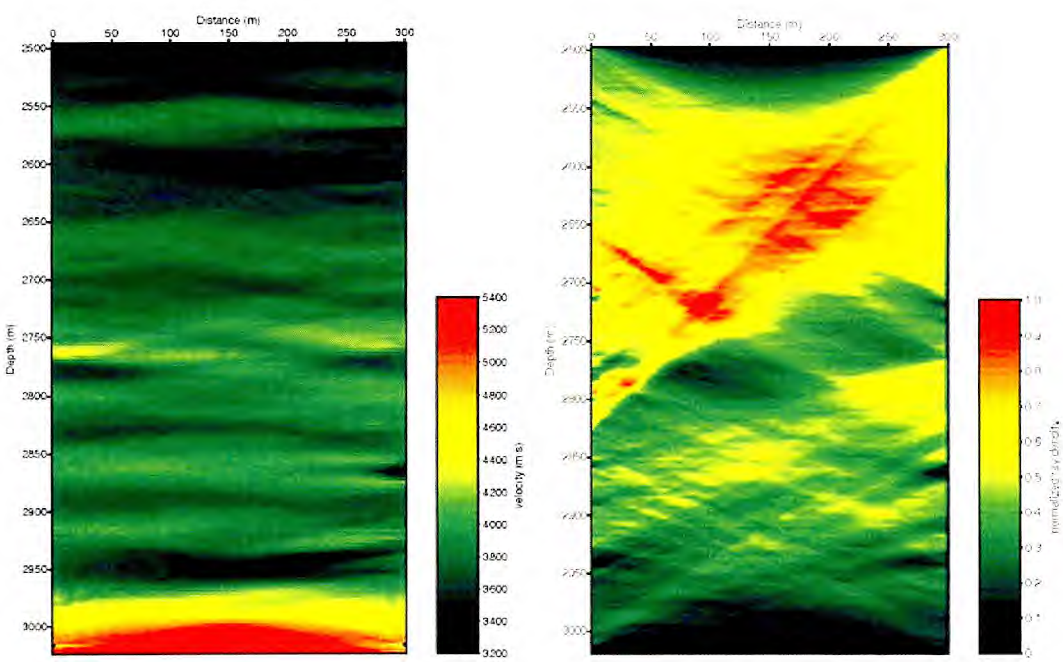

(*a*) (*b*)

Figure 3.6 (a) The initial velocity model for waveform inversion, generated by traveltime inversion. (b) Ray density of the real seismic data set.

A second effect is the unevenly distributed ray density. As shown in Figure 3.5b, the ray density distribution appears to be in short wavelength variation. An uneven distribution of ray density will cause a biased distribution of model update, as a model update is (inversely) proportional to the ray density through data residual back-propagation. When constructing the model covariance matrix $\mathbf{C}_M$, I could smooth the ray density distribution so as to change the weight of model update. This approach might reduce the roughness of model update for any single iteration and slow down the convergence of the iterative procedure, but may not mitigate the problem in the final solution. Ray density distribution is a measurement of the illumination in the physical experiment, and thus reflects directly the resolving power distribution.

The third effect is due to the model sensitivity. Investigation by Wang and Pratt (1997) revealed that in traveltime inversion long wavelength components of the velocity field are more sensitive than the short wavelengths, and that in amplitude inversion short wavelength components of the velocity field are much more sensitive than the long wavelength components. Therefore, in waveform inversion where amplitude information dominates, the data residual tends to attribute to shortest wavelength components of the model update first. This is contradictory to the philosophy of iterative linear inversion. In an iterative inversion, I must get the background right first, so that linearization can be used for the inverse problem. Some research groups have advocated amplitude-normalized waveform tomography, at least in the initial stages (Zhou and Greenhalgh 2003; Pratt *et al.* 2005).

This analysis suggests that I should use a smoothing operator of different size at each iteration, starting with a large smooth size and then reducing the size gradually as iterations proceed. This approach is sometimes referred to as a "multi-scale" approach. Pratt *et al.* (1998) has given a complete treatment of a "reduced parameterization" approach which incorporates all possible such multi-scale approaches. It is also worthwhile to mention that Wang and Houseman (1994, 1995) used a Fourier series to parameterize the velocity model (and interface geometry) with different wavenumbers and then partitioned them into different subspaces so that they could be inverted simultaneously. In the following waveform inversion, I use a fixed 3×3 smoothing operator. That is, any model update δm_i is an average value of neighbouring 9 points, centred at the ith cell, with equal weights.

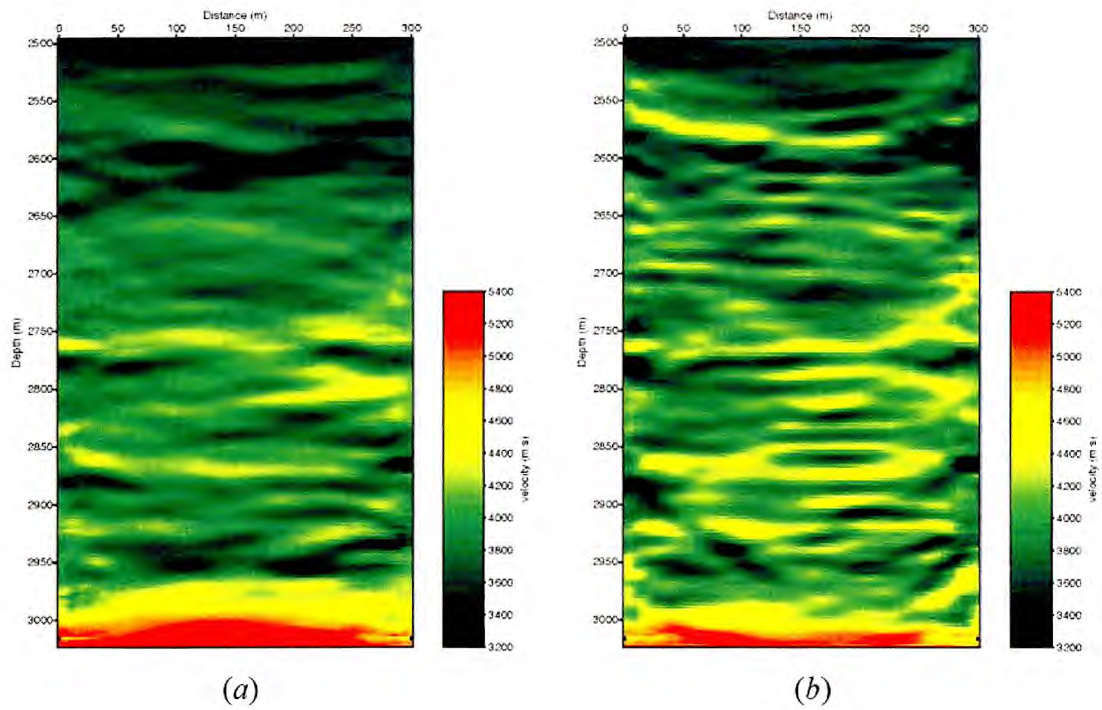

Figure 3.7 Waveform tomography experiment 1 – the inversion is executed by each frequency consecutively. (a) The image after using five frequency components between 190 and 210 Hz (with 5 Hz interval). (b) The result after using all 60 selected frequencies between 190 and 480 Hz. The image has strong X shaped artefacts.

With a fixed 3×3 smoothing operator used in waveform tomography, I now design two experiments to further combat the noise in real data. In the first experiment, I use all selected frequencies consecutively (190, 195, 200, 205, …, 485 Hz), as I did for the synthetic data test. I start with the initial model generated from traveltime inversion, and invert the 190 Hz data component first. Then, I switch to a higher frequency component (195 Hz) of the data as the inversion progresses. The result from each lower frequency is used as the starting model for the next higher frequency inversion. At each frequency stage, three iterations are carried out. Figure 3.7a shows the reconstructed image after using five frequency components between 190 and 210 Hz, and Figure 3.7b is the result after using all 60 selected frequencies between 190 and 480 Hz.

In the second experiment, I use a group of five neighbouring frequencies simultaneously in the inversion (Pratt and Shipp 1999). The 60 selected frequencies are assigned into 12 groups with increasing frequency contents. The result from each lower frequency group is used as the starting model for the inversion of the next higher frequency group. For each group, three iterations are carried out, proceeding through all groups. For each iteration, the gradient of each frequency group is computed using all five frequencies simultaneously. Figure 3.8a shows the tomographic image after using the first frequency group (190, 195, 200, 205, 210 Hz), and Figure 3.8b is the final result after using all 12 frequency groups consecutively.

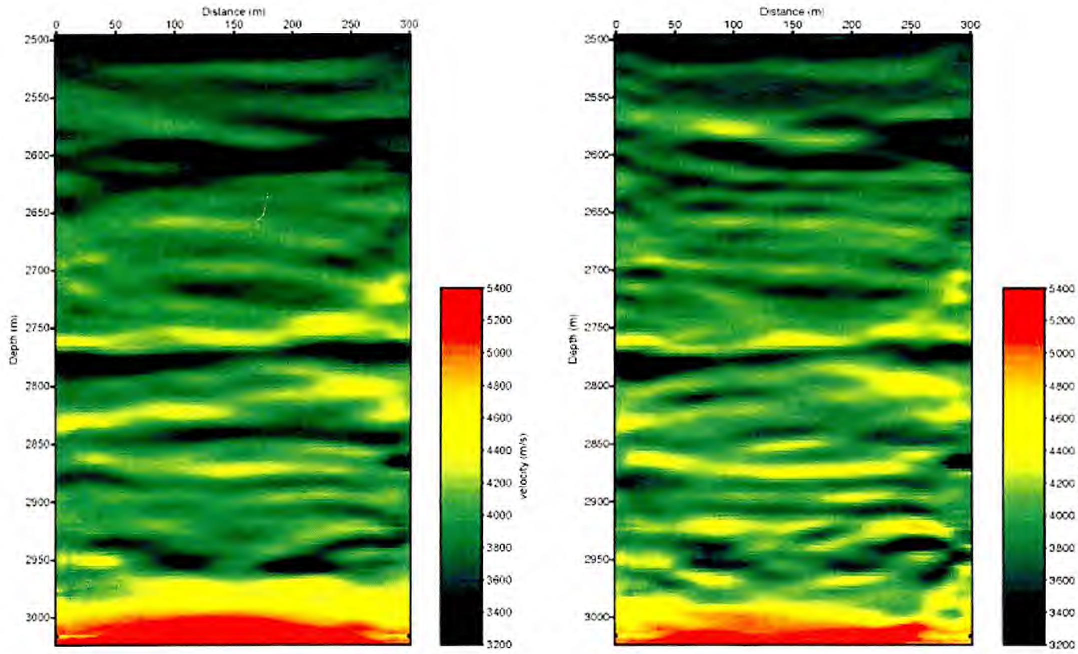

(a) (b)

Figure 3.8 Waveform tomography experiment 2 - inversion executed using sequential groups of five frequencies. (a) The velocity image after using the first frequency group (190, 195, ..., 210 Hz). (b) The inversion result after using all 12 frequency groups; it is regarded as the final result of waveform tomography.

Comparing the inversion results of those two experiments, I see that Figure 3.7b is marked by the presence of some X-shaped artefacts that cross the image. Such artefacts are quite often obtained in crosshole tomography, especially when waveform inversion is attempted. They are due to the nonuniform coverage of the object spectrum and the lack of information about the object spectrum in certain directions (Wu and Toksöz, 1987). When using multiple frequencies simultaneously, the inherent filtering (smoothing) might have the effect of extrapolating the object spectrum to the blind area. The final result of the second experiment has many fewer artefacts, and the image is smoother and more continuous than that of experiment one, especially at the 2800-2950m portions. I recommend using the strategy of the second experiment in practice, in order to mitigate the data noise effectively in the input of waveform tomography.

Comparing the final result of waveform inversion (Figure 3.8b) with the traveltime inversion result (Figure 3.6a), I can see that the results of waveform inversion appear to be a significantly better representation of the geological layering than the original traveltime inversion result which is used as a starting model. The most striking features of the final waveform inversion results are high-velocity layers. At the section from 2500 to 2900m, the layers appear laterally continuous across the section, and the vertical resolution is clearly much better. Deeper layers are discontinuous and faulted. In addition, a number of low-velocity layers are evident on the image.

3.5 Well-log constrained waveform inversion

In this section, I use well-log information as a geological constraint on the waveform inversion to test the dependence of the inversion result on the initial model.

I design an initial model by combining sonic logging velocities and the velocity field obtained from the traveltime tomography. The velocity in the jth column of the initial model, $v_j^{(\mathrm{init})}$, is given by

$$v_j^{(\mathrm{init})} = w_j v_j^{(\mathrm{log})} + (1 - w_j) v_j^{(\mathrm{tt})}, \tag{3.12}$$

where $v_j^{(\mathrm{log})}$ is the logging velocity, $v_j^{(\mathrm{tt})}$ is the velocity obtained from travel time tomography, and w_j is the weighting coefficient. The weight coefficient w_j, as shown in Figure 3.9, is set according to the horizontal distance, as shown in Chapter 2.

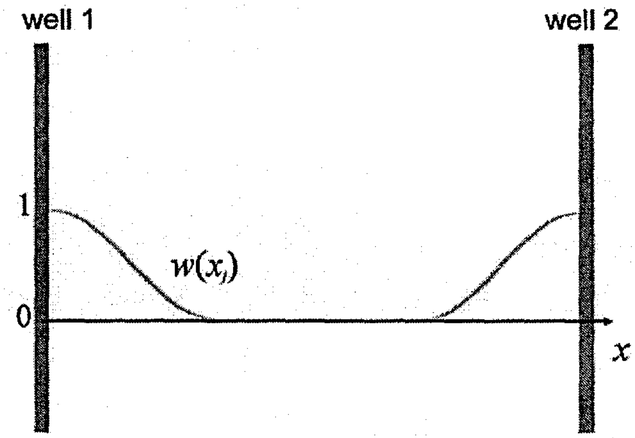

Figure 3.9 The diagrammatic curve of the relation between the weight coefficient and the horizontal distance.

I generate the well-log constrained initial model shown in Figure 3.10a, where the logging velocity $v_j^{(\log)}$ for the initial model building has been low-pass filtered. The trade-off parameter is set as $\mu = 0.3$, following chapter 2. Then, using exactly the same running parameters as those used in the experiment two above, I obtain the well-log constrained velocity images, shown in Figure 3.10b. In these images, the distinct layered structure with high/low velocities corresponds to the high and low velocity intervals in the well logs.

Comparing the inversion result with and without well-log constraint (Figures 3.10b and 3.8b), I see that the inversion procedure that I implemented has very weak dependency on the well-logging constraint but depends strongly on the inversion strategy. The similarity of the two results in fact reveals the importance of the three issues I discussed in the previous section for generating reliable inversion results from real seismic data, and the importance of correctly setting up the initial model and the inversion strategy (using a group of frequencies simultaneously and a model smoothness constraint).

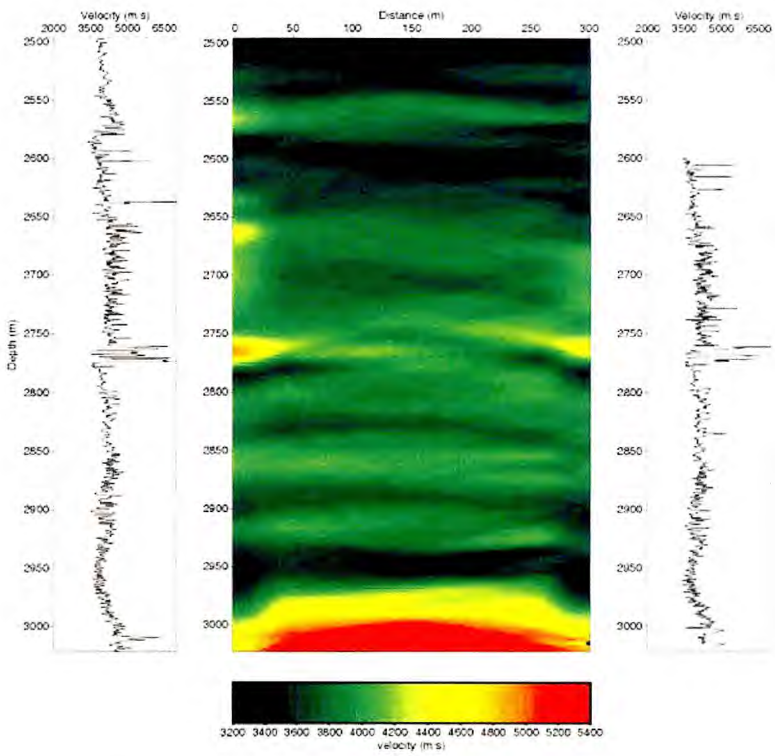

(a)

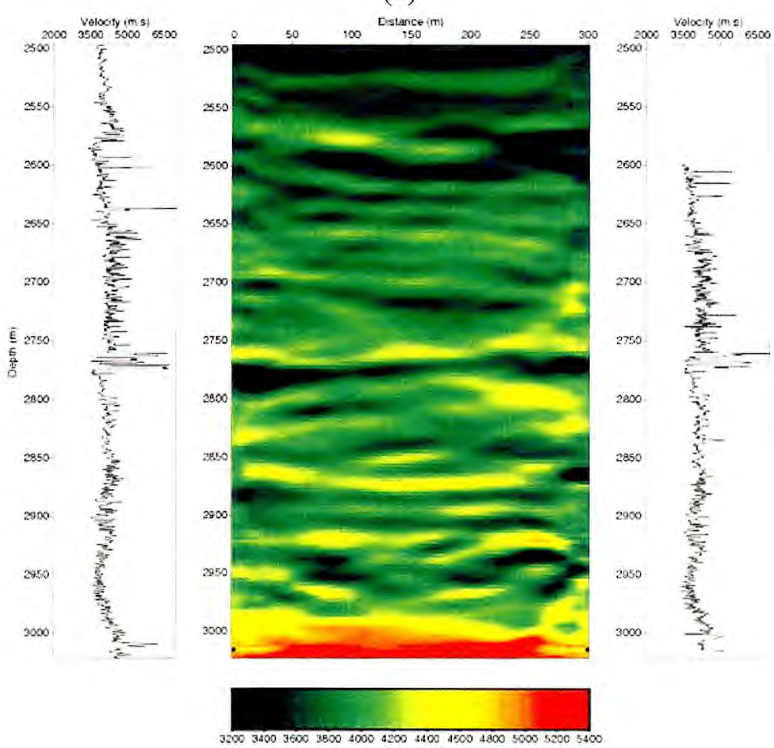

(b)

Figure 3.10 Logging constrained waveform tomography. (a) The initial model set as the mixture of well-log information of two boreholes and the traveltime inversion result. (b) The final waveform tomography result, after using all of the frequency groups in sequence. The trade-off parameter is set as $\mu = 0.3$, following chapter 2.

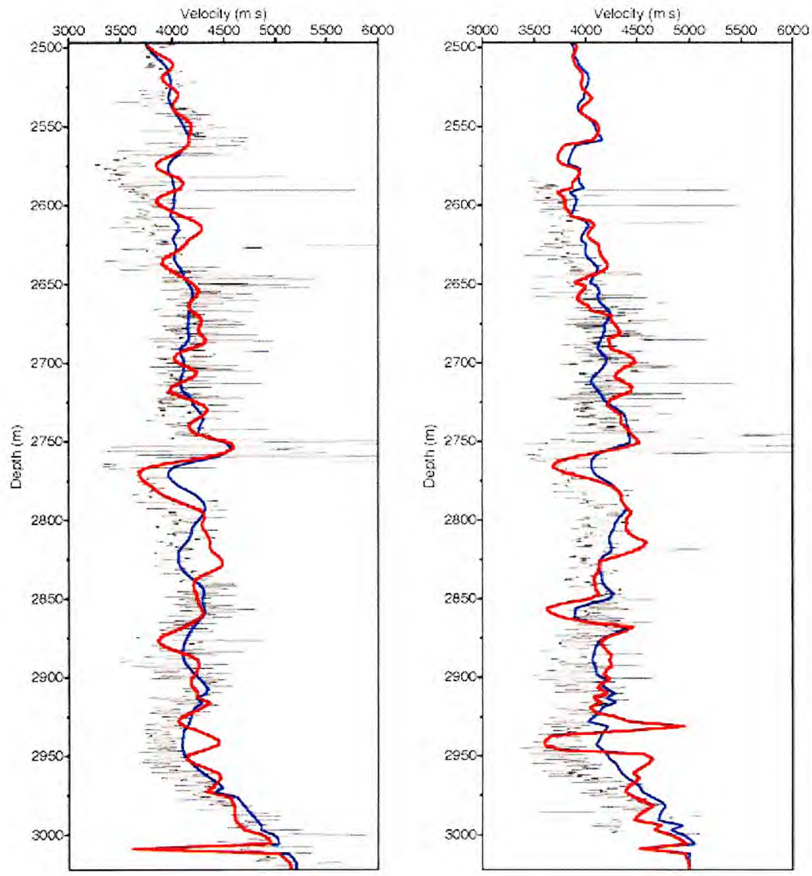

(a) (b)

Figure 3.11 Velocities from sonic logging in the boreholes (dark lines) compared with traveltime tomography (blue lines) and waveform tomography (red lines), where (a) and (b) correspond to two boreholes, respectively.

In Figure 3.11, I compare the traveltime inversion result (blue lines) and waveform tomography result (red lines) both against velocity curves from sonic logging in the boreholes (thin solid lines). I can see clearly that the traveltime inversion result is the long wavelength background velocity measured by the sonic log and the waveform inversion result. It indicates that the traveltime inversion result is indeed a good initial model to use for waveform inversion.

3.6 Conclusions

In this Chapter I have discussed the practical application of crosshole seismic waveform tomography when dealing with real data. I have analyzed and verified that the following three issues are important for real data waveform tomography, compared to waveform tomography of synthetic data or traveltime tomography on both synthetic and real data.

(1) A good initial model is essential for the success of waveform tomography, since in most cases real crosshole seismic data do not contain low frequency components (<190 Hz in the example presented).

(2) A smoothness constraint must be used in waveform tomography of real seismic data, to combat the effect of data noise, the effect of uneven distribution of ray density, the effect of the strong sensitivity to short wavelength components of velocity model, and the non-linearity of the problem.

(3) It is necessary to invert a group of frequencies simultaneously at each inversion stage, to further mitigate the effect of data noise. The inversion result then appears much better, in terms of interpretability, than that using single frequencies in sequence (Pratt and Shipp, 1999).

After successful waveform tomography with consideration of the above three issues, I have also brought in the sonic log information as a geological constraint in the inversion. The result is similar to the inversion without the well-log constraint. The reliability of waveform inversion without the well-log constraint in fact indicates the importance of the three issues in the waveform inversion when I deal with the application to real seismic data.

The material in this chapter has been published in *Geophysical Journal International*, 2006, Vol. **166**, pages 1224-1236.

Chapter 4

Resolution analysis for waveform inversion

4.1 Introduction

Waveform tomography is a powerful tool that can yield quantitative images of physical properties of the earth media. Compared to traveltime tomography, a velocity image generated by waveform tomography will have significantly better resolution. However, one significant question remains, "how reliable is the velocity image, and can I use it to make a direct geological interpretation?" Can I use the observed velocity contrasts to distinguish individual geological layers? In this chapter, I conduct a series of checkerboard tests on a waveform tomographic velocity model that was obtained from a real crosshole seismic data set. The aims of these tests are to reveal the resolving power of the inversion when dealing with real data, and to provide an indication of reliability of the inversion result.

Generally speaking, a geophysical tomographic solution is not unique. It depends on the quality of the data, data selection, the inversion method employed, and the model parameterization. Tomographic resolution can be very poor in regions where the distribution of sources and receivers is irregular. Additionally, it is common to apply model constraints to the inverse problem to produce a practical solution. The effect of these factors upon the inversion solution is difficult to quantify, especially when dealing with real seismic data. It is thus questionable whether I can use the final velocity model to infer the earth's properties correctly.

In this Chapter I use checkerboard tests to verify the final velocity model obtained from a waveform tomographic inversion. Checkerboard testing has been used commonly in traveltime tomography (Inoue *et al.,* 1990; Zelt, 1998; Zelt and Barton, 1998; Morgan *et al.*, 2002), but has not yet been used in an application of waveform tomography to real seismic data. I set up a checkerboard consisting of rows and columns of alternating positive and negative velocity anomalies, superimposed on the final velocity model. The velocity perturbations are a percentage of the actual velocity value, and thus are spatially varying. I generate a synthetic data set based on the checkerboard, and then invert these data, using exactly the same method, procedure, constraints, and parameterization as used for the tomographic inversion of the real data. Resolvability at any point of the model space is defined in terms of the ratio of recovered velocity anomaly to the real velocity perturbation.

In the resolution analysis tests, I test the effect of: the reference-model constraint, the model smoothness constraint, and the effect of the combination that I applied in the inversion of the real data. I also mimic the real data acquisition with an irregular source/receiver geometry. Then I test the effect of irregular ray coverage in the real experiment by setting up an ideal crosshole configuration, consisting of regular sources for each of the cells in one borehole and regular receivers spanning all cells at the other borehole. Finally, I test the effect of varying the magnitude of the velocity perturbation and the cell-size of the checkerboard.

4.2 Real data waveform tomography

A waveform tomography example with real data is presented in Chapter 3. In this real data example, the two boreholes are parallel and 300 m apart. The depth range that I choose to invert for is from 2497 to 3022 m. In the inversion, I have 175 source points in one vertical borehole and 175 receiver points in the other. Source intervals and receiver intervals are both 3 m.

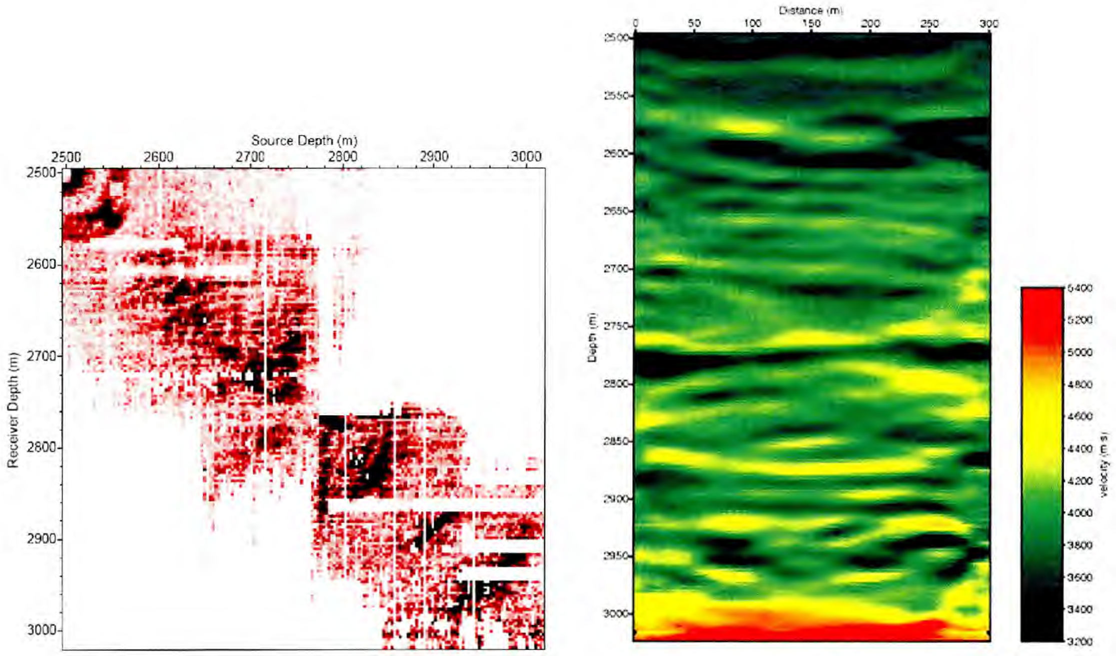

(*a*) (*b*)

Figure 4.1 (a) Amplitudes of the real crosshole seismic data at frequency 260 Hz. The data vector $\mathbf{P}_{\mathrm{obs}}$ in the frequency domain waveform tomography. (b) The velocity model generated from waveform tomography from Figure 3.8b.

Following Pratt (1999), Pratt and Shipp (1999), Ravaut *et al.* (2004), and Sirgue and Pratt (2004), the waveform tomography is performed in the frequency domain. Figure 4.1a shows the amplitudes of the real crosshole seismic data at frequency 260 Hz. In the inversion, I divide the velocity model into 100 × 175 cells with a cell size of 3 m, which is equal to the source and receiver interval. I use a traveltime inversion result as an initial model, and obtain the final velocity model shown in Figure 4.1b. The layer structure in the middle part of image appears laterally continuous across the section. Deeper layers are discontinuous and faulted. A number of low-velocity layers also appear on the image. The waveform tomographic image in Figure 4.1b contains velocity contrasts that may reflect individual geological layers, but the question of model reliability remains.

As described in chapter 3, I have used a number of constraints in the real data inversion to combat problems with the data noise, uneven ray coverage and the non-linearity of the problem. The inverse problem is based on the minimization of a least-squares objective function as the following:

$$
\begin{aligned}
J(\mathbf{m}) = & [\mathbf{P}(\mathbf{m}) - \mathbf{P}_{\text{obs}}]^H \mathbf{C}_{\text{D}}^{-1} [\mathbf{P}(\mathbf{m}) - \mathbf{P}_{\text{obs}}] \\
& + \mu (\mathbf{m} - \mathbf{m}_0)^H \mathbf{C}_{\text{M}}^{-1} (\mathbf{m} - \mathbf{m}_0),
\end{aligned} \tag{4.1}
$$

where the superscript ^{H} denotes the complex conjugate transpose. This objective function consists of two parts. In the first part, the data minimization term, $\mathbf{P}_{\text{obs}}$ is a vector of the observed data in the frequency domain, and $\mathbf{P}(\mathbf{m})$ is a vector of the forward modelled data for the current model $\mathbf{m}$, and $\mathbf{C}_{\text{D}}$ is the covariance operator in the data space with units of $(data)^2$, which defines the estimated uncertainties in the data set. In the second part, the model constraint term, $\mathbf{m}_0$ is a reference model, $\mathbf{C}_{\text{M}}$ is called the model covariance matrix with units of $(model\ parameter)^2$. The scalar μ is a trade-off parameter that controls the relative weights of the data contribution and the reference-model constraint.

Introducing a smoothness constraint in the inversion, I may express the objective function as

$$
\begin{aligned}
J(\mathbf{Dm}) = & [\mathbf{P}(\mathbf{Dm}) - \mathbf{P}_{\text{obs}}]^H \mathbf{C}_{\text{D}}^{-1} [\mathbf{P}(\mathbf{Dm}) - \mathbf{P}_{\text{obs}}] \\
& + \mu (\mathbf{Dm} - \mathbf{m}_0)^H \mathbf{C}_{\text{M}}^{-1} (\mathbf{Dm} - \mathbf{m}_0),
\end{aligned} \tag{4.2}
$$

where $\mathbf{D}$ is a dimensionless smoothing operator. Denoting $\tilde{\mathbf{m}} = \mathbf{Dm}$, I have

$$
\begin{aligned}
J(\tilde{\mathbf{m}}) = & [\mathbf{P}(\tilde{\mathbf{m}}) - \mathbf{P}_{\text{obs}}]^H \mathbf{C}_{\text{D}}^{-1} [\mathbf{P}(\tilde{\mathbf{m}}) - \mathbf{P}_{\text{obs}}] \\
& + \mu (\tilde{\mathbf{m}} - \mathbf{m}_0)^H \mathbf{C}_{\text{M}}^{-1} (\tilde{\mathbf{m}} - \mathbf{m}_0),
\end{aligned} \tag{4.3}
$$

the same expression as the objective function (4.1).

In the waveform tomography, I have used a reference-model constraint and a model smoothness constraint. In order to assess their effects on waveform tomography, I set up a series of checkerboard tests to test the capability of waveform tomography in reconstructing the velocity anomalies.

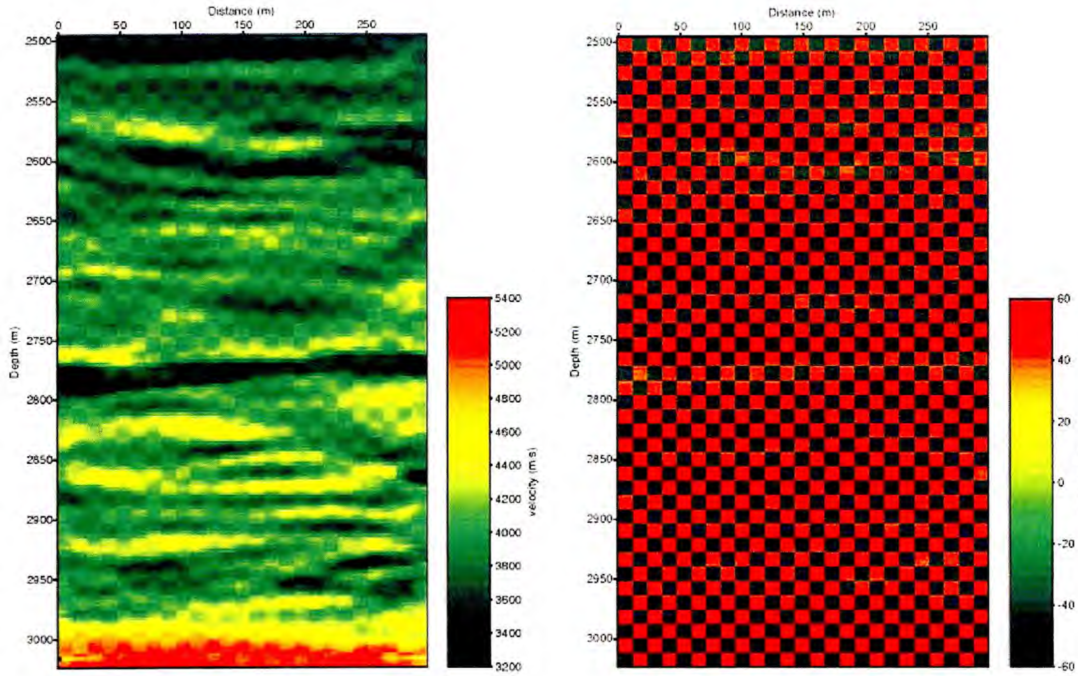

(*a*) (*b*)

Figure 4.2 (a) A perturbed velocity model generated by adding ±1% velocity perturbation to the waveform inversion result of Figure 4.1b. (b) Velocity perturbation pattern, with checkerboard anomaly size of 12 m.

4.3 Checkerboard test on the inversion result

I design a checkerboard velocity model as shown in Figure 4.2a, by superimposing an alternating pattern of positive and negative anomalies on to the final inversion model (shown in Figure 4.1b). The perturbation shown in Figure 4.2b is calculated based on the final velocity model with a constant percentage and thus the perturbation magnitude is spatially varying. To start with I choose a small perturbation of only $\pm 1\%$, so that the iterative procedure of waveform inversion satisfies linear conditions.

My inverse problem is now to perform the waveform tomography a step further, using exactly the same strategy and parameters as I used in the real data inversion, to see whether the inversion is able to recover the perturbation imposed onto the velocity model.

Test 1: inversion with reference-model constraint only

In this first test, I use the objective function in equation 4.1, which includes data minimization and a reference-model constraint. The reference model $\mathbf{m}_0$ I use in the inversion is the real data inversion result without perturbation (Figure 4.1b), and the trade-off parameter is set as $\mu = 0.3$, following chapter 2. The initial model $\mathbf{m}_0$ is the model that is 'close' to the real solution (the perturbed model, Figure 4.2a).

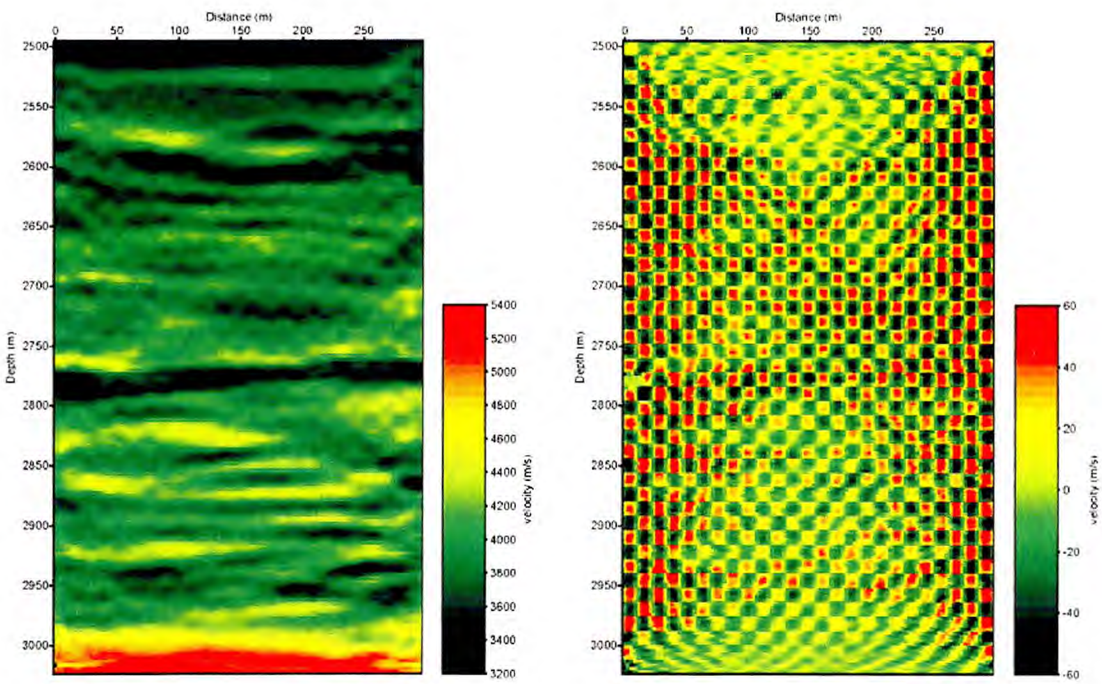

(*a*) (*b*)

Figure 4.3 Test 1, inversion with reference-model constraint only. (a) The reconstructed velocity image. (b) Recovered perturbation pattern.

Figure 4.3a is the reconstructed velocity model, and Figure 4.3b is the recovered perturbation pattern. The top and bottom portions of the model are not well resolved, as there are no sources/receivers at the top and bottom edges of the model. In most parts of the model, the vertical resolution is better than the horizontal resolution, as I can see that the anomaly boundary between positive (red) and negative (dark) pixels is defined sharply in the vertical direction but relatively blurred in the horizontal direction.

As the reference model and initial model are close to the solution (only $\pm 1\%$ difference) and the input data are noise free, I would expect the result of this test to be the same as the one without using a model constraint (I conducted the experiment and found that the difference between two was indeed negligible). However, when I deal with real data, the use of a model constraint is justified as it prevents divergence in the inversion process from divergence, caused by data noise and the non-linearity of the problem. I use the inversion result of Test 1 as a benchmark for other inversion tests with different constraints.

Test 2: the combined effect of reference-model constraint and smoothness constraint

Test 2 is the same as Test 1 but also includes a 3×3 velocity smoothing operator, as described in section 3.4. For frequency domain waveform tomography, the smoothness constraint must be used with real data, in order to generate a reasonable solution.

I obtain the velocity model in Figure 4.4a, with the recovered perturbation pattern shown in Figure 4.4b. Use of the smoothness constraint results in reduced resolution, as The velocity perturbation is averaged at the boundaries between neighbouring anomaly pixels and the recovered perturbation pattern is not as sharp as in Test 1, especially in the middle part far away from the two boreholes. Adding some constraint between the two wells, such as a sonic log data constraint, could might uncertainty in inversion, but tests in the Chapter 3 suggest that a well-log constraint has less effect on the final result of waveform inversion than in traveltime inversion. More iterations might help in this case but, for a direct comparison between tests, I still use five iterations for the inversion of each frequency group.

However, use of the smoothness constraint is likely to improve the stability of the inversion in real data cases. Hence, in the next test, I try to optimize the application of the reference-model constraint and the velocity smoothing operator in an inversion.

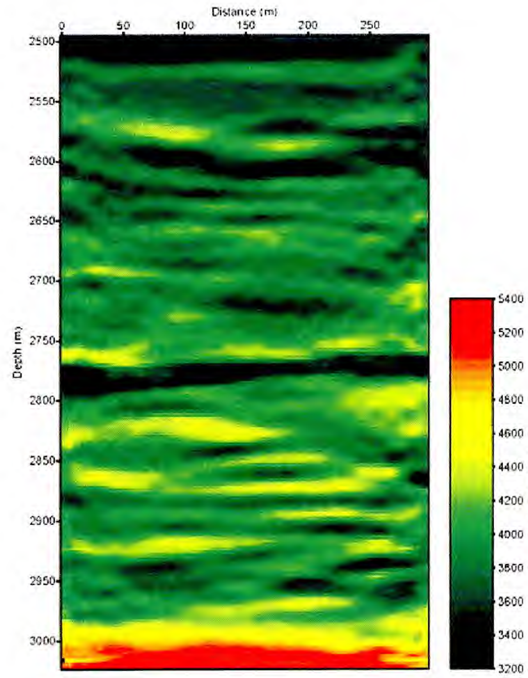

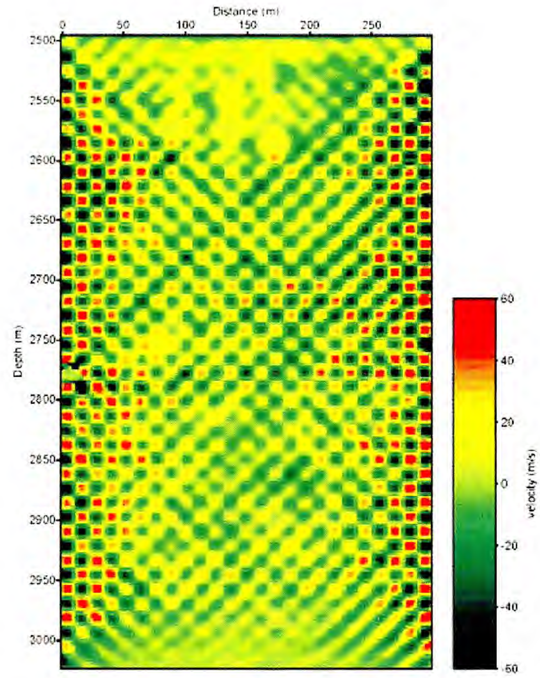

(*a*) (*b*)

Figure 4.4 Test 2, the effect of smoothness constraint. (a) The reconstructed velocity image. (b) Recovered perturbation pattern.

Test 3: an optimal use of the two constraints

In Test 3, I use the reference-model constraint and the smoothness constraint together for the first three iterations but only the reference-model constraint for the subsequent two iterations.

The result shown in Figure 4.5 is significantly better than the result of Test 2 (Figure 4.4). Comparing the result of Test 3 with the result of Test 1 (Figure 4.3), I also see that the shape of the variable velocity boundaries has been better recovered, especially in the middle portion of the two wells. In fact the result of Test 3 is close to optimal, as it is very similar to the result of Test 1 which is without the smoothness constraint.

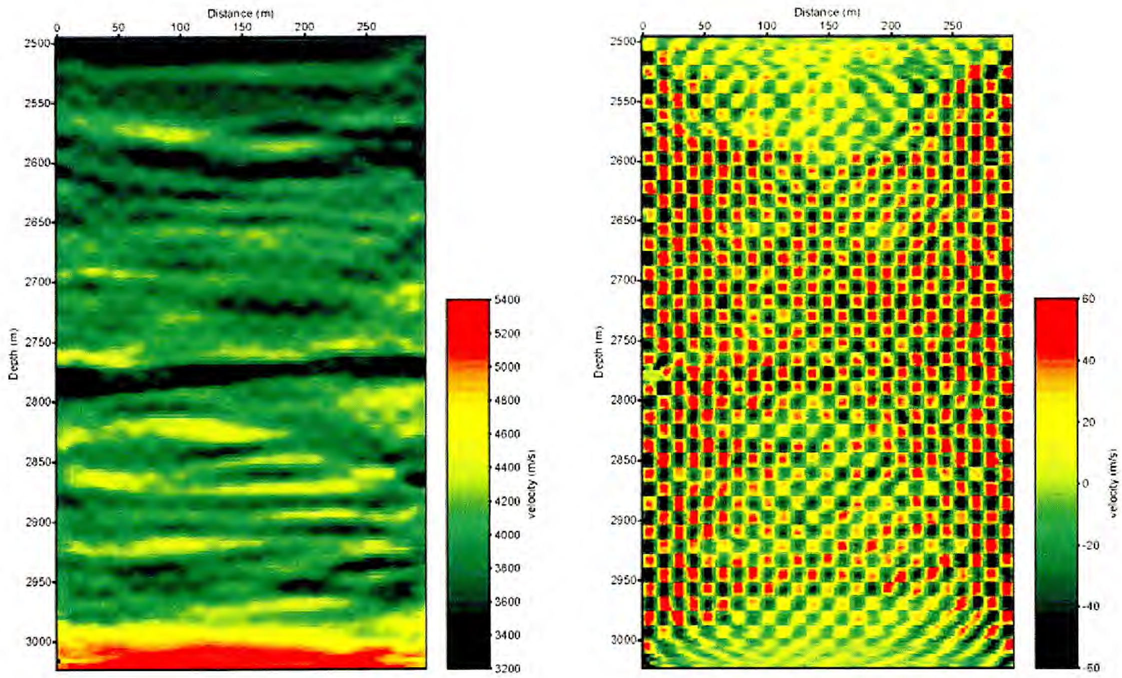

(a) *(b)*

Figure 4.5 Test 3, an optimal use of the reference-model and smoothness constraints. (a) The reconstructed tomographic image. (b) Recovered velocity perturbation pattern.

Test 4: the effect of ray coverage

In the previous three tests, I mimicked the true acquisition configuration in the real data case, as shown in Figure 4.1a, in which many traces were missing. That is, for each shot, I did not have exactly 175 receivers at the receiver borehole. Therefore I edited the synthetic dataset by decimating some traces prior to inversion. Figure 4.6a displays the ray coverage, defined in terms of ray density, the (normalized) total length of (curved) ray segments that pass through each cell. To test the effect of the original ray coverage, I now set up Test 4 with an ideal acquisition geometry where, for each shot, I have exactly 175 receivers spanning over the receiver borehole. In this way, I have the maximum ray coverage, as shown in Figure 4.6b, for the case with two parallel vertical boreholes.

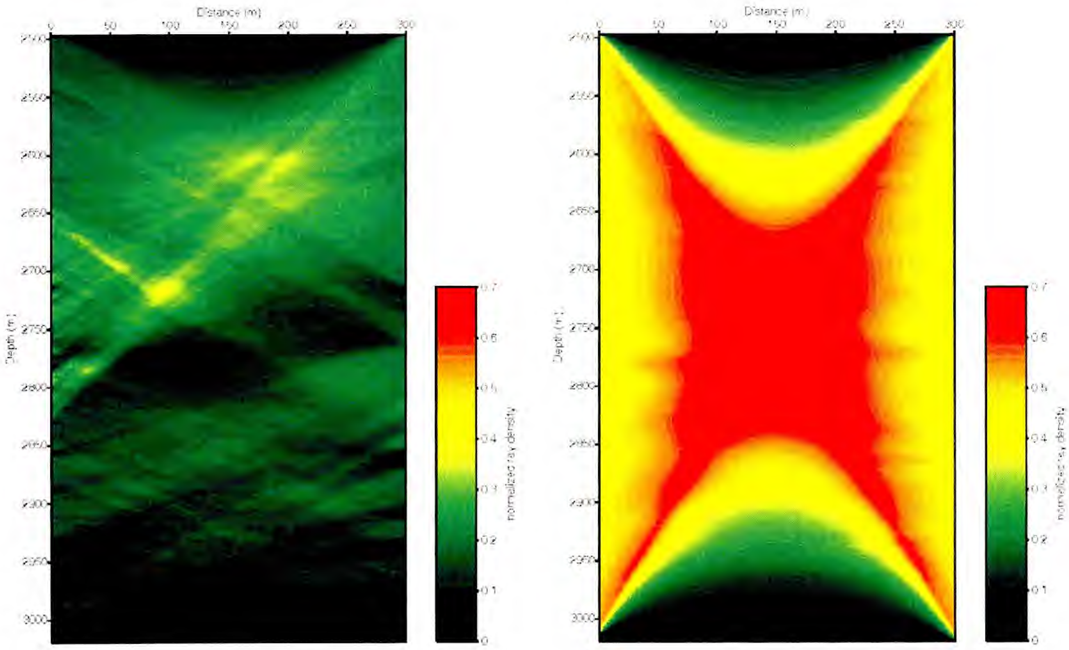

(*a*) (*b*)

Figure 4.6 (a) The ray coverage of the actual acquisition geometry with irregular source and receiver distribution. (b) The ray coverage of an ideal acquisition geometry with regularly distributed sources and receivers. The ray coverage is calculated within a 3×3 m cell size.

In Test 4, I simply repeat the inversion procedure of Test 3, i.e., three iterations with both the reference-model constraint and the smoothness constraint, followed by two iterations using only the model constraint. The result is shown in Figure 4.7, which is better than the result of Test 3 shown in Figure 4.5, especially the middle portion at the 2800-2950 m in depth, where the ray coverage is much better with the regular geometry than it is for the irregular geometry of the actual data set.

It seems straightforward that a better ray coverage will result in a better recovery of the perturbation pattern in waveform tomography. But more importantly, this test demonstrates that regions with poor recovery in Test 3 were not caused by the inversion strategy I adopted.

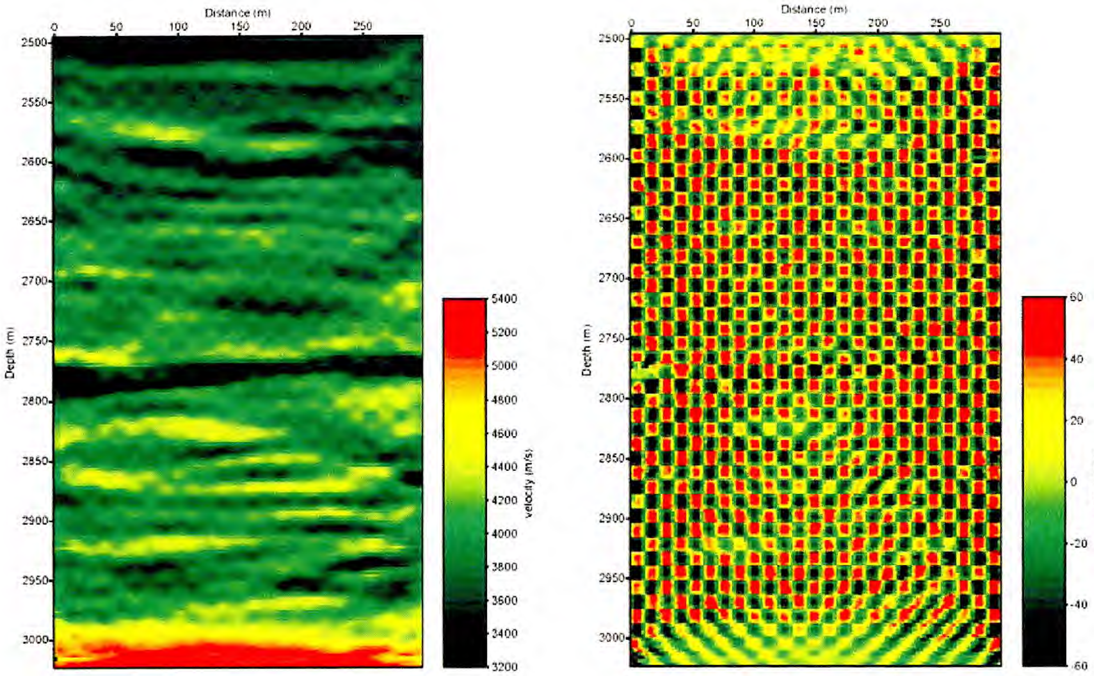

(*a*) (*b*)

Figure 4.7 Test 4, the effect of ray coverage. (a) Reconstructed tomographic image. (b) Recovered perturbation pattern which, due to a better ray coverage, is better than the result of Test 3 (Figure 4.5b).

4.4 Resolvability analysis

In order to quantitatively assess the resolving power of the waveform inversion, I now compare the reconstructed and real velocity models. I define a measurement at a node as

$$R = \sqrt{\sum_{i=0}^{M} \Delta\widetilde{v}_i^{\,2}} \Big/ \sqrt{\sum_{i=0}^{M} \Delta v_i^{\,2}}\ , \tag{4.4}$$

where Δv_i are the true velocity perturbations, and $\Delta\widetilde{v}_i$ are the recovered velocity perturbations. I refer to the measurement R, calculated within a rectangle space in the (x, z) plane, as the 'resolvability', as it indicates the ability of the inversion to recover the given perturbation at any particular point in the model.

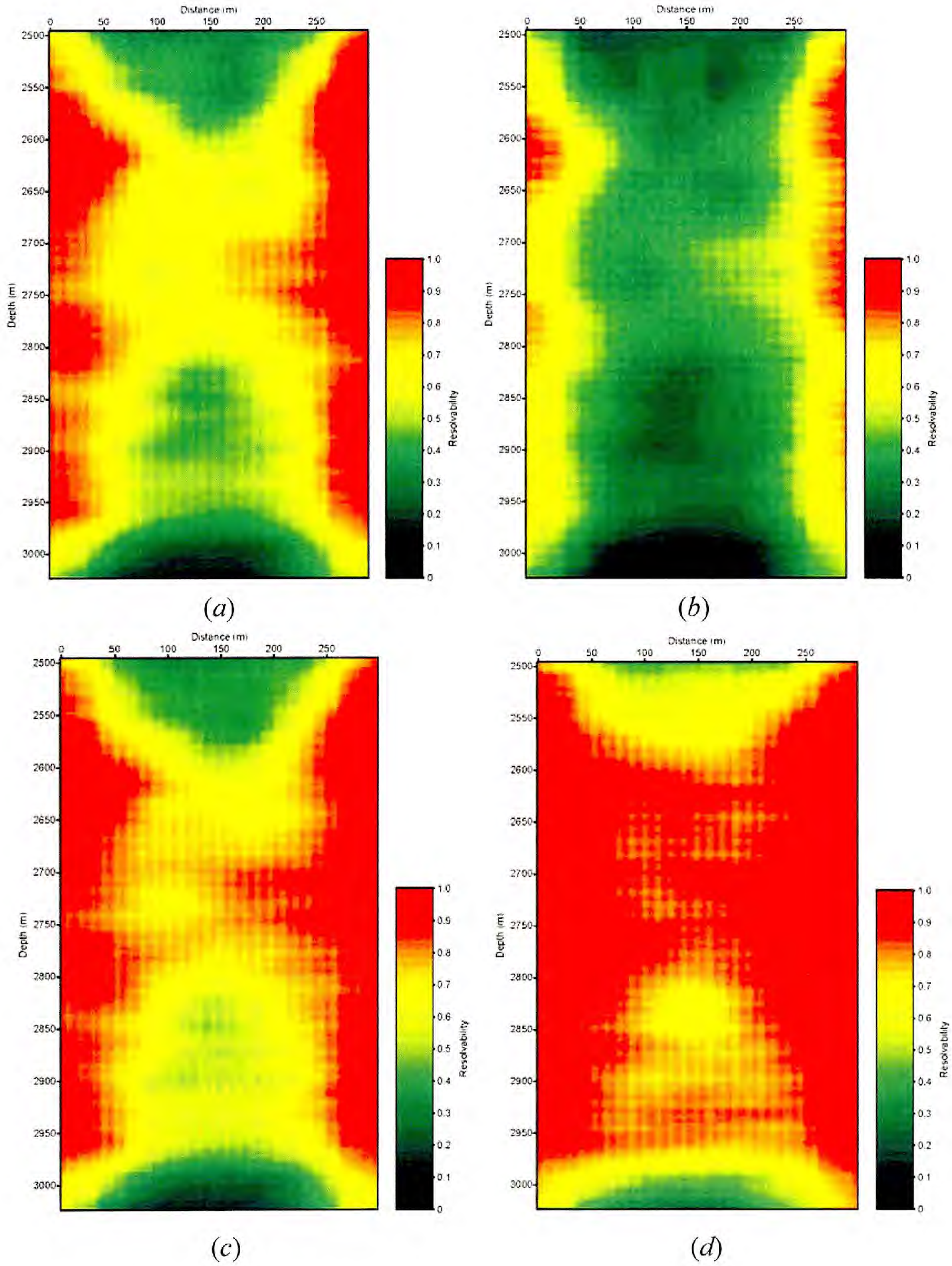

Figure 4.8 Resolvability analysis of Test 1 (a), Test 2 (b), Test 3 (c) and Test 4 (d). Test 3 has an optimal resolvability when inverting with the true acquisition configuration, and Test 4 has the best resolvability if I have an ideal acquisition geometry with a good ray coverage.

Figure 4.8 is a quantitative representation of the resolving power of the inversion. Resolvability above 0.6 indicates a well-recovered checkerboard structure. When estimating the resolvability R, I use $M = 5\times5 = 25$ around any specific node, which is small enough to reflect a local similarity between the true and reconstructed models. Since the grid spacing is approximately $< \lambda/4$, a quarter of a wavelength, the size of the resolvability patch is roughly one wavelength in size. The shortest spatial wavelength that can be recovered from crosshole tomography is a half wavelength (Wu and Toksöz, 1987). The resolvability defined here is actually a ratio of zero-lag 2D auto-correlations of velocity perturbations, and the radius of the patch is almost exactly a half of the wavelength.

Compared with Tests 1 and 2 (Figures 4.8a and 4.8b respectively), Test 3 (Figure 4.8c) has a better resolving power, as the resolvabilities of the middle portion between 2750 and 2950 m in depth and the portion between 2550 and 2600 m in depth have been improved. Test 4 (Figure 4.8d) shows the best resolvability, if I have an ideal acquisition geometry with better ray coverage than the actual data acquisition. Considering a real data case where the model constraint and smoothness constraint must be used in the inversion, Test 3 is an optimal choice for production use.

The resolvability in the checkerboard test above is a direct measure of the reliability of the final inversion result of the real seismic tomography shown in Figure 4.1b.

4.5 Resolution to different perturbation rates

Having tested the effects of different inversion constraints and the effects of different ray coverages, and concluded the strategy of Test 3 is optimal for the real data waveform inversion, I now summarize my tests on the resolving power of waveform tomography for increased velocity contrasts. I design a set of checkerboards with different amounts of velocity perturbation, and in the inversion I use the same scheme as Test 3 in the previous section.

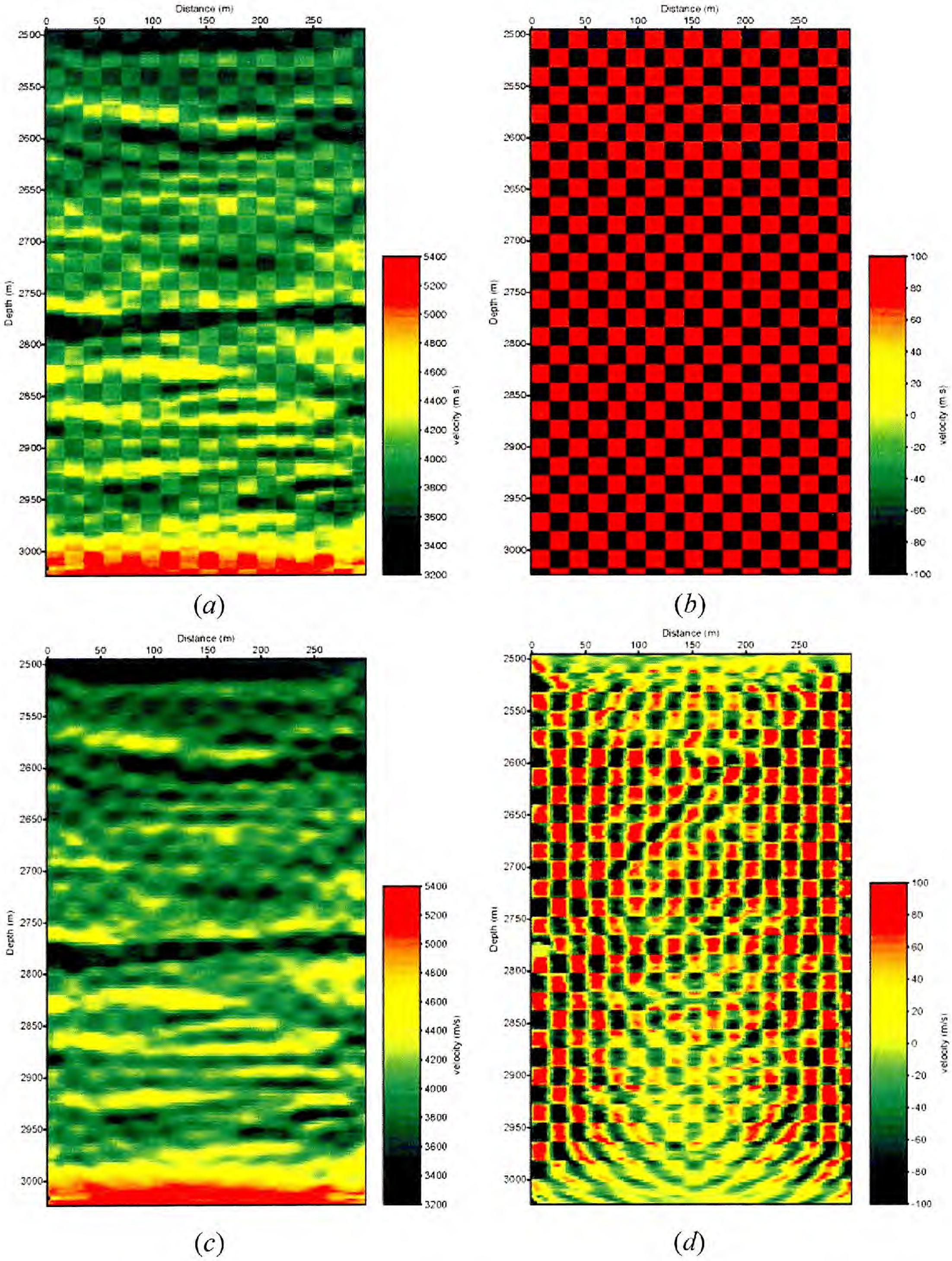

Figure 4.9 Waveform tomography with ± 2% velocity perturbation with checkerboard anomaly size of 18 m. (a) The perturbed velocity model, generated by adding ± 2% perturbation on the waveform inversion result. (b) Velocity perturbation pattern. (c) The reconstructed model from waveform tomography. (d) The recovered perturbation pattern.

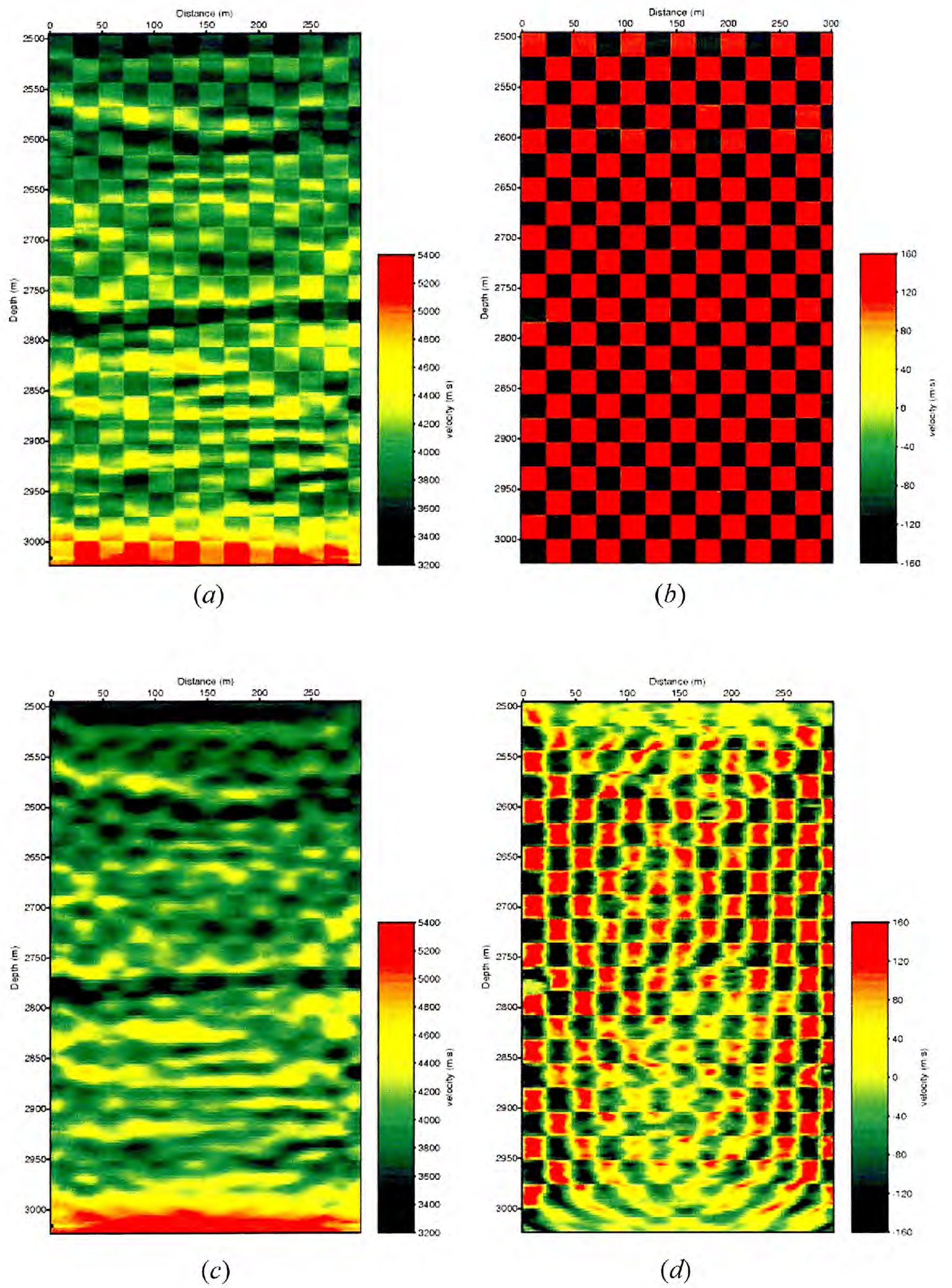

Figure 4.10 Waveform tomography with $\pm 3\%$ velocity perturbation with checkerboard anomaly size of 24 m. (a) The perturbed velocity model, generated by adding $\pm 3\%$ perturbation on the waveform inversion result. (b) Velocity perturbation pattern. (c) The reconstructed model from waveform tomography. (d) The recovered perturbation pattern.

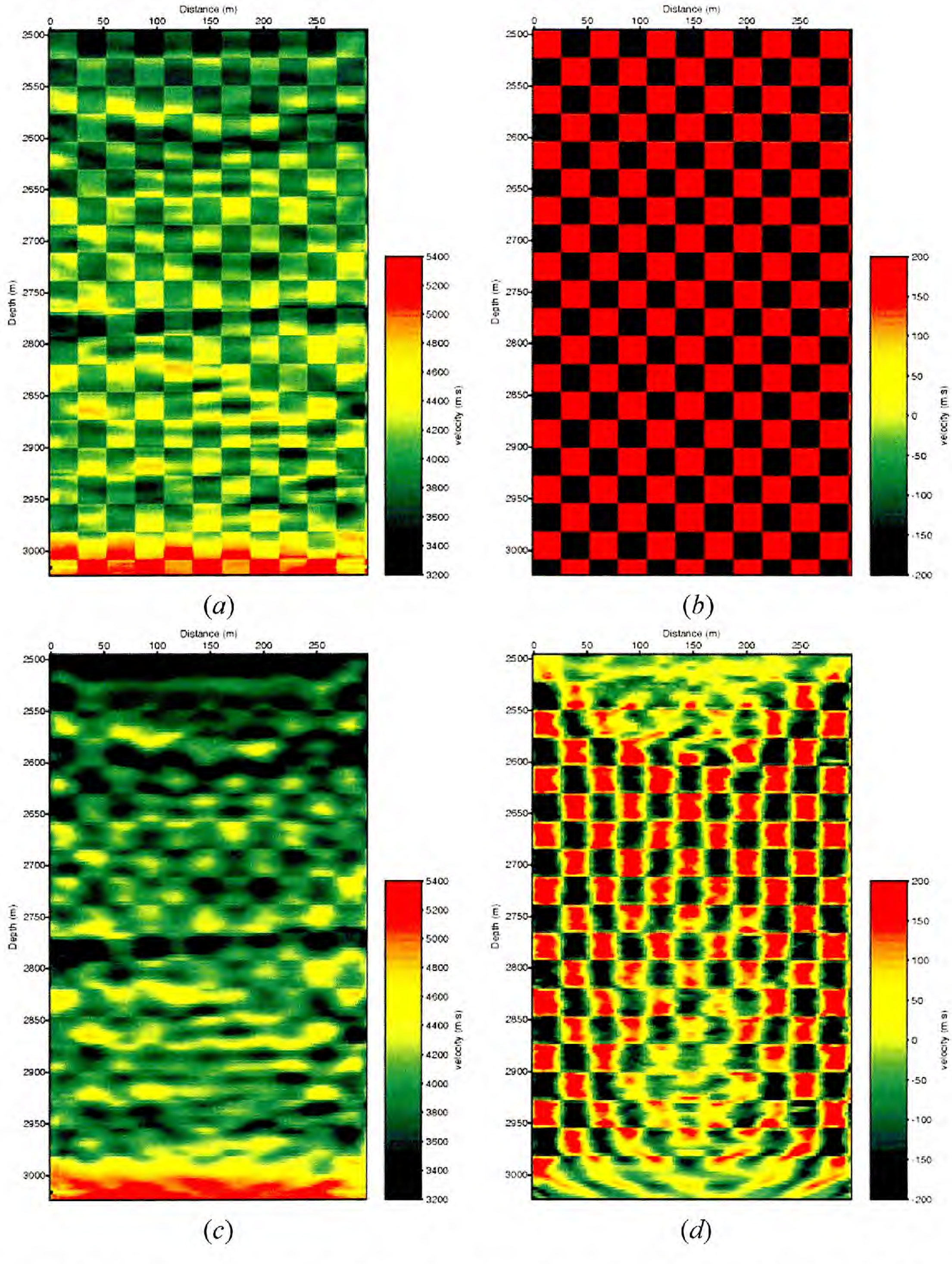

Figure 4.11 Waveform tomography with $\pm 4\%$ velocity perturbation with checkerboard anomaly size of 27 m. (a) The perturbed velocity model, generated by adding $\pm 4\%$ perturbation on the waveform inversion result. (b) Velocity perturbation pattern. (c) The reconstructed model from waveform tomography. (d) The recovered perturbation pattern.

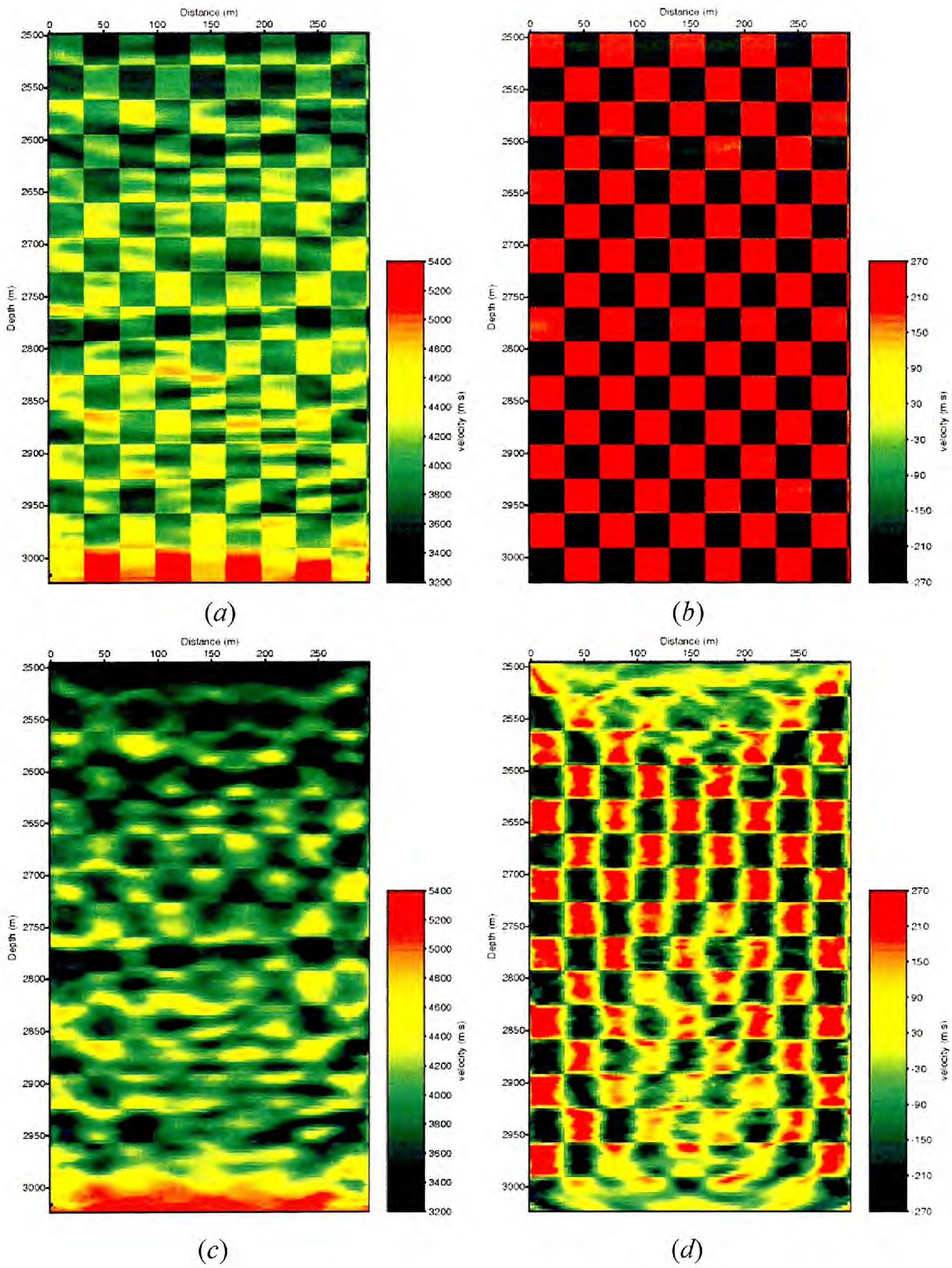

Figure 4.12 Waveform tomography with $\pm 5\%$ velocity perturbation with checkerboard anomaly size of 33 m: (a) The perturbed velocity model, generated by adding $\pm 5\%$ perturbation on the waveform inversion result. (b) Velocity perturbation pattern. (c) The reconstructed model from waveform tomography. (d) The recovered perturbation pattern.

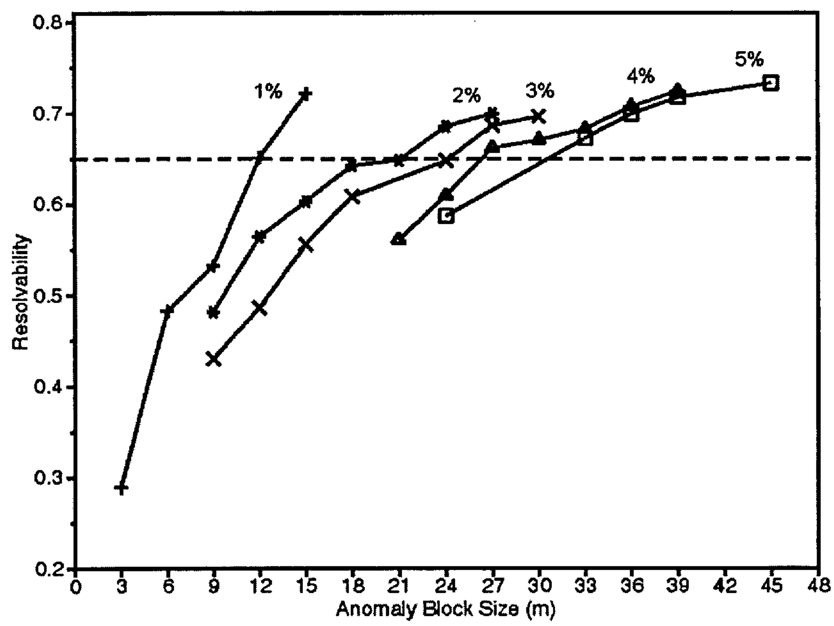

Figure 4.13 A comprehensive summary of the experiments on the resolvability against the anomaly block size, for different perturbation rates. The resolvability value is an average over entire region, and the horizontal axis is the size of the anomaly block I designed in perturbed velocity models. Each sample along a curve represents a full inversion of waveform tomography, and this plot contains 30 such full inversion processes in total.

Figures 4.9-12 show four tests with different velocity perturbation rates: $\pm 2\%$, $\pm 3\%$, $\pm 4\%$ and $\pm 5\%$. Each figure shows the perturbed velocity model (a), velocity perturbation pattern (b), the reconstructed checkerboard model (c), and correspondingly the recovered perturbation pattern (d). Note that each perturbation pattern display has a different colour scale, as the amount of velocity anomaly differs. Note also that the anomaly block sizes are different for different perturbation magnitudes. The anomaly block sizes that I use in Figures 4.9-12 are 18, 24, 27 and 33 m, corresponding to $\pm 2\%$, $\pm 3\%$, $\pm 4\%$ and $\pm 5\%$ velocity perturbations, respectively.

Figure 4.13 provides a comprehensive summary of the experiments I have conducted that have measured resolvability for different checkerboard cell sizes (3 – 45

m) and different perturbation rates (from 1% through 5%). The resolvability value presented is an average over the entire region, and the horizontal axis is the checkerboard cell-size. Each sample along a curve represents the result from a complete waveform inversion, and this plot contains 30 such inversions in total. The dashed line represents an average resolvability of 0.65. The checkerboard test results shown in Figures 4.9-12 are those that occur around this line.

From this set of tests, I have two straightforward observations. (1) For a fixed perturbation rate, longer-wavelength variations are better recovered. (2) As the velocity perturbation is increased, the smallest checkerboard size that can be well-resolved also increases. These observations suggest that, when I discuss the resolution defined in terms of the wavelength of an anomaly, I need to consider its magnitude as well. That is, I should consider a normalized wavelength or a ratio of wavelength to magnitude of an anomaly in the context of waveform tomography.

4.6 Conclusions

In this chapter, I have conducted a series of checkerboard tests to assess the performance of waveform tomography in the inversion of real crosshole seismic data. I have made a quantitative measurement of resolvability to investigate the reliability of the inversion, and to provide an indication of degree of confidence in the inverted velocity field.

The resolvability analysis assists us in designing an appropriate inversion strategy. For example, when using both the reference-model and smoothness constraints in the inversion of real data, if I use both constraints first and then relax the smoothness constraint at later iterations, I can obtain an optimal solution. I can further improve the resolvability with a regular source/receiver geometry. .

In addition, the resolvability analysis reveals that, for different amplitudes in velocity perturbation, the spatial resolution differs significantly. A good recovery of the velocity perturbation was only possible when the spatial size of the positive and negative anomalies was increased proportionally with perturbation amplitude.

In summary, checkerboard tests and resolvability analyses can be used to guide the geological and lithological interpretation of features shown in waveform tomographic images.

The material in this chapter has been published in *Geophysical Journal International*, 2006, Vol. **166**, pages 1237-1248.

Chapter 5

The effects of the earth attenuation on seismic waveform and waveform tomography

5.1 Introduction

In this chapter, I test the effects of the earth attenuation factor on waveform and on the waveform tomography. First, I investigate the effect on forward modelling. Then, I compare two attenuation inversion methods used in waveform tomography. The first method is inverting real-part velocity and fixing attenuation model ($1/Q$) first, using selected frequency components, then use reconstructed real-part velocity model as fix to invert the attenuation factor model. The other method is to invert for these two models simultaneously. There are no big differences in synthetic data tests. But because the trade-off between update of the real-part velocity and the attenuation factor is very sensitive to noise, there are big differences in real data tests, and the first method can successfully avoid cross contamination of the two fields. When the real dataset has strong attenuation, the choice of starting attenuation factor model is one critical issue for inversion. So I also test the effect of differing starting attenuation factor model on attenuation inversion results. The starting attenuation factor model, using a constant of zero everywhere, will be a reliable choice.

In practice, seismic data is always subject to high-frequency attenuation. For waveform tomography, there are two ways to deal with the attenuation effects. (1) Before I use seismic data as the input to waveform tomography, I can process the data for amplitude compensation and phase correction for both direct waves and scattered waves. This process is called inverse Q filtering (Wang, 2002, 2003a, 2006). (2) I can include the attenuation effects in the waveform tomography scheme. In frequency-domain waveform tomography it is easy to take the frequency-dependent attenuation into consideration (Song *et al.*, 1995; Pratt *et al.*, 2004).

In this study, I test the effects of the earth attenuation factor on the seismic waveform and on the waveform tomography. I investigate the attenuation effect on seismic waveform with forward modelling. Then, I compare two different strategies for waveform tomography when considering the attenuation effect. I also apply the waveform tomography method on a real data set, to invert for both velocity and attenuation models.

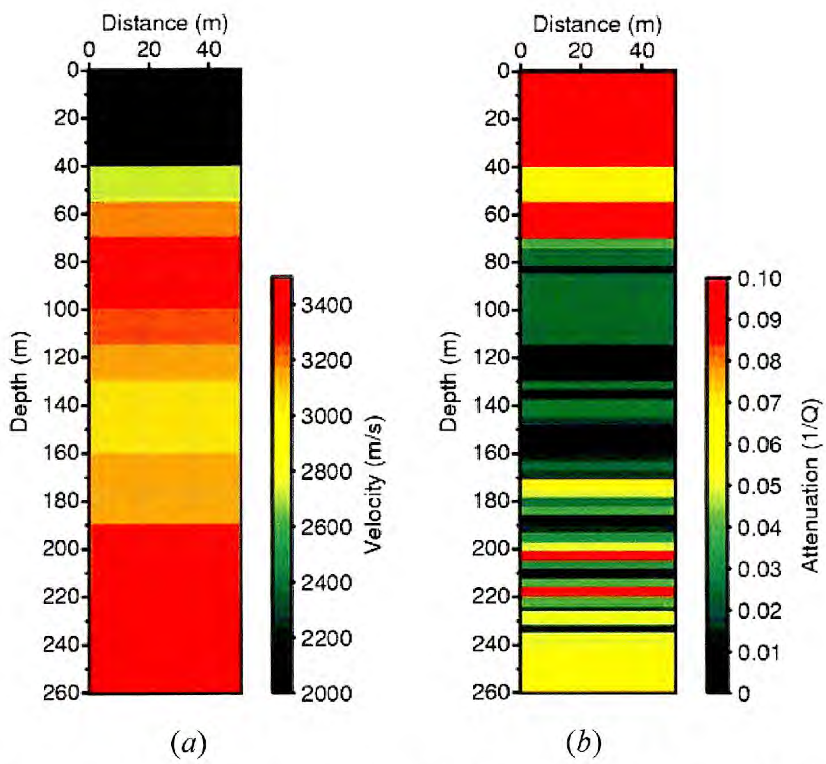

Figure 5.1 (a) A synthetic velocity model. (b) The corresponding synthetic attenuation factor ($1/Q$) model.

5.2 Complex velocity for attenuation

Frequency-domain waveform tomography can easily be adapted to include the attenuation effect. To do so, I may simply replace the real-valued velocities with complex velocities, and express the complex-valued velocity as

$$c(r) = c_R(r) + ic_I(r), \tag{5.1}$$

where $c_R(r)$ and $c_I(r)$ are respectively the real part and the imaginary part of the complex velocity $c(r)$, and r is the spatial position. Correspondingly, I have complex-valued wavenumber as

$$\begin{aligned} k &= k_R + ik_I \\ &= \frac{\omega}{c_R + ic_I} \\ &= \frac{\omega c_R}{c_R^2 + c_I^2} - i\frac{\omega c_I}{c_R^2 + c_I^2}. \end{aligned} \tag{5.2}$$

Then, I may express the frequency component of a plane wave at distance r as

$$\exp(ikr) = \exp\left(i\frac{\omega c_R r}{c_R^2 + c_I^2}\right)\exp\left(\frac{\omega c_I r}{c_R^2 + c_I^2}\right), \tag{5.3}$$

where the second exponential term in the right-hand side represents the attenuation along distance r. According to Aki and Richards (1980), I may define the quality factor Q using

$$A(r) = A_0 \exp\left(-\frac{\omega r}{2c_R Q}\right), \tag{5.4}$$

where A_0 is the initial amplitude of the plane wave and $A(r)$ is the amplitude at distance r.

In practice, $c_R{}^2 >> c_I{}^2$, Following equations (5.3) and (5.4), I can describe the relationship between the quality factor Q, and the imaginary part of a complex velocity field as

$$\frac{1}{Q} \approx -\frac{2c_I}{c_R}. \tag{5.5}$$

Hence, in waveform tomography, I can recover the complex-valued velocity field first, and then calculate the effective attenuation field based on equation (5.5).

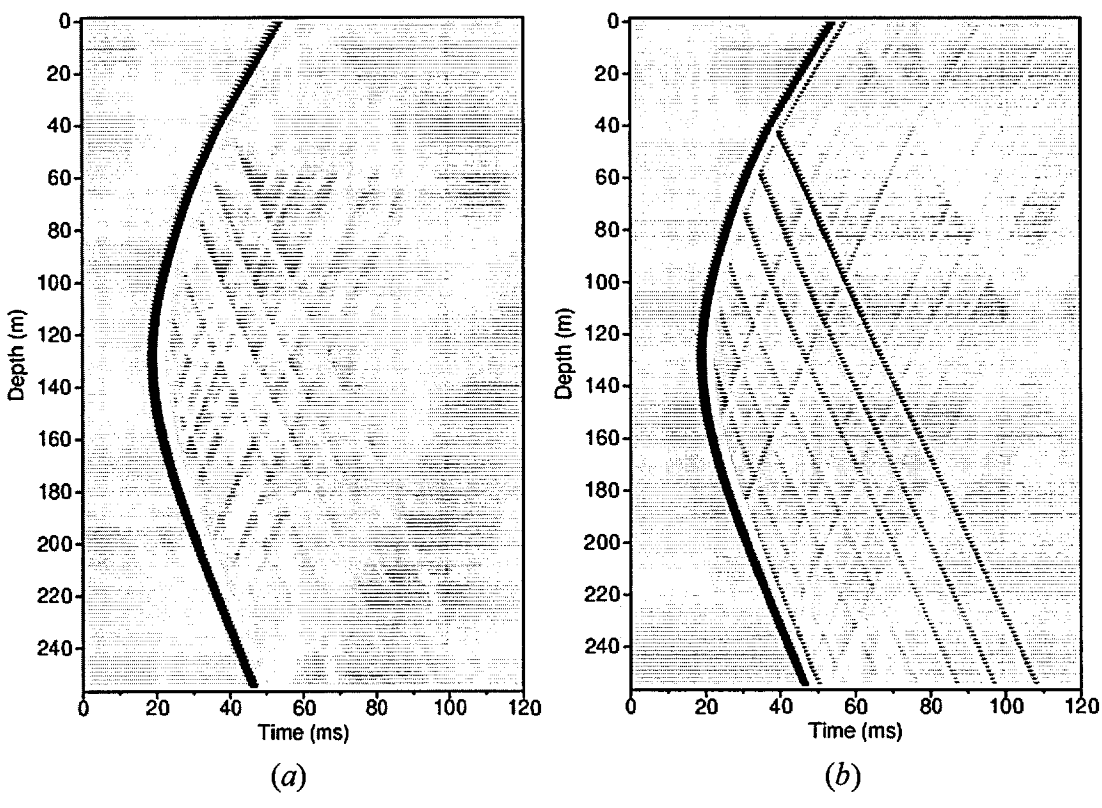

Figure 5.2 (a) Modelled shot gather generated from the velocity model in Figure 5.1a and the attenuation factor model in Figure 5.1b. (b) Modelled shot gather generated from velocity model in Figure 5.1a, without the attenuation effect.

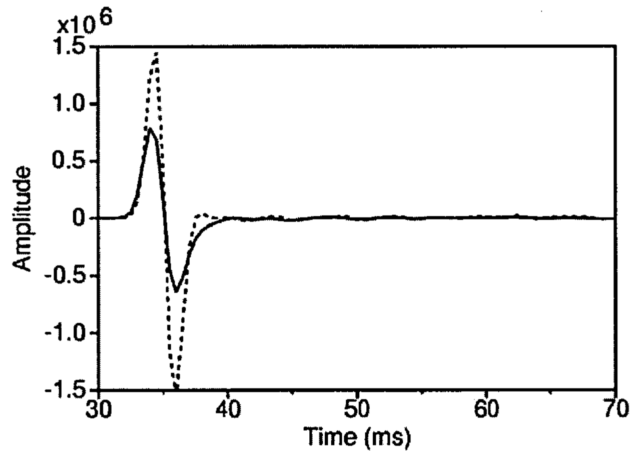

(a)

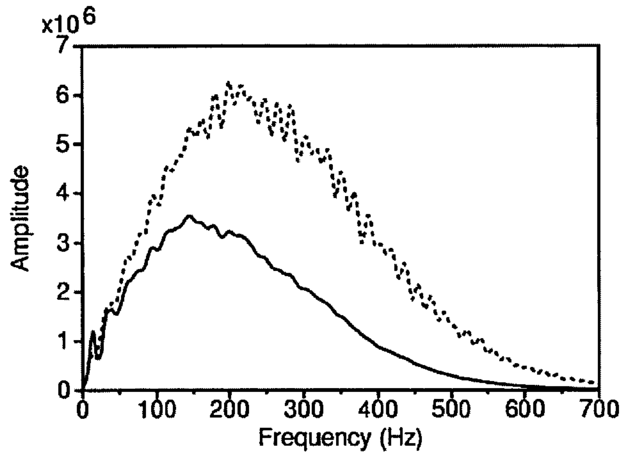

(b)

Figure 5.3 (a) Comparison of two traces without attenuation effect (dotted line), and considering attenuation effect (solid line), from the receiver at position (55, 215m). (b) Comparison of the amplitude spectra of two traces without attenuation effect (dotted line) and considering the attenuation effect (solid line).

Figure 5.1a shows the synthetic velocity model with values ranging from 2000 to 3500 m/s, and Figure 5.1b is the corresponding $1/Q$ attenuation factor with value ranging from 0.1 to 0. A line of sources is placed at $x = 5$ m, spreading in the z direction from 5 to 255 m, and a line of receivers is placed at $x = 55$ m, spreading in the z direction from 5 to 255m.

For the seismic simulation, I divide the region of 60×270 m^2 into finite-difference cells of 0.5×0.5 m^2. The source function is a first derivative of the Gauss function with a dominant frequency of 250 Hz.

Figure 5.2a shows one shot gather of the source at (5, 135m). Compared with the shot gather computed without the attenuation effect (Figure 5.2b), the amplitude of the result is much weaker. Figure 5.3 shows a selected trace, at receiver position (55, 215m) from the two shot gathers in Figure 5.2. I can see that the attenuation has a strong effect on waveform, both on amplitude and on the domain frequency.

5.3 Waveform tomography for the attenuation

5.3.1 Two inversion strategies

For waveform tomography, I test two strategies: (1) I invert first for the real-part velocity model and then for the attenuation factor model, keeping real-part velocity fixed. (2) I invert the real-part velocity and the attenuation factor models simultaneously, i.e., for the complex-valued velocity field.

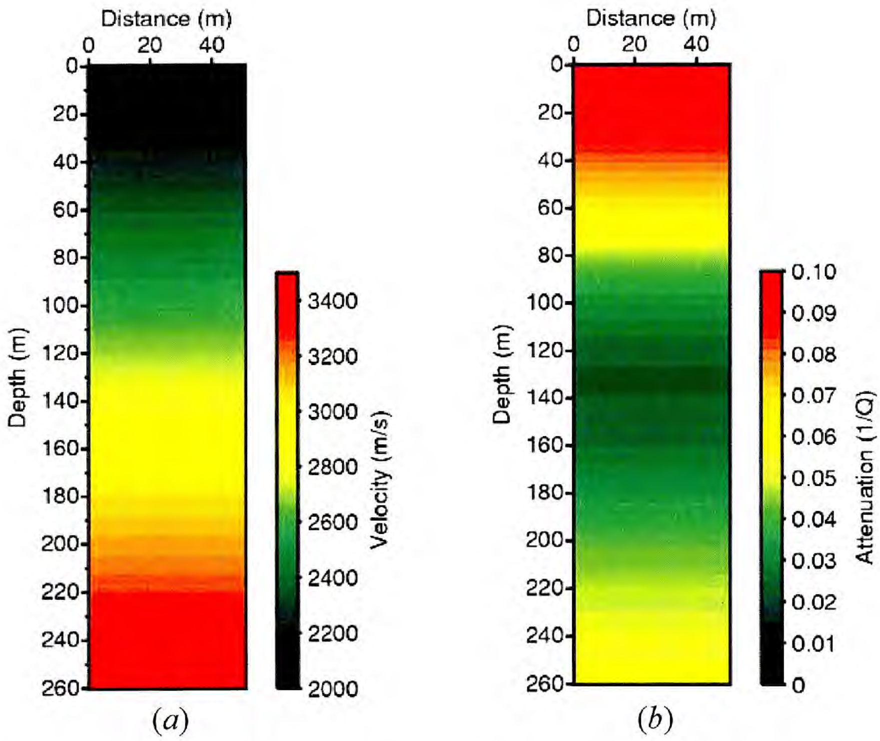

Figure 5.4 (a) The starting velocity model for waveform tomography. (b) The corresponding synthetic attenuation factor ($1/Q$) model obtained by smoothing the true attenuation factor model shown in figure 5.1b.

Test 1: This test has two steps. In the first step, I invert for the velocity model only, using starting real-part velocity model shown in Figure 5.4a, and starting attenuation factor model shown in Figure 5.4b. Figure 5.5a is the reconstructed velocity model after performing waveform inversion using selected frequency components between 100 to 1000Hz.

In the second step, I fix the real-part velocity model to that shown in Figure 5.5a and, with the same starting attenuation factor model as the first step, invert for the attenuation factor model only. Figure 5.5b is the reconstructed attenuation factor model.

Test 2: I invert the real-part velocity model and attenuation factor model simultaneously in every iteration step of the waveform inversion. Figure 5.6a is the reconstructed real-part velocity model. Figure 5.6b is the reconstructed attenuation factor model.

Comparing the results of these two tests on synthetic data without noise, there are no big differences between these two methods. Most of the layer structure in the real-part velocity model can be recovered, both in quantitative and in qualitative information. In the reconstructed attenuation factor models, the layer structure can be recovered at depth 80-180m, and the result of test 1 is slightly sharper than that of test 2. Both recovered models them show some blurred layer character from 40-80m, where the ray coverage is very low. Even in these depth ranges, however, the waveform inversion shows strong potential for attenuation factor inversion.

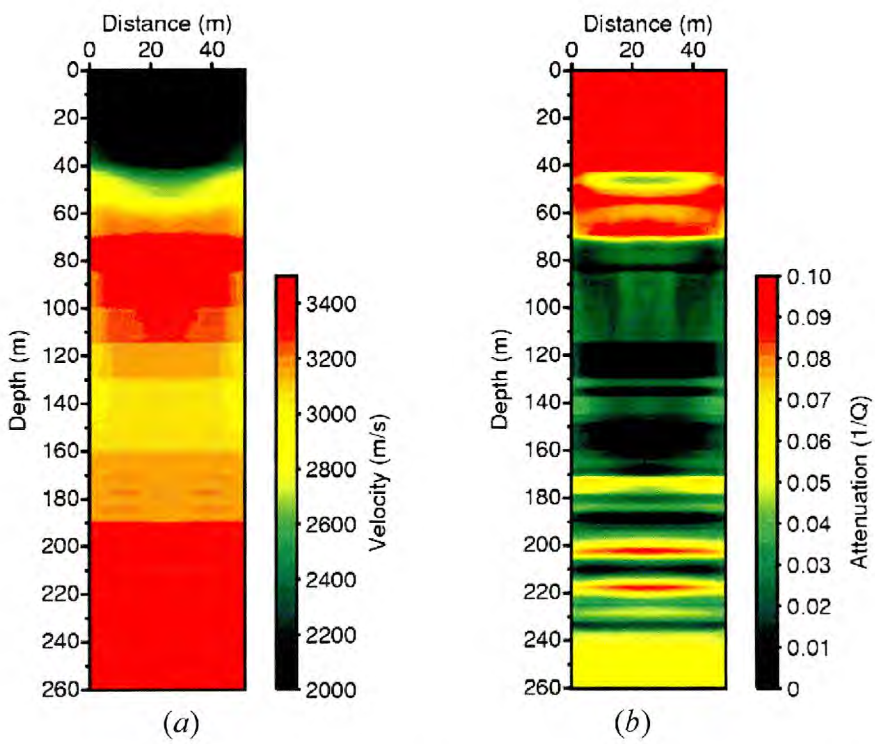

Figure 5.5 Results of Test 1: inverted real-part velocity and attenuation factor model one by one. (a) Reconstructed real-part velocity model, using figure 5.2a as starting real-part velocity model and figure 5.2b as fixed attenuation factor model. (b) Reconstructed attenuation factor model, using figure 5.3a as fixed real-part velocity model and figure 5.2b as starting attenuation factor model.

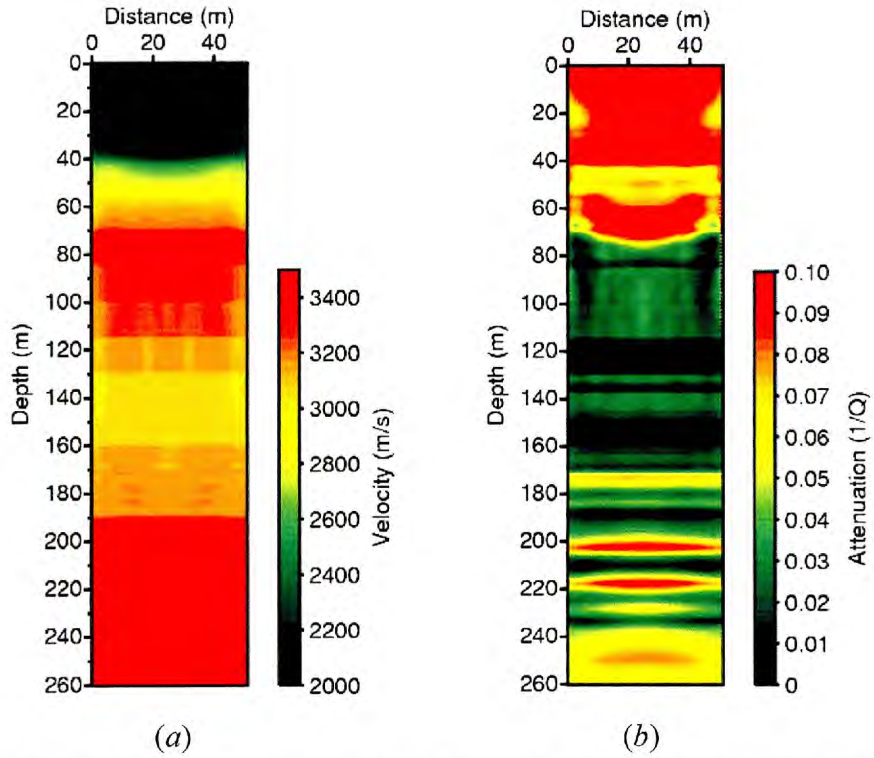

Figure 5.6 Results of Test 2: real-part velocity and attenuation factor models inverted simultaneously by waveform inversion. (a) Reconstructed real-part velocity model, and (b) reconstructed attenuation factor model, using starting real-part velocity model and attenuation factor models shown in Figure 5.2a, b.

5.3.2 The effect of the starting attenuation model

When I process real data, in general I will have no proper starting model of the attenuation factor for the inversion. However, the starting model chosen is a very important step for nonlinear inverse problem using waveform inversion. So I design the following tests to check the sensitivity of the inversion to the starting model.

First, I use a starting attenuation model with zero everywhere. Figure 5.7a is the reconstructed velocity model and Figure 5.7b is the reconstructed attenuation factor model.

The layer structure is recovered in both velocity and attenuation factor model. Especially at the 100-180m depth, even thin layers at 135m depth and 85m depth can be recovered in the reconstructed attenuation factor model.

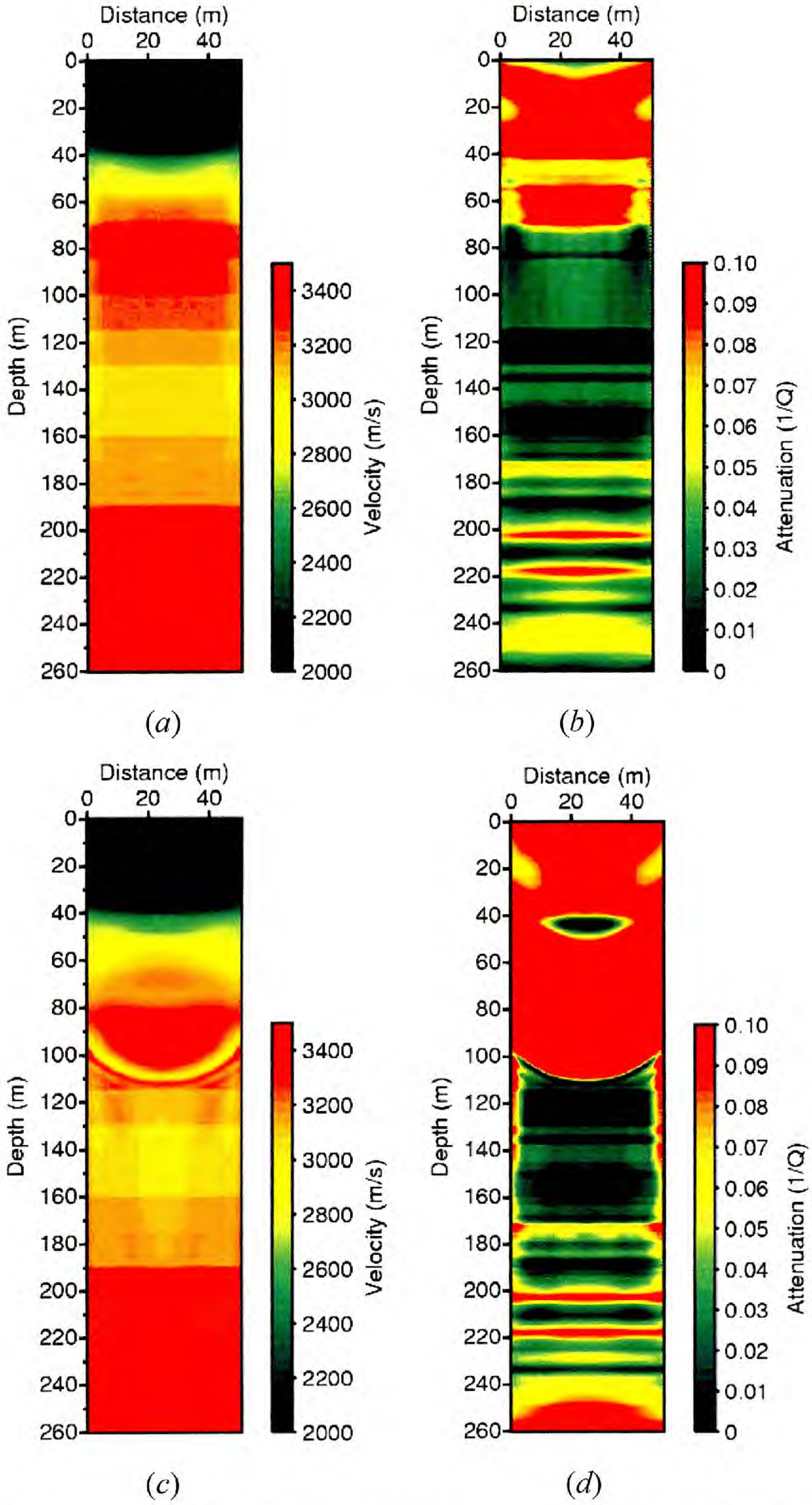

Figure 5.7 Starting attenuation factor model test: (a) Reconstructed real-part velocity model, using 0 everywhere in starting attenuation factor model. (b) Reconstructed attenuation factor model. (c) Reconstructed real-part velocity model, using 0.1 (max $1/Q$ value in the true model) everywhere in starting attenuation factor model. (d) Reconstructed attenuation factor model.

In the next test, I use a constant value of 0.1 across the whole model as the starting attenuation model. Figure 5.7c is the reconstructed velocity model and Figure 5.7d is the reconstructed attenuation model. Those two results are far away from the true model. Especially at the 40-110m depth, no characteristics of the true model have been recovered at all.

The poor result of Figure 5.7c,d is because $1/Q$=0.1 in the starting model is far away from the true model (with magnitude 0.01), and the initial model causes a big bias in the imaginary part of the velocity and strong nonlinearity in the inverse problem.

In practice, without a proper starting attenuation model, it is a better strategy to execute waveform inversion, with setting attenuation $1/Q$=0.

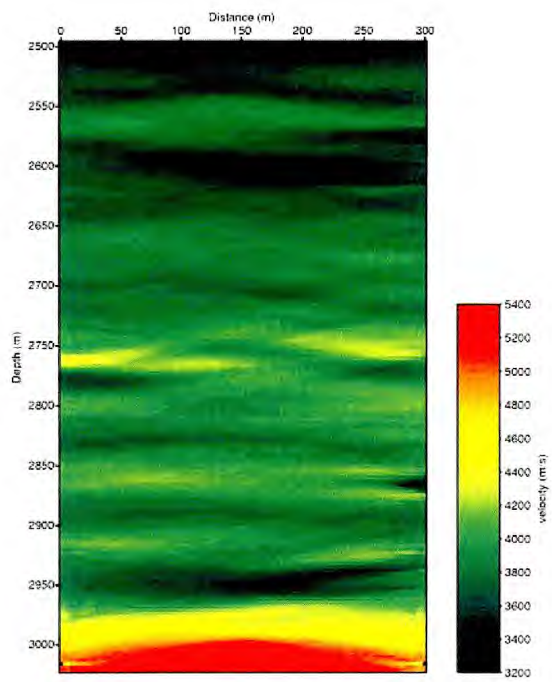

Figure 5.8 The initial velocity model for waveform inversion, generated by traveltime inversion from Figure 3.6a.

5.4 Real data attenuation inversion

For this test, I use the same data as I presented in the previous chapters. I make the velocity model discrete in cells of area 3m x 3m to satisfy the criterion of four cells per wavelength for the highest frequency (485 Hz) that I use in the inversion. The depth range that I choose to invert for is from 2497 to 3022 m. Therefore, there are altogether 100 rows and 175 columns in the grid.

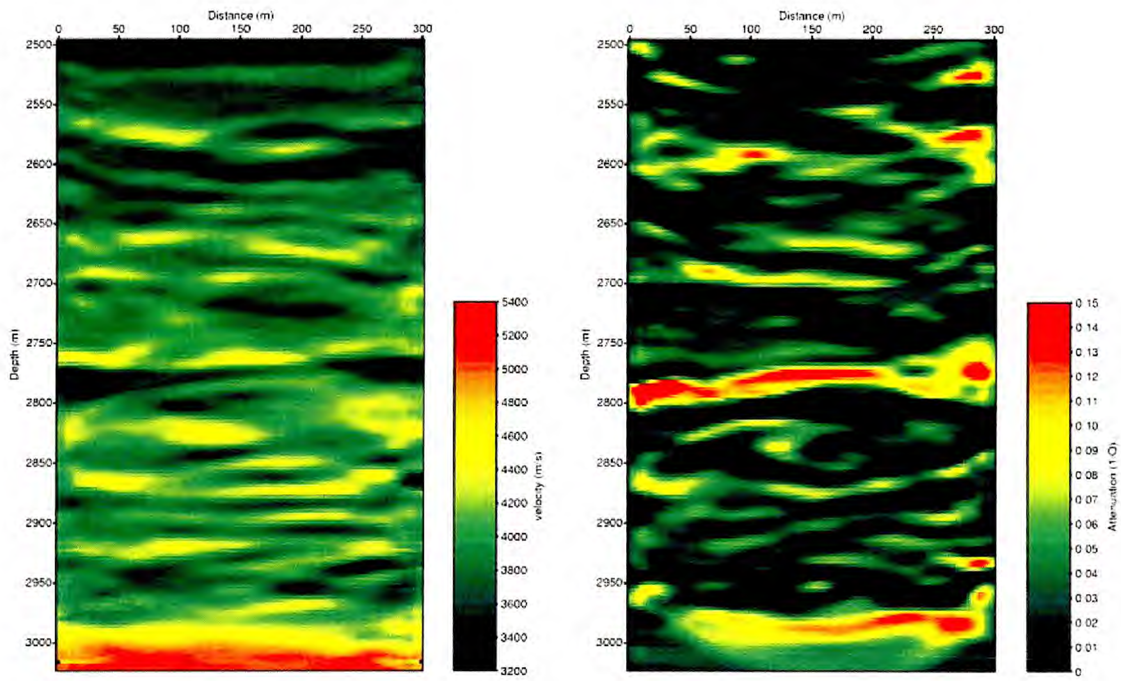

(*a*) (*b*)

Figure 5.9 Real data test 1: Inverse attenuation factor model first and fixing attenuation factor model. Then inverse attenuation factor model by fixing the velocity model. (a) Reconstructed velocity model. (b) Reconstructed attenuation factor model.

With the fixed 3×3 smoothing operator used in waveform tomography, I now design two experiments to further compare the above two methods with real data. Figure 5.8 displays the starting velocity model and the starting attenuation factor model is set to 0 everywhere. In the two experiments, I use groups of five neighboring frequencies simultaneously in the inversion (Pratt and Shipp, 1999). The 60 selected frequencies are assigned into 12 groups with increasing frequency contents from 190Hz to 485Hz. The result from each lower frequency group is used as the starting model for the inversion of the next higher frequency group. For each group, three iterations are carried out, proceeding through all groups. For every iteration, the gradient of each frequency group is computed using all five frequencies simultaneously.

In experiment 1, figure 5.9a is the reconstructed real-part velocity model obtained using all 12 frequency groups consecutively with the attenuation factor model fixed to zero. Figure 5.9b is the reconstructed attenuation factor model obtained by fixing the real-part velocity model to that of Figure 5.9a.

In experiment 2, figure 5.10a is the reconstructed real-part velocity model and Figure 5.10b is the reconstructed attenuation factor model obtained by inverting for both models in the same step.

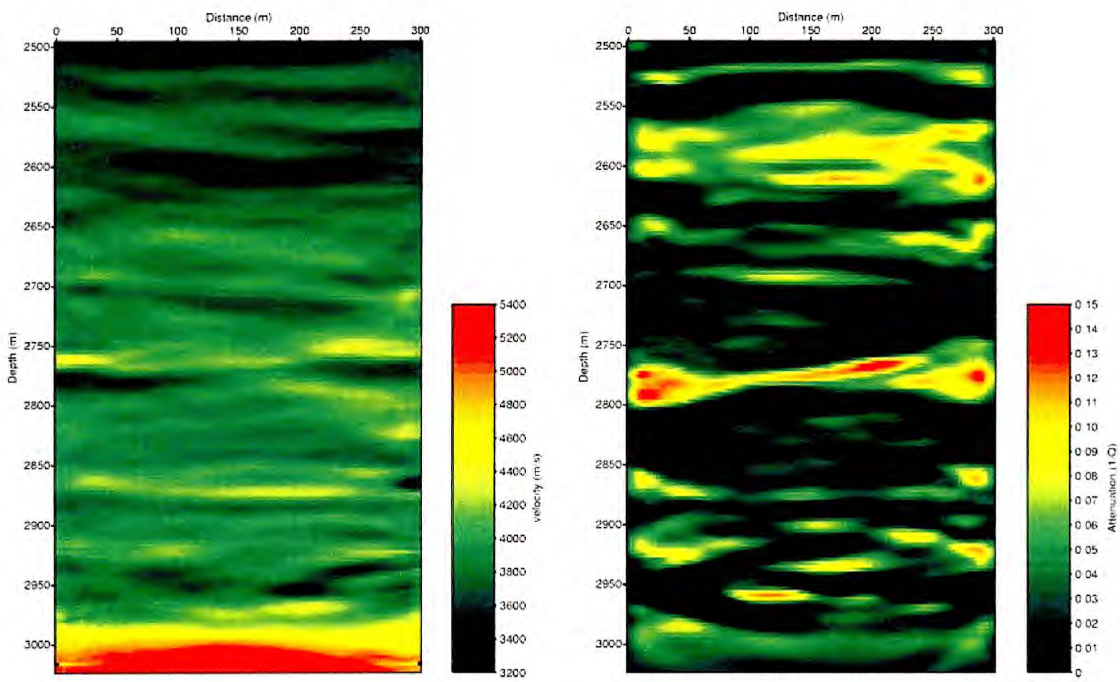

(a) (b)

Figure 5.10 Real data test 2: Inverse attenuation factor model and the velocity model together in the same step, using same starting velocity model as real data test 1. (a) Reconstructed velocity model. (b) Reconstructed attenuation factor model.

Comparing the results of those two experiments, there are big differences in both the real-part velocity models and the attenuation factor models. The reconstructed real-part velocity in experiment 2 has generally lesser velocity contrasts than that of experiment 1. The velocity contrast in Figure 5.9a is bigger than in the Figure 5.10a, with values ranging from 3500m/s to 5500m/s. For example, at the 2600m depth, I can see two layer structures in Figure 5.9a clearly, but the same area is blurred in Figure 5.10a.

The reconstructed attenuation models, shown in Figure 5.9b and 5.10b, have contrasting structures. Compared with real-part velocity model, the low real-part velocity is corresponding to having higher attenuation than the fast one. At depth 2750-2850m, both figures show two strips of low attenuation. These low attenuation zones correspond to the two high velocity layers respectively. But at depth 2550-2650m and 2800-2850m, these two figures are quite different. The inversion for $1/Q$ is sensitive to the effects of noise in the real dataset. If I invert the real-part velocity and $1/Q$ together, there is certainly a trade-off between them, because the real-part velocity is about 10^3, but $1/Q$ is just 10^{-2}. In the objective function, their contribution will be different. Small velocity perturbations will bring big $1/Q$ perturbations. If I invert the two models simultaneously without any trade-off compensation, the attenuation factor model may be biased far from the true model. If I fix the attenuation factor model to invert the real-part velocity model first, then fix real-part velocity model to invert the attenuation factor model as in experiment 1, I can avoid the trade-off between errors in the real-part velocity and those in the attenuation factor. So I prefer the results of experiment 1 in Figure 5.9 as final results.

5.5 Conclusions

(1) The examples have demonstrated that variation of the attenuation factor affects both the amplitude and the frequency of the modelled seismic wavefield.

(2) The real-part velocity is of order 10^3, and the attenuation factor ($1/Q$) is of order 10^{-2}. Relative contributions of these two terms to the objective function are different. When dealing with real data, the best strategy is to first invert the real-part

velocity model with the attenuation factor model fixed, then fix real-part velocity and invert for the attenuation factor model. Using this way we avoid the trade-off of errors between the two fields.

(3) Because the attenuation factor is very sensitive to the starting model, using constant value 0 in the starting attenuation factor model is the safe choice for waveform inversion, when we have no other starting attenuation factor model.

Chapter 6

Seismic response to fractured media with different scales and different orientations

6.1 Introduction

In this chapter, I systematically investigate the effects of fracture scale and fracture orientation on the seismic response. When fractures are smaller than the wavelength, they act as single scatters and generate secondary wavefields. When the size approaches the wavelength they act as individual interfaces and the wavefield is more complicated. Different fracture orientations also have significantly different effects on the seismic wavefield, and vertical fractures show the strongest effect on wave propagation. I further measure these effects on waveform tomography, using an attenuation model to represent fractures with different scales and different orientations.

Fractures are a very important element in reservoir characterization and in reservoir exploration and development, especially as they can act as gas and fluid pathways. In this chapter, I systematically investigate the effects of factures with different scales and orientations on seismic response.

In the forward wavefield simulation, I implement fractures on finite-difference grids using an effective medium theory (Coates and Schoenberg, 1995; Liu *et al.,* 2000). This method can deal with multiple scattering cases without having any limitations on the number of fractures included in the medium.

I then use waveform tomography to invert for the attenuation factor ($1/Q$), due to the fractures. Waveform tomography is implemented in the frequency domain, so it is easy to take the frequency-dependent attenuation into consideration (Song *et al.,* 1995; Pratt *et al.*, 2004). A reconstructed attenuation model quantitatively represents the effect of fractures on seismic energy.

6.2 Implementation of fractures in the finite-difference scheme

In this study, I use the fourth-order finite-difference method (Levander, 1988), as shown in appendex A, to model the seismic wavefield, in order to study the effect of different attributes of fractures on the wavefield characteristics. Levander's (1988) finite-difference method, using a staggered-grid, is accurate to second-order in time and fourth-order in space. Its advantages include that it is stable for all values of Poisson's ratio and it reduces the spatial sampling required to accurately simulate wave propagation, compared with a traditional finite-difference method.

Schoenberg (1980) represented fractures as boundaries with characteristics of discontinuous displacement and continuous stress. This can be expressed as a boundary condition:

$$[u] = \mathbf{Z}\boldsymbol{\tau}, \tag{6.1}$$

where $[u]$ is the average displacement discontinuity, $\boldsymbol{\tau}$ is the traction acting across the fracture, and $\mathbf{Z}$ is the fracture compliance tensor, which is an elastic parameter of the medium. To realize it in a finite-difference method, I can set the elastic parameter using the equivalent anisotropic medium within the cells surrounding the fracture (Coates and Schoenberg, 1995). This method can represent any sizes of fracture, provided the grid size is smaller than the fracture length (Vlastos *et al.,* 2003).

In this Chapter, I follow Liu et al. (2000) method for estimating the equivalent medium representation of a fractured medium. The advantage of the method is that all parameters involved have physical meaning. A compliance tensor is the inverse of the stiffness tensor $c_{k\ell}$ which can be expressed as

$$c_{k\ell} = \begin{bmatrix} c_{11} & c_{12} & c_{13} & 0 & 0 & 0 \\ c_{21} & c_{22} & c_{23} & 0 & 0 & 0 \\ c_{31} & c_{32} & c_{33} & 0 & 0 & 0 \\ 0 & 0 & 0 & c_{44} & 0 & 0 \\ 0 & 0 & 0 & 0 & c_{55} & 0 \\ 0 & 0 & 0 & 0 & 0 & c_{66} \end{bmatrix}. \tag{6.2}$$

In the area surrounding the fractures, the compliance tensor includes two parts. One is the compliance tensor in the absence of any fractures. And anther is the extra compliance tensor resulting from the fractures. The elastic constants in the stiffness tensor can be expressed as

$$
\begin{aligned}
c_{11} &= (\lambda + 2\mu)\left(1 + \frac{\lambda + 2\mu}{\mu}\varepsilon U_{33}\right)^{-1}, \\
c_{22} &= c_{33} = \left[(\lambda + 2\mu) + 4(\lambda + \mu)\varepsilon U_{33}\right]\left(1 + \frac{\lambda + 2\mu}{\mu}\varepsilon U_{33}\right)^{-1}, \\
c_{12} &= c_{13} = c_{21} = c_{31} = \lambda\left(1 + \frac{\lambda + 2\mu}{\mu}\varepsilon U_{33}\right)^{-1}, \\
c_{23} &= c_{32} = \lambda(1 + 2\varepsilon U_{33})\left(1 + \frac{\lambda + 2\mu}{\mu}\varepsilon U_{33}\right)^{-1}, \\
c_{44} &= (c_{22} - c_{23})/2 = \mu, \\
c_{55} &= c_{66} = \mu(1 + \varepsilon U_{11})^{-1}.
\end{aligned}
\tag{6.3}
$$

where λ and μ are referred to as the Lamé coefficients, and ε is the crack density. For dry cracks, Hudson (1981) gives

$$
U_{11} = \frac{16}{3}\frac{\lambda + 2\mu}{3\lambda + 4\mu}, \text{ and } U_{33} = \frac{4}{3}\frac{\lambda + 2\mu}{\lambda + \mu}. \tag{6.4}
$$

These elastic constants represent a cluster of cracks in the compact area.

There is no displacement outside of the two fracture tip points. To represent this fracture characteristic, Kachanov (1993) introduced a hyperbolic taper equation for the crack-opening displacement. Thus, the compliance constant, used to exhibit fractures in the grid cells, should be tapered along the fracture. After the tapering is implemented, the value of the compliance constant of fracture in the centre of fracture is the maximum value, and the value at the fracture tips is zero.

Kachanov's (1993) weighting equation for fracture is

$$
Z = Z_{\max}\sqrt{1 - \left(\frac{x}{\ell}\right)^2}, \tag{6.5}
$$

where $Z_{\max}$ is the maximum value of the weighting function in the middle of the fracture, ℓ is half the length of fracture, and x is the length between the fracture centre and a point on the fracture.

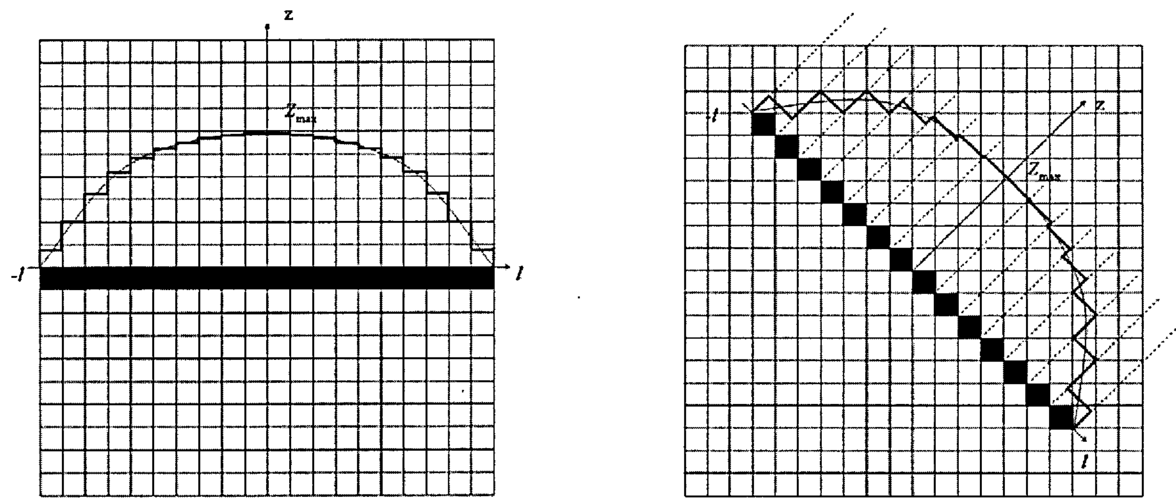

(*a*) (*b*)

Figure 6.1 Following Kachanov (1993), the fractures are realistically simulated by gradually reducing the elastic constant from the middle to the two fracture tips. At two tips of the fractures, the displacement equal to 0. (a) Horizontal fracture. (b) 45° fracture. The grid represents the cells parameterisation in the velocity model. The cells marked by black are the cells surrounding the fractures. The curve represents the weighting function and the stepped line is the value assigned to the cells surrounding the fracture.

The curve in Figure 6.1a represents the weighting function and the stepped line is the value assigned to the cells surrounding the horizontal fracture. The stepped line in Figure 6.1b is the value assigned to the cells surrounding the 45° fracture. For example, the elastic constant c_{11} can be represented as

$$c_{11} = (\lambda + 2\mu)\left(1 + Z\frac{\lambda + 2\mu}{\mu}\varepsilon U_{33}\right)^{-1}, \tag{6.6}$$

where the $\frac{\lambda + 2\mu}{\mu}\varepsilon U_{33}$ term in equation 6.6 represents the effect of the fracture, and Z is a weighting factor so that the elastic constants can realistically represent the fractures, including two fracture tips.

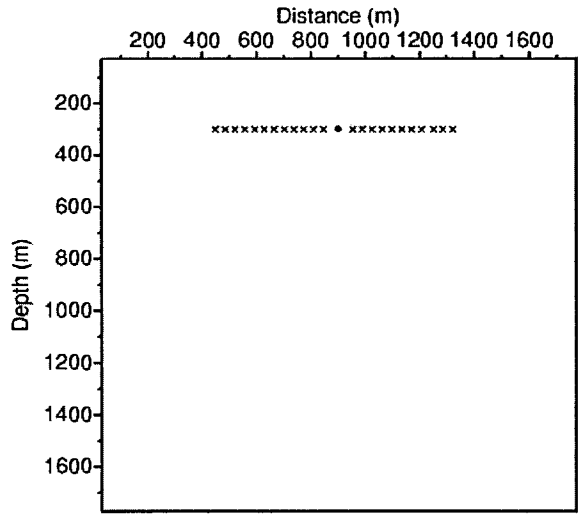

Figure 6.2 Source and receiver geometry. Cross points mark the position of the receiver string and the dot point marks the position of source in the middle.

6.3 The effect of fracture scales and orientations

In this section, I simulate the seismic wavefield in fractured media, and observe the effect of fracture scale and orientation. The model I used has 1770 fractures randomly distributed in an 1800×1800 m^2 area, with a spatial grid step of 3 m. I set the top boundary using a free surface boundary condition, and the other three boundaries using an absorbing boundary condition. The surrounding solid matrix has *P*- and *S*-wave velocities V_P=3000 m/s, V_S=1500 m/s and density ρ=2200 kg/m^3. The source type is a pressure force. A Ricker wavelet with a dominant frequency of 40 Hz is used. The source is placed at horizontal distance of 900m and a depth of 300m. A line of receivers is placed at the same level, spreading from 450m to 1350m, with maximum offset 450m, as shown in Figure 6.2. A time step of 0.5 ms is used for the seismic simulation.

Figures 6.3-6.6 show fracture distribution with different fracture sizes and a common alignment which is either horizontal or vertical. The fracture size in figure 6.3 is $\alpha = 0.4\lambda$, where λ is the wavelength (30 m). The fracture size in figure 6.4 is the same as the wavelength, ($\alpha = \lambda$). The fracture size in figures 6.5 and 6.6 is $\alpha = 1.5\lambda$ and $\alpha = 2\lambda$, respectively. I generate synthetic shot gathers using the method of appendix A to help us interpret and understand the seismic response. (c) and (d) in Figures 6.3-6.6 are the seismic responses of the vertical components of the fractured distributions shown in (a) and (b).

By comparing these shot gathers, one can observe that the size of the fracture has a strong effect on the seismic response.

Figure 6.3 shows that more scattering occurs if shorter fracture wavelengths are used. Present with longer fracture wavelengths, as shown in Figures 6.4, 6.5, and 6.6 the fractures change the apparent properties of the whole material. The long fractures act as individual boundaries. So the interference between the various reflections has strong effects on the amplitudes of reflected waves. Because the longer fractures cluster in some areas, the seismic response could be interpreted as a reflection from a single reflector. Strong and horizontally coherent energies are shown in Figures 6.4-6.6.

In Figures 6.3-6.6, I show the fracture models with different fracture orientations. From these tests, I can observe that the seismic response depends on the orientation of the fractures. Because the fractures act as strong diffraction points, the dipping coherent energies in shot gathers (figure 6.3d), with fractures in the vertical direction, are much stronger than those in shot gathers with the same size of fractures in other non-vertical directions (figure 6.3c). All examples show that the fracture orientation has the most significant effect on the seismic responses. This observation could be the basis of a method to detect coherent fracture orientation in practice. Furthermore, the wavefields generated in Figure 6.5d, and 6.6d show strong coda waves and are very complicated.

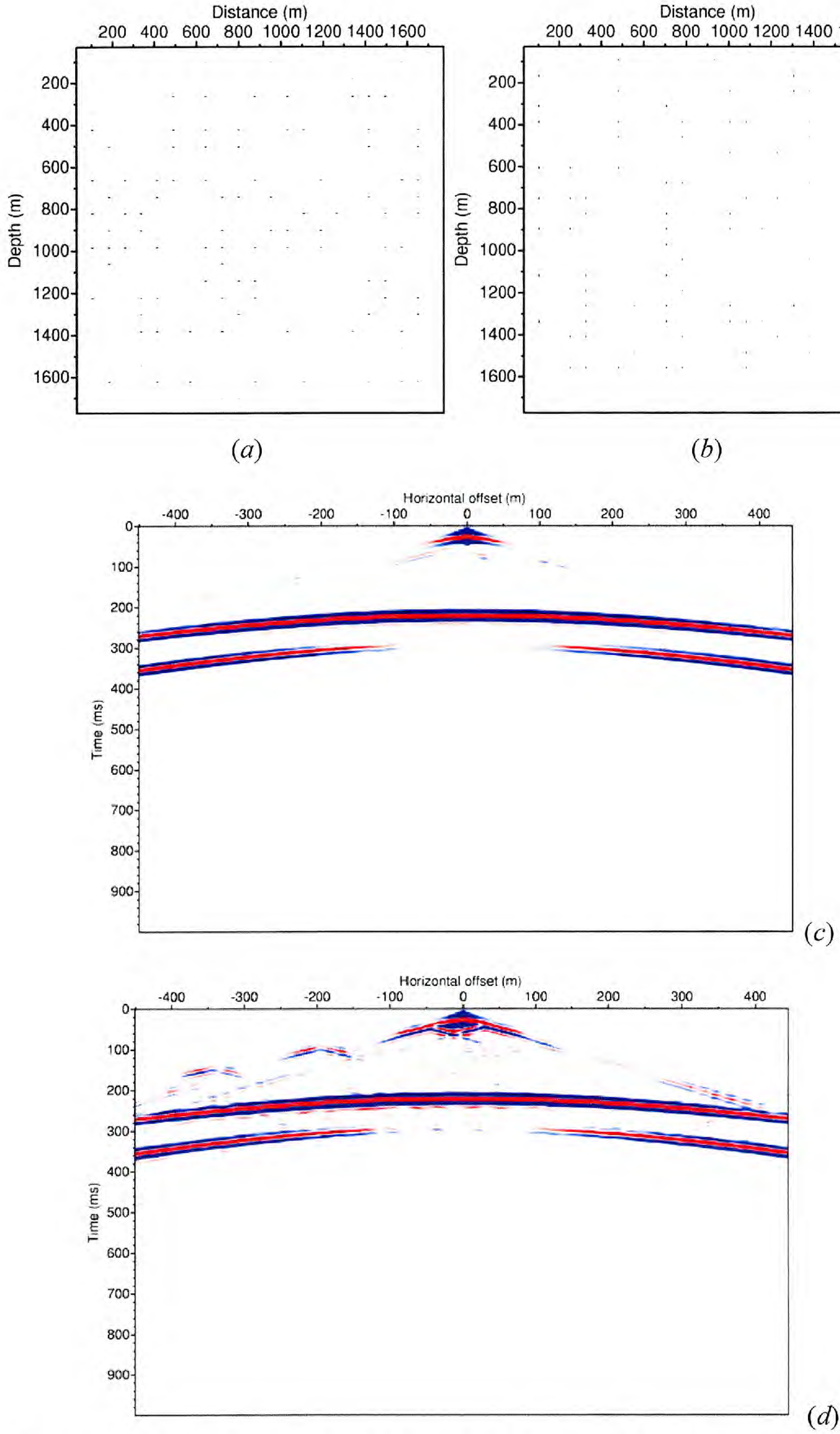

Figure 6.3 (a) Horizontal fracture model with fracture size $\alpha = 0.4\lambda$. (b) Vertical fracture model with the same fracture size. (c) The vertical component of the seismic response of model a. (d) The vertical component of the seismic response of model b.

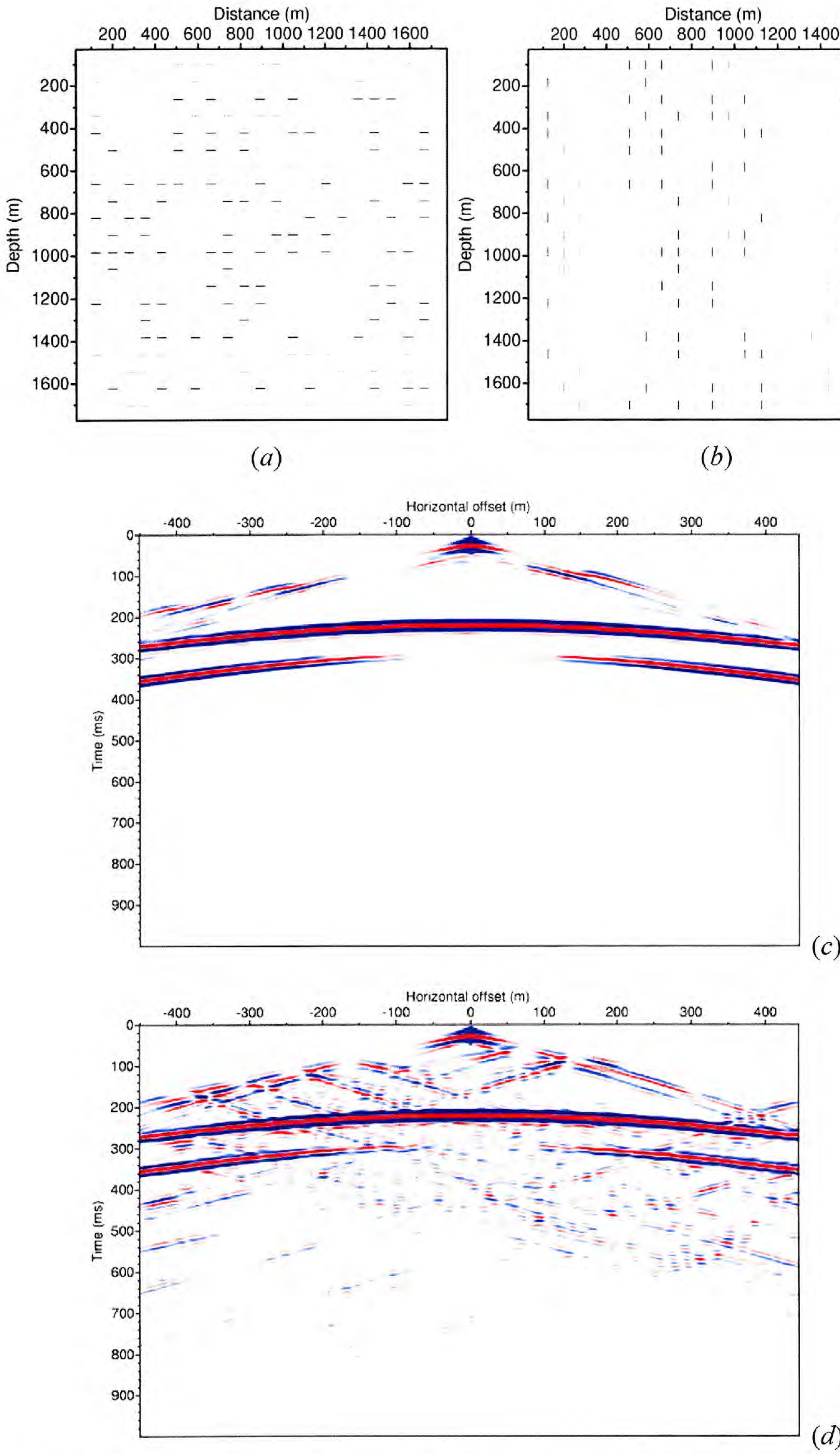

Figure 6.4 (a) Horizontal fracture model with fracture size $\alpha = \lambda$. (b) Vertical fracture model with the same fracture size. (c) The vertical component of the seismic response of model a. (d) The vertical component of the seismic response of model b.

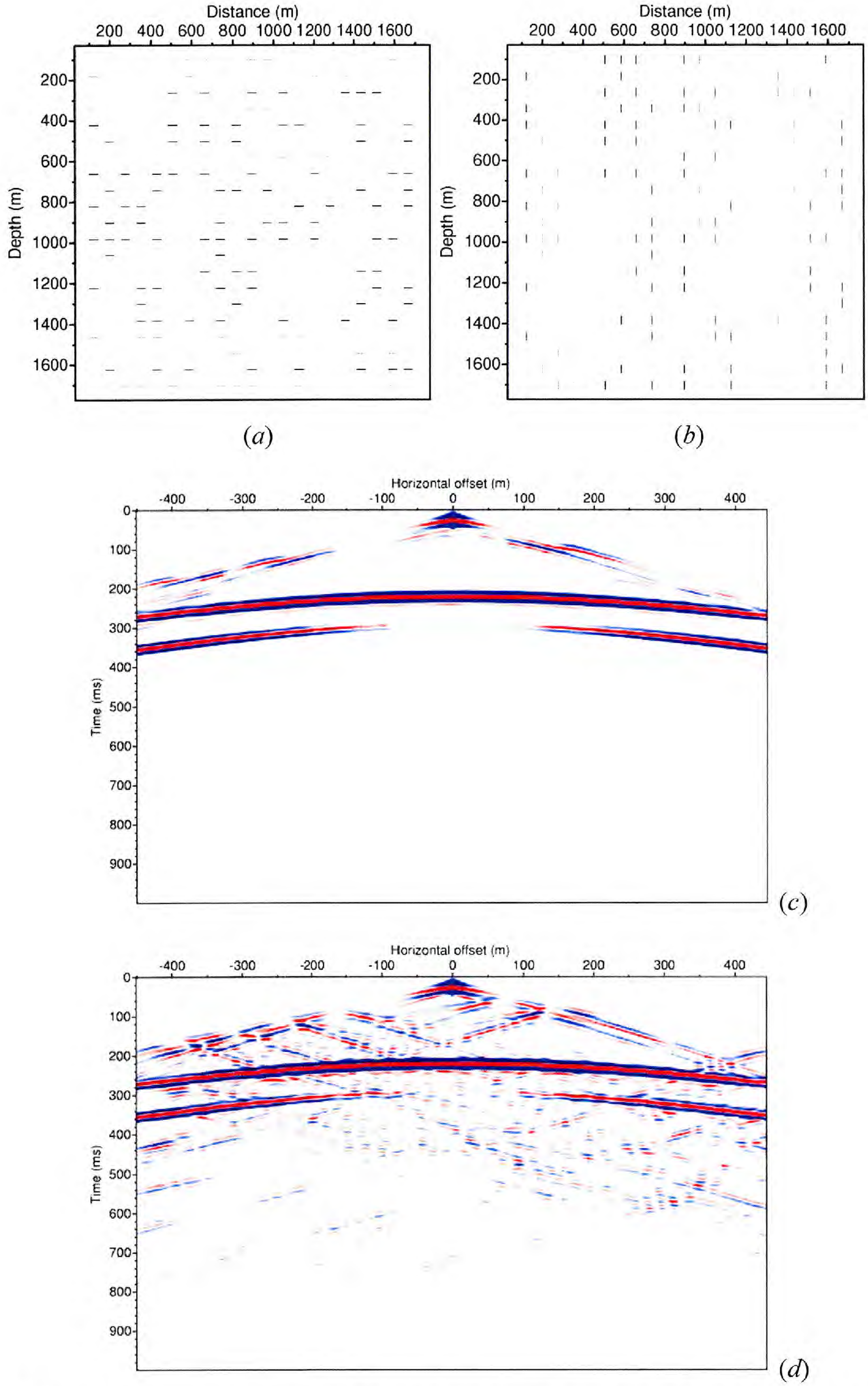

Figure 6.5 (a) Horizontal fracture model with fracture size $\alpha = 1.5\lambda$. (b) Vertical fracture model with the same fracture size. (c) The vertical component of the seismic response of model a. (d) The vertical component of the seismic response of model b.

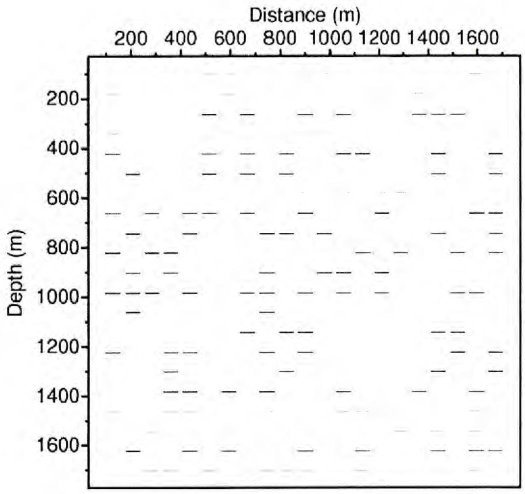

(a)

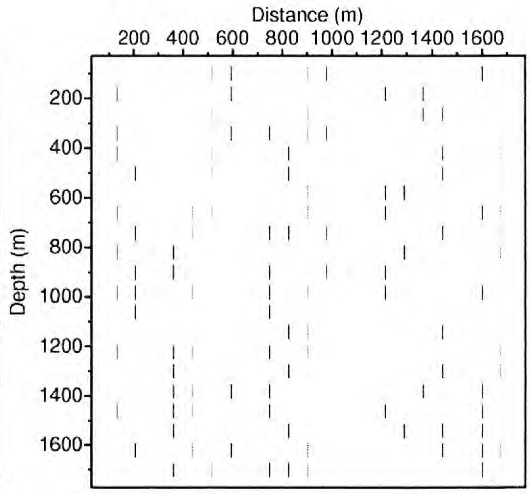

(b)

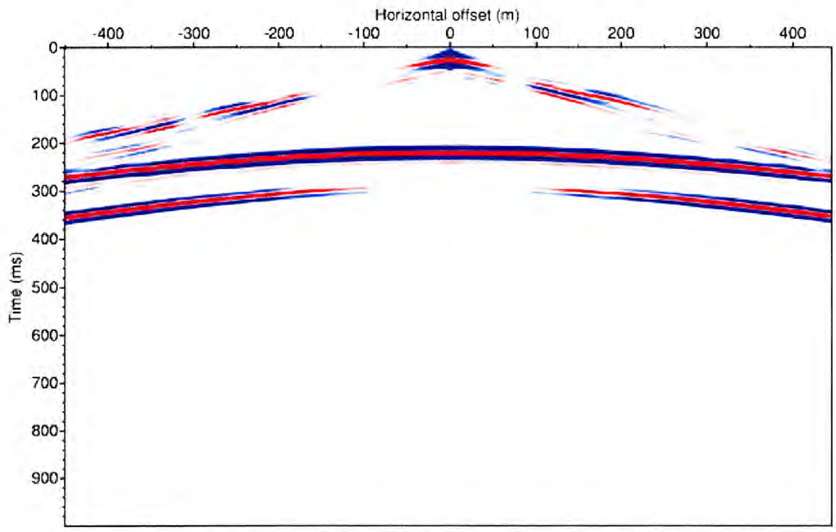

(c)

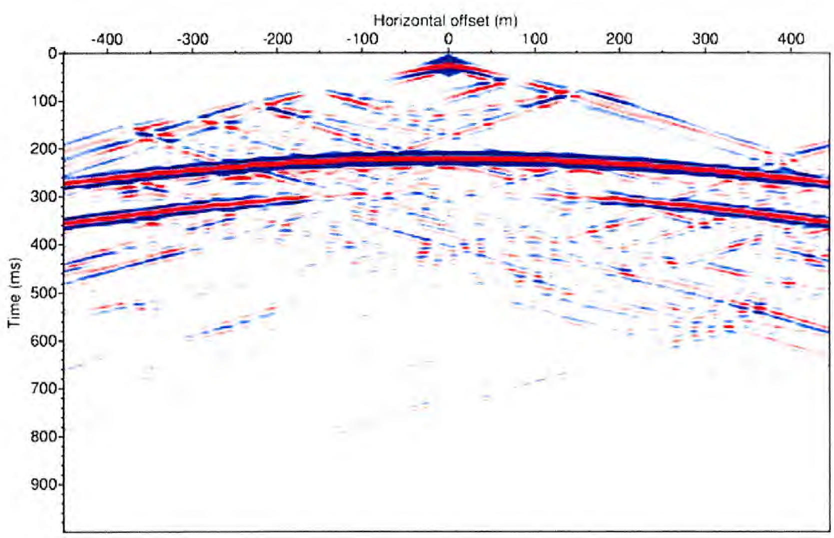

(d)

Figure 6.6 (a) Horizontal fracture model with fracture size $\alpha = 2.0\lambda$. (b) Vertical fracture model with the same fracture size. (c) The vertical component of the seismic response of model a. (d) The vertical component of the seismic response of model b.

6.4 The attenuation images of fractured media

At this stage I just have waveform inversion code based on acoustic wave equation. Therefore, I use elastic wave equation to modelling wavefield in the area with fractures. Then I should convert two components and source field in elastic wave equation to suit for acoustic wave equation.

In the acoustic assumption, $c_{11} = c_{33} = c_{13} = \lambda$ and $c_{55} = c_{15} = c_{35} = 0$. Here I use a stress source $S(t)$ for forward modelling. Then the elastic wave equation can be written as

$$
\begin{aligned}
-\rho\frac{\partial v_x}{\partial t} + \frac{\partial \tau_{xx}}{\partial x} + \frac{\partial \tau_{xz}}{\partial z} &= 0, \\
-\rho\frac{\partial v_z}{\partial t} + \frac{\partial \tau_{xz}}{\partial x} + \frac{\partial \tau_{zz}}{\partial z} &= 0, \\
-\frac{\partial \tau_{xx}}{\partial t} + \lambda\left(\frac{\partial v_x}{\partial x} + \frac{\partial v_z}{\partial z}\right) &= S(t), \\
-\frac{\partial \tau_{zz}}{\partial t} + \lambda\left(\frac{\partial v_x}{\partial x} + \frac{\partial v_z}{\partial z}\right) &= S(t), \\
\frac{\partial \tau_{xz}}{\partial t} &= 0.
\end{aligned}
\tag{6.7}
$$

where (v_x, v_z) is the particle velocity vector. According to Newton's second law, the relationship between particle velocity and pressure is

$$
\begin{aligned}
\rho\frac{\partial v_x}{\partial t} &= -\frac{\partial P}{\partial x} \\
\rho\frac{\partial v_z}{\partial t} &= -\frac{\partial P}{\partial z}
\end{aligned}
\; . \tag{6.8}
$$

Combining equations 6.7 and 6.8, I get

$$
\frac{\partial P}{\partial t} + \lambda\left(\frac{\partial v_x}{\partial x} + \frac{\partial v_z}{\partial z}\right) = S(t) . \tag{6.9}
$$

Then I combine equations 6.7 and 6.9 to get acoustic wave equation

$$
-\frac{\partial^2 P}{\partial t^2} + \frac{\lambda}{\rho}\left(\frac{\partial}{\partial x}\frac{\partial P}{\partial x} + \frac{\partial}{\partial z}\frac{\partial P}{\partial z}\right) = \frac{\partial S(t)}{\partial t} . \tag{6.10}
$$

To convert the two components v_x and v_z obtained from the elastic wave equation to pressure P, I first calculate partial derivatives of v_x and v_z, and use equation (6.8) to obtain pressure projection $P_x = \frac{\partial P}{\partial x}$ and $P_z = \frac{\partial P}{\partial z}$ in x and z directions respectively. I then calculate the incident angles θ by ray tracing, and obtain the scale measurement of pressure P by $P = P_x \cos(\theta) + P_z \sin(\theta)$. Meanwhile, the partial derivative of $S(t)$ with respect to time (Figure 6.7) is the source signature we need for the acoustic wave equation (6.10).

For wave propagation simulation, the solution domain is between two parallel boreholes 300 meters apart and 540 meters deep. The background P-wave velocity is 3000 m/s and S-wave velocity is 1700 m/s. Density ρ=2300 kg/m^3. The model has 36 fractures randomly distributed in depth from 180-300 m depth area. The model is discretized in cells with cell size 3m to satisfy the resolution criterion of both elastic wave equation forward modelling and acoustic wave equation waveform tomography. Therefore, there are altogether 100 rows and 175 columns in the grid. A line of sources is placed at (0, 0) m, spreading in the z direction from 0 to 522 m, and a line of receivers is placed at (300, 0) m, spreading in the z direction from 0 to 522m. The source type is a stress source, on τ_{xx} and τ_{zz}. A Ricker wavelet, shown in Figure 6.7a, with a dominant frequency of 100 Hz is used.

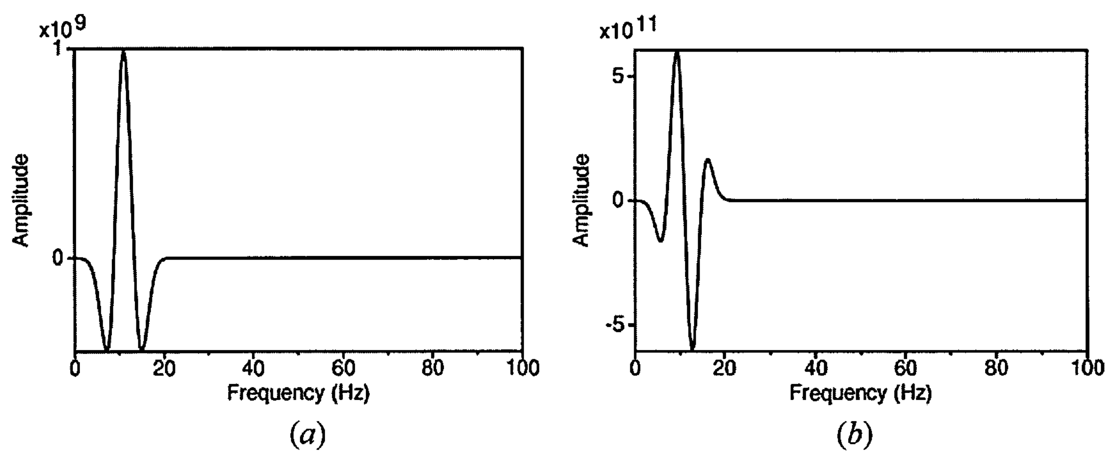

Figure 6.7 (a) First order Gauss function source wavelet $S(t)$ for forward modelling. (b) Equivalent source wavelet $\frac{\partial S(t)}{\partial t}$ for waveform tomography.

Using elastic wave equation forward modelling, I have two particle velocity components. Figure 6.8a is one shot gather of horizontal particle velocity and Figure 6.8b is the corresponding shot gather of the vertical particle velocity component. Figure 6.8c is the shot gather of the pressure, calculated from v_x and v_z using the method I mentioned at the beginning of this section. Figure 6.9a shows the fracture model with fracture size equal to 3m. Figure 6.7b is the source for waveform tomography obtained by differentiating the source signal, I used for forward modelling, in time.

Having equivalent source field and wavefield, I use the acoustic waveform tomography method to invert for the apparent attenuation factor (1/Q) model. Figure 6.9b is the corresponding reconstructed 1/Q model. A concentration of fractures near the offset 100-150 m and the depth 175-200m enhance each other and result in an apparently greater local attenuation (Figure 6.9b). Even the isolated fracture at the offset 285 m and depth 200 m causes apparent attenuation in the reconstructed model. Because the length of the fractures much smaller than the wavelength scattering of the energy by character these small fractures produces an apparent attenuation character corresponding to small elliptical regions of higher attenuation.

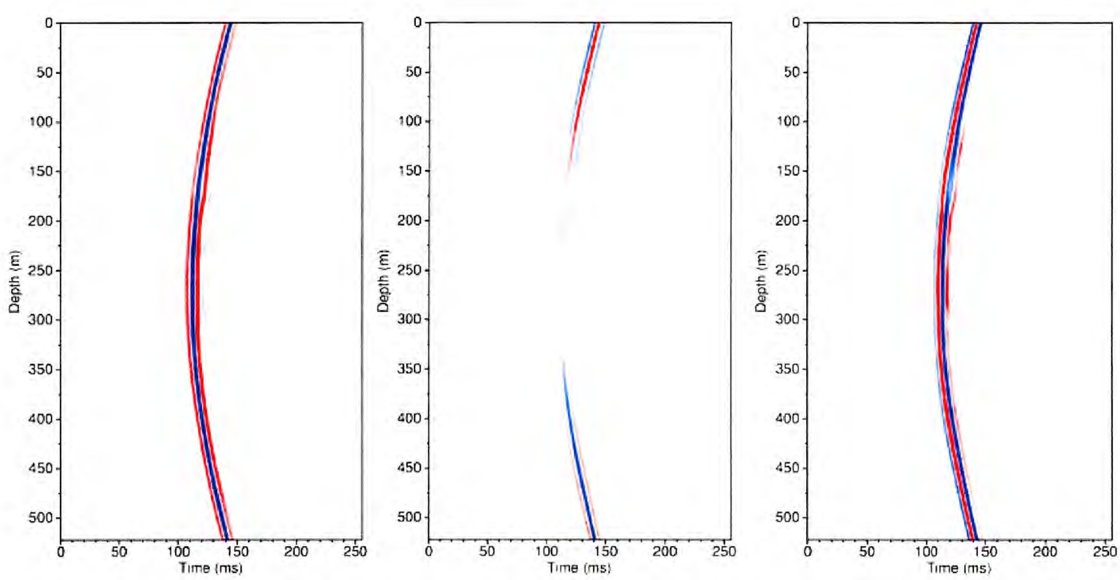

(a) (b) (c)

Figure 6.8 (a) Horizontal component of a shot gather. (b) The vertical component of a shot gather. (c) The shot gather of the pressure wavefield, obtained from the two particle velocity components.

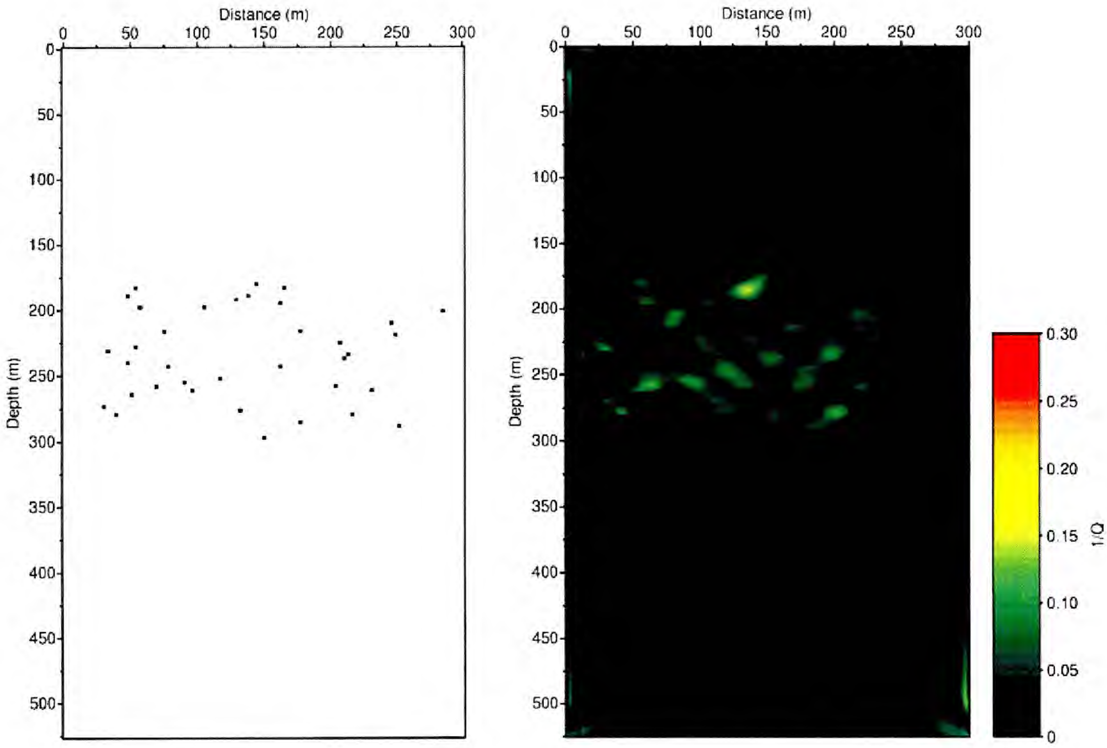

(*a*) (*b*)

Figure 6.9 (a) Fracture model with fractures of length 3 m. (b) The attenuation model reconstructed by acoustic waveform tomography.

In Figure 6.10-6.12, I show the reconstructed attenuation models, corresponding to different fracture models with increasing fracture length. Because the 15m vertical fractures, in Figure 6.10a, act as strong diffraction points, the seismic response lead to a the reconstructed attenuation model (Figure 6.10b) that is similar to Figure 6.9b, with attenuation enhanced because of the greater fracture length. When the length of vertical fractures is to 30m, the maximum attenuation values enhanced, compared to the results obtained with 15m fractures.

In Figure 6.10-6.12, I also show the reconstructed attenuation models, corresponding to the different fracture orientation. Comparing the experiments with the same fracture length, the fractures parallel to the source string show significantly greater attenuation. Using transmitted energy in these crosshole examples, the fractures, parallel to the source string, behave like small reflection interfaces. Hence in Figure

6.11d, we see that the attenuation is enhanced and connected to form high attenuation zones between 150-300 m depth, corresponding to the fractured area. Compared with two other fracture orientations, such as 45° angle fracture in Figure 6.12b and 135° angle fracture in Figure 6.12d, the fractures parallel to the source string show the strongest attenuation in the results of waveform tomography.

6.5 Conclusions

(1) In forward modelling of the surface data example, the examples shown in Figure 6.3-6.6 have demonstrated that when fractures are smaller than the wavelength, they act as single scatters and generate secondary wavefields, whereas when the fracture length approaches the wavelength they act as individual interfaces and the wavefield is more complicated. The observation confirms the importance of fault length in modelling fractured rock.

(2) In forward modelling the surface data example, different fracture orientations show significantly different effects on seismic wavefield. Vertical fractures show the strongest effect. Therefore, the numerical modelling techniques presented here can be a useful tool in understanding the important role of fractures and their effects on wave propagation.

(3) In the crosshole waveform tomography example, the characters of attenuation produced by 3m fractures are approximately elliptical, as fracture length is smaller than wavelength. Strong attenuation positions closely correspond to the fracture locations. When the length of the fractures increases, the attenuation is enhanced.

(4) In the crosshole waveform tomography example, fractures, parallel to the source string, show strongest attenuation in the results of waveform tomography, because the fractures act as reflecting surfaces in the measured seismic response.

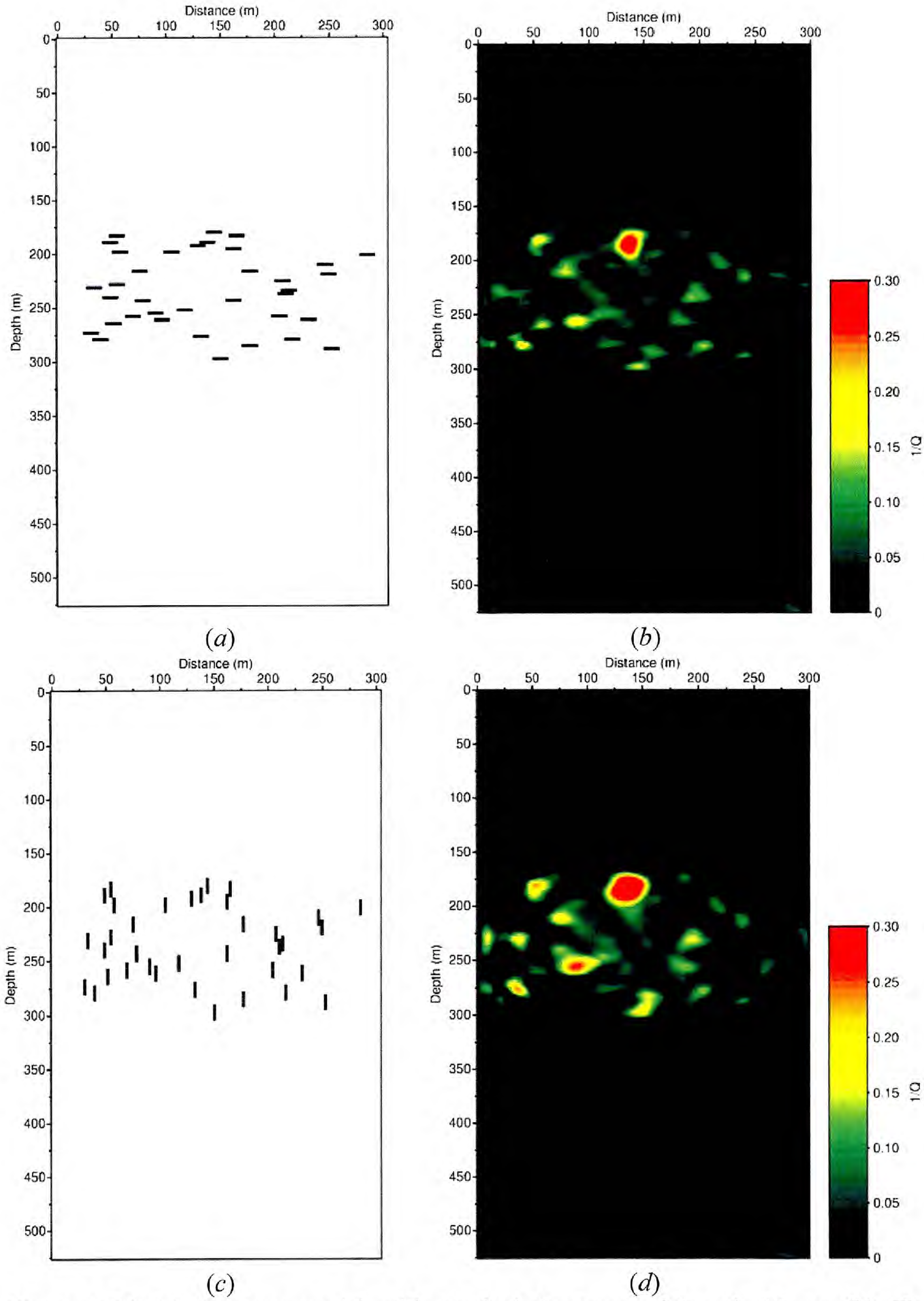

Figure 6.10 (a) Fracture model with vertical fractures of length 15 m. (b) The attenuation model reconstructed by acoustic waveform tomography. (c) Fracture model with horizontal fractures of length 15 m. (d) The attenuation model reconstructed by waveform tomography.

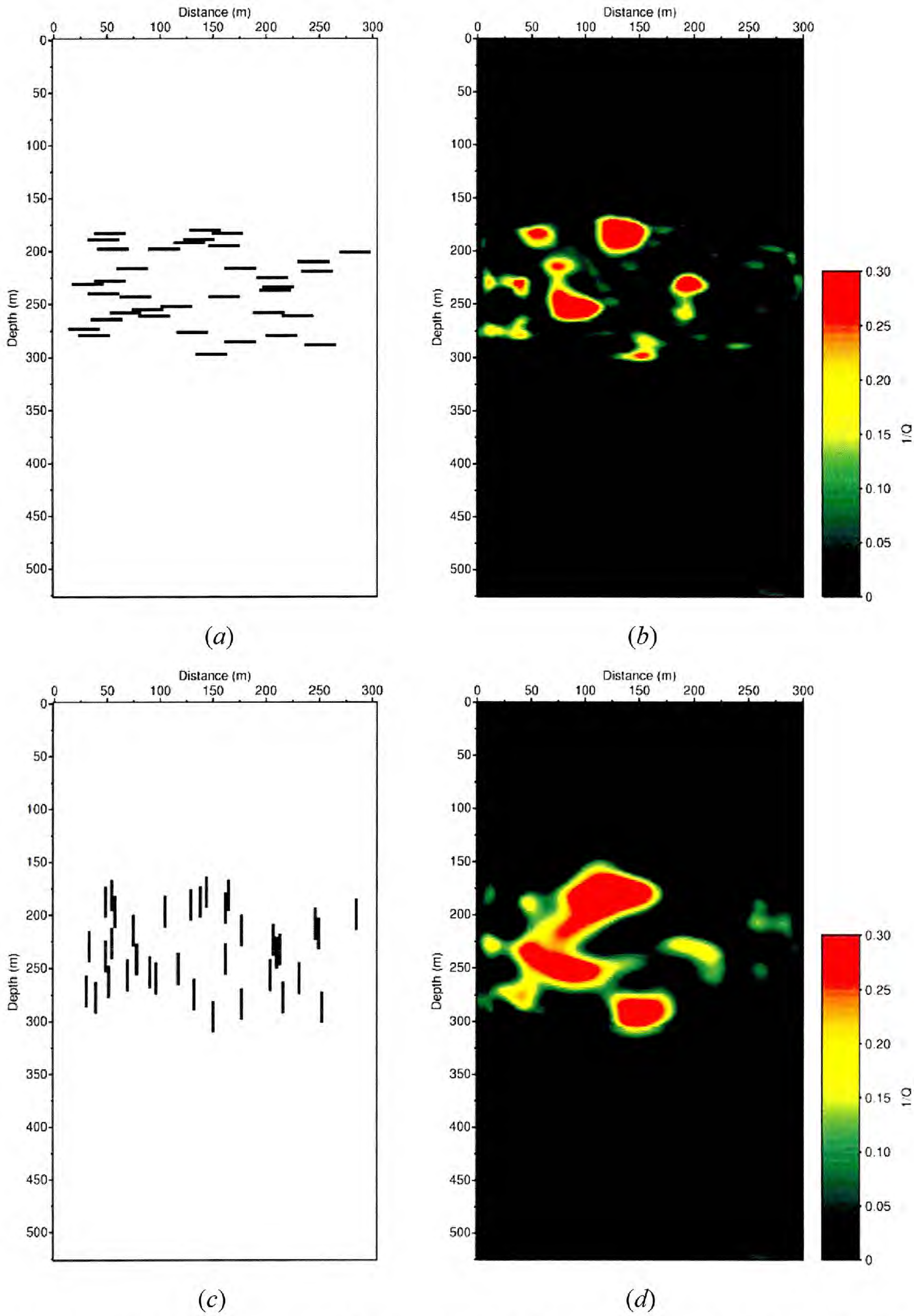

Figure 6.11 (a) Fracture model with vertical fractures of length 30 m. (b) The attenuation model reconstructed by waveform tomography. (c) Fracture model with horizontal fractures of length 30 m. (d) The attenuation model reconstructed by waveform tomography.

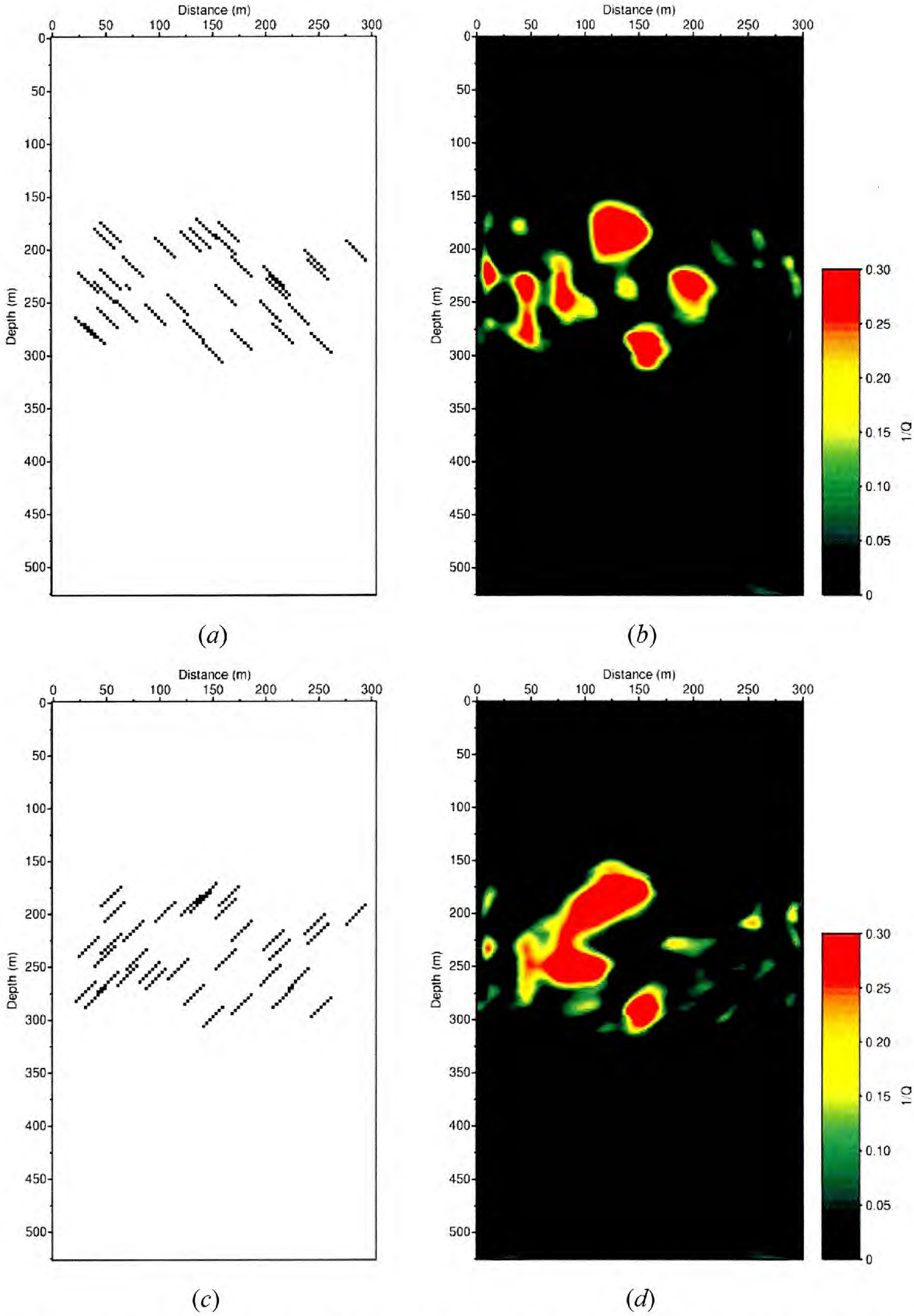

Figure 6.12 (a) Fracture model with orientation 45° and length 30 m. (b) The attenuation model reconstructed by waveform tomography. (c) Fracture model with orientation 135° and length 30 m. (d) The attenuation model reconstructed by waveform tomography.

Chapter 7

Conclusions and future work

7.1 Conclusions

The main aim of this PhD project is to investigate the application of waveform tomography to real seismic data to obtain high resolution results.

As the real crosshole seismic data do not include frequencies less than 200 Hz, a reliable initial estimate is important for frequency-domain waveform tomography. I use traveltime tomography to generate such a reliable model. In chapter 2, I have addressed three issues of traveltime tomography for dealing with real crosshole seismic data: how to suppress the effect of data errors, how to balance the data contribution and the *à priori* model in the objective function, and how to include well log velocity information as geological constraints in the inversion. I have used the conventional data covariance matrix, explicitly defined as a data confidence matrix in terms of the vertical offset of source and receiver, to suppress the effect of the first arrival picking errors. To control the balance in the inversion, I have used a normalizing factor systematically to make the choice of trade-off parameter meaningful. I have also included well log information as geological constraints in the inversion, in which I want to make sure that the structural details in the final result of traveltime tomography is unbiased by any strong constraints, This traveltime inversion result can then be used as initial model for waveform tomography.

In Chapter 3, I have addressed issues of waveform tomography in dealing with real crosshole seismic data. I have analyzed and verified that the following three issues are important for real data waveform tomography, compared to waveform tomography of synthetic data or traveltime tomography on both synthetic and real data. First, a good initial model can effectively compensate for the low frequency components, missing in the real data. It is essential for the success of waveform tomography. Second, a smoothness constraint is essential to combat the effect of data noise, the effect of uneven distribution of ray density, the effect of the strong sensitivity to short wavelengths of the velocity model and the non-linearity of the problem. Inverting a group of frequencies simultaneously at each inversion stage is necessary to further mitigate the effect of data noise. I have used the sonic log information as a geological constraint in the inversion. The result, without the sonic log information constraint, is similar to that using sonic log information as a geological constraint in the inversion, which indicates the reliability of waveform inversion without the well-log constraint.

In chapter 4, to quantitatively assess the reliability of waveform tomography results, I have conducted a series of checkerboard tests. These checkerboard tests provide an indication of the degree of confidence in the waveform tomography results. First, I designed a series of checkerboard tests to test the effect of the reference-model constraint and the smoothness constraint in the waveform tomography. I show that the resolvability can be further improved with regular source/receiver geometry. With the source/receiver geometry, in which lots of sources and receivers are missing, I can obtain an optimal solution by using both constraints first and then relaxing the smoothness constraint at later iterations, as demonstrated by the resolvability analysis. These tests also reveal that we need to consider both anomaly wavelength and amplitude when we discuss the resolution. For a fixed perturbation rate, longer-wavelength variations are better recovered. When the velocity perturbation is greater, the smallest anomaly size that can be well-recovered also increases. Guided by these checkerboard tests and resolvability analyses, the features in the waveform tomography results can be confidently used in the geological and lithological interpretation.

In chapter 5, I use waveform tomography to invert for not only the velocity model but also the attenuation model. Because the magnitude of the attenuation factor is of order 0.01, a starting attenuation factor model with constant value 0, is a safe choice for waveform inversion. In working with real data case, it is best to invert for real-part velocity model, fixing the attenuation factor model first, and then fixing the real-part velocity model to invert for the attenuation model. Because the real part velocity and attenuation factor have different weights of contribution in the objective function, the strategy of fixing one model and inverting for the other model can successfully avoid the effect of the trade-off of errors between the two different parameter types.

In chapter 6, I use waveform tomography to investigate the attenuation effects caused by distributed fractures. I have shown that strong attenuation positions closely correspond to the region of high fracture density. When the fracture size is smaller than the wavelength, the characters of attenuation are elliptical. The apparent attenuation factor is sensitive to both fracture length and fracture orientations. When the length of the fractures increases, the attenuation is enhanced. When the fractures are parallel to the source/receiver string, they act as small reflecting surfaces in seismic response. This orientation shows the strongest attenuation in the results of waveform tomography. Whereas when fractures are perpendicular to the source/receiver string, they act as scattering points in the seismic response and show the weakest apparent attenuation in the results of waveform tomography.

7.2 Future work

In the above chapters I have obtained some encouraging results. I have found that there are still some works that should be done to develop the waveform tomography:

(a) Use waveform tomography to qualitatively investigate fracture response

The frequency-domain tomography method can be easily extended to take account of attenuation. The attenuation image can be used in turn to estimate fracture characteristics. Certain regions of low Q may be due to an increased density of fracturing, and these regions may also have acted as gas migration pathways. In chapter 6, I use waveform inversion to investigate seismic response in fractured media, by for inverting attenuation factor Q. Here, I show some promising results that indicate the relationship between apparent attenuation factor measured in crosshole tomography and fracture length and orientation. The other direction in the future work is to reduce the harmful effect of parameter trade-off in the objective function and realize to qualify the accuracy of attenuation factor inversion. In chapter 6, I test the examples in crosshole geometry. Examples in surface acquisition geometry should also be further tested.

(b) Elastic waveform tomography

To model the physical properties of the solution domain more realistically, the elastic waveform tomography is a direction. By using the elastic wave equation, we can see more complete wave phenomena, such as shear-wave events etc.. It can help us better understand the seismic response, properly account for shear waves, mode conversions and multi-component data, and to incorporate the effects of anisotropy and attenuation.

Forward modeling is a useful tool to predict the seismic response for interpretation. It also is an essential step for waveform tomography. An efficient fourth-order finite difference method to model the elastic wave equation in two dimensions has been developed by Virieux (1986) and Levander (1988). In this method, a staggered grid method is used. Two particle velocity components and three stress components are solved simultaneously. It is stable for all value of Poisson's ratio. It is also suitable for the liquid/solid interface. Figure 7.1 shows an example of wave propagation through a transversely isotropic medium, using the staggered grid method, with the elastic constants $c_{11} = 28.60$ Gpa, $c_{33} = 18.09$ Gpa, $c_{13} = 9.90$ Gpa, $c_{55} = 4.40$ Gpa, $c_{15} = c_{35} = 0.00$ Gpa, and $\rho = 1.95 \times 10^3$ kg/m^3. Figure 7.2 shows an example of wave propagation through an anisotropic medium, for which the six non-zero elastic coefficients $c_{11} = 28.60$ Gpa, $c_{33} = 18.09$ Gpa, $c_{13} = 9.90$ Gpa, $c_{55} = 4.40$ Gpa, $c_{15} = 1.80$ Gpa, $c_{35} = 2.30$ Gpa, and $\rho = 1.95 \times 10^3$ kg/m^3. In Figure 7.2, we can see the qP-wave front clearly; the qSV-wave front is crossed like four triangles, two of which propagate along the symmetry axis, and the two others in the perpendicular direction. These calculations are done in the time domain. Štekl and Pratt (1998) presented a viscoelastic model based on the frequency-domain finite differences method. Two coupled integro-differential equations have been used in this method. Only two particle velocity components are solved simultaneously in these equations. With this improvement, only two unknowns need to be solved simultaneously. Compared to the staggered-grid method in which five unknowns should be solved, this method effectively saves storage and calculation expense. To improve the accuracy and save the storage, the rotated operator and lumped mass terms have been used in this method. In this method, the integral term is represented using complex-valued elastic media properties. This method performs better than the standard second-order scheme for a wide range of Poisson ratios by some simulating shear wave propagation examples in liquid layers. By comparing real crosshole seismic data and synthetic model data they interpret the coda in seismic data in term of the generation of mode-converted shear waves within the complicated, finely layered sediments at the site.

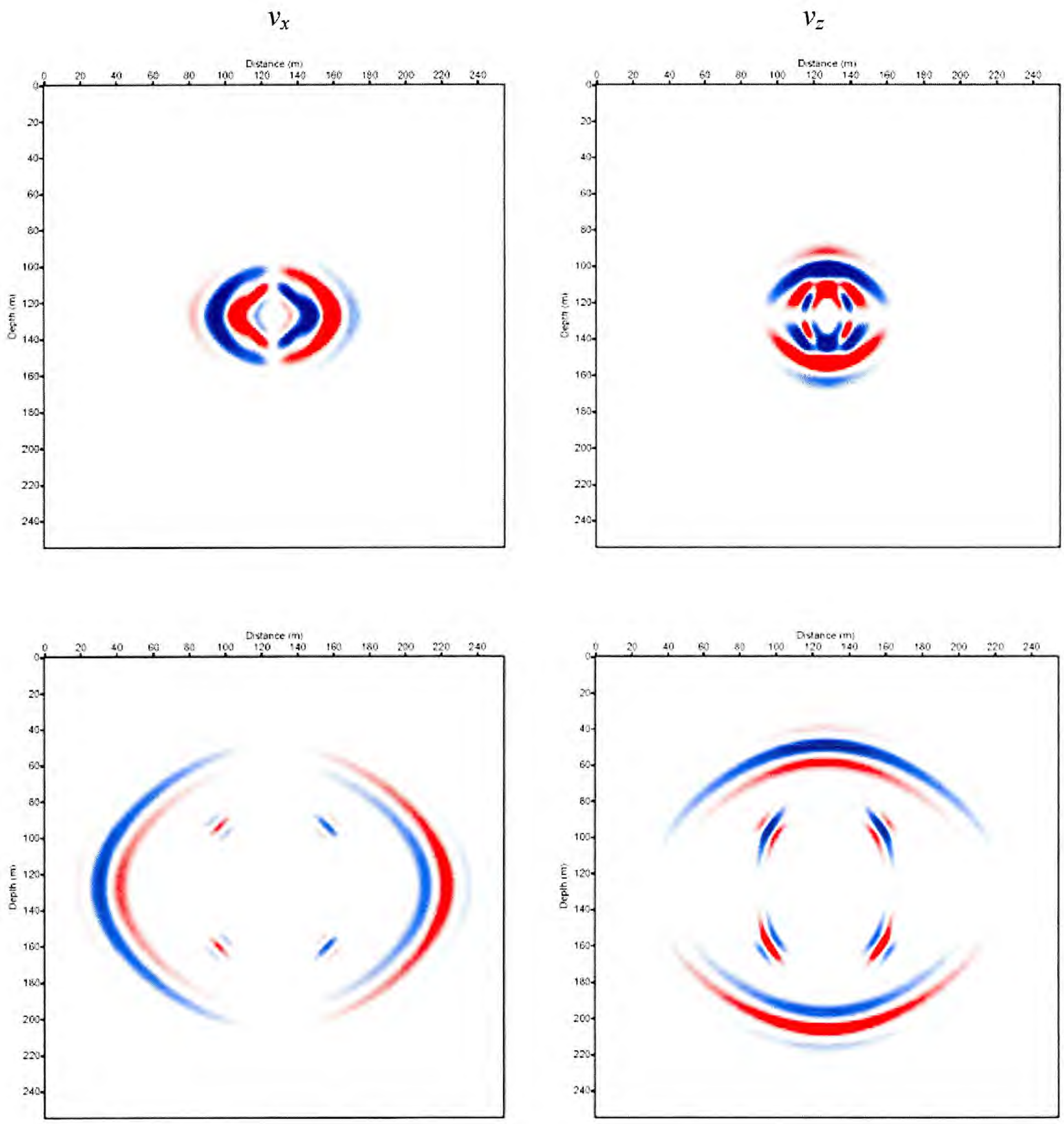

Figure 7.1 Snapshot of wave propagation in the transversely isotropic medium at different time. The elastic constants $c_{11} = 28.60$ Gpa, $c_{33} = 18.09$ Gpa, $c_{13} = 9.90$ Gpa, $c_{55} = 4.40$ Gpa, $c_{15} = c_{35} = 0.00$ Gpa, and $\rho = 1.95$ kg/m^3.

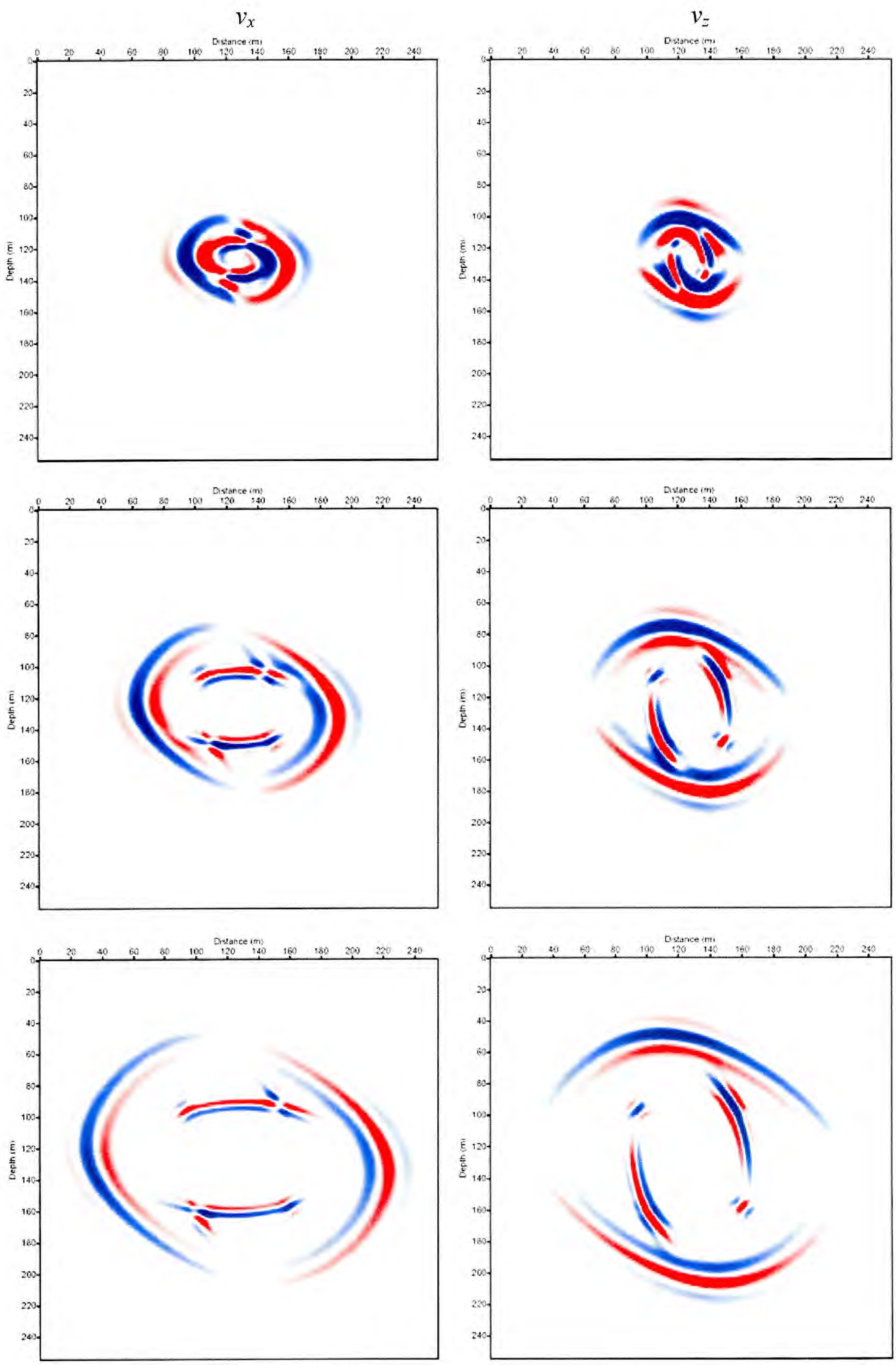

Figure 7.2 Snapshot of wave propagation in the anisotropic medium at different time. The six non-zero elastic coefficients $c_{11} = 28.60$ Gpa, $c_{33} = 18.09$ Gpa, $c_{13} = 9.90$ Gpa, $c_{55} = 4.40$ Gpa, $c_{15} = 1.80$ Gpa, $c_{35} = 2.30$ Gpa, and $\rho = 1.95$ kg/m^3.

By using the elastic wave equation, we can use S-wave information instead of treating it as undesirable noise, as when using the acoustic wave equation in waveform inversion. Tarantola *et al.* (1986) and Mora (1987) build the theoretical framework for elastic waveform inversion, where they have shown a method to calculate the gradients by using the perturbation solution of the elastic wave equation. Zhou et al. (1997) invert for both P- and S-velocity distributions in crosshole geometry by using the elastic waveform inversion method. Sears et al. (2007) demonstrate the potential of elastic waveform inversion for reservoir characterization in wide-angle multi-component ocean-bottom cable (OBC) geometry. They show very promising results on inversion of P-wave data, which contain both P- and S-wave velocity information.

For the elastic waveform tomography, further research could explore the effect of attenuation, anisotropy and incorporate the effect in the elastic waveform inversion method. Properly using PS-wave to improve resolution of waveform inversion result is another direction for further investigation. In the case of real data, the accuracy of the estimated source wavelet depends on the accuracy of the velocity model. Errors in the estimate of the source wavelet function may bring large artifacts in the waveform inversion. Hence it is also a direction for further investigation. The most elastic waveform calculations are executed in time domain, more work on elastic waveform inversion could be done in frequency domain using the two coupled integro-differential equations I mentioned in this section, since it has advantages I mentioned in chapter 1.

(c) Surface seismic data waveform tomography on target area

Surface seismic surveying is commonly used to image sub-horizontal structures in the hydrocarbons industry. Although the disadvantage of seismic data in this geometry is that waveform, amplitude and traveltimes are distorted by velocity variations, waveform inversion can also be applied to surface seismic data. Pratt *et al.* (1996) have used wide-angle refraction energy in this geometry to reconstruct a velocity model. A synthetic test, based on a real crustal data set collected over the Basin and Range province in south-western USA, has illustrated the potential of frequency domain waveform inversion for providing high resolution near-surface velocity models.

Once a high-resolution near-surface velocity image is obtained, a further research direction is to improve the resolution at greater depth by using reflection energy in seismic data. One strategy is to redefine a reference surface for wave-equation datuming. Wave-equation datuming is the name given to upward or downward continuation of seismic time data when the purpose is to redefine the reference surface on which the source and receivers appear to be located. Berryhill (1984) extended this concept from stacked data to pre-stacked data. Unlike datuming with static shifts, wave-equation datuming moves sources and receivers-and so corrects for traveltimes-in a manner consistent with wave equation theory. The normal application for this technique is to remove near-surface velocity variations or topography effects that adversely affect the continuity and time structure of subsurface reflectors. Berryhill (1984) presented the result of moving the source-receiver plane from see a level to a datum plane coincident with the sea floor. Then Bevc (1997) upward continued land data with rugged acquisition topography to a flat datum at elevation above the topography surface. Francesca and Christopher (2002) dealt with irregular subbasalt interfaces at depth, using similar method

However, for frequency domain waveform inversion, the critical problem is to effectively use reflection information and avoid the effect of strong refraction energy in this step.

Further work in this direction will concern (1) further reducing computing and storage expense; (2) investigate the combined use of direct and iterative solvers (Ben Hadj Ali et al. 2007); (3) further investigating the practical application in real datasets.

References

Aki K. and Richards P.G. 1980. *Quantitative seismology: theory and methods.* W. H. Freeman., San Francisco.

Alford R.M., Kelly K.R. and Boore D.M. 1974. Accuracy of finite-difference modelling of the acoustic wave equation. *Geophysics* **39**, 834-842.

Alkhalifah T. 2002. Traveltime computation with the linearized eikonal equation for anisotropic media. *Geophysical Prospecting* **50**, 373-382.

Alterman Z.S. and Karal F. 1968. Propagation of elastic waves in layered media by finite-difference methods. *Bulletin of the Seismological Society of America* **58**, 367-398.

Ben Hadj Ali H., Operto S., Virieus J., Amestoy P. L'Excellent J.Y. and Giraud L. 2007. 3D finite-difference frequency-domain modelling of acoustic wave propagation using a massively parallel direct solver. 69th Conference of the European Association of Geoscientists & Engineers, London, UK, C027.

Berenger J. P. 1994. A perfectly matched layer for the absorption of electromagnetic waves. *Journal of Computational Physics* **114,** 185-200.

Bergman B., Tryggvason A. and Juhlin C. 2004. High-resolution seismic traveltime tomography incorporating static corrections applied to a till-covered bedrock environment. *Geophysics* **69,** 1082-1090.

Berryhill J. R. 1984. Wave equation datuming before stack. *Geophysics,* **49**, 2064-2066.

Berryman J.G. 1989. Weighted least-squares criteria for seismic traveltime tomography. *IEEE Transactions on Geoscience and Remote Sensing* **27,** 302-309.

Bevc D. 1997. Flooding the topography: Wave equation datuming of land data with rugged acquisition topography. *Geophysics,* **62**, 1558-1569.

Beydoun W.B. and Mendes M. 1989. Elastic ray-born l_2 migration/inversion. *Geophysical Journal International* **97**, 151-160.

Bording R.P., Gersztenkorn A., Lines L.R., Scales J.A. and Treitel S. 1987. Applications of seismic traveltime tomography. *Geophysical Journal of the Royal Astronomical Society* **90,** 285-303.

Bregman N.D., Chapman C.H. and Bailey R.C. 1989. Crosshole seismic tomography, *Geophysics,* **54**, 200-215.

Brenders A.J. and Pratt R.G. 2007. Efficient waveform tomography for lithospheric imaging: implications for realistic, two-dimensional acquisition geometries and low-frequency data. *Geophysical Journal International* **168**, 133–151.

Bunks C., Saleck F.M., Zaleski S. and Chavent G. 1995. Multiscale seismic waveform inversion. *Geophysics,* **60**, 1457-1473.

Cao D., Beydoun W.B., Singh S.C. and Trantola A. 1990. A simultaneous inversion for background velocity and impedance maps. *Geophysics* **55,** 458-469.

Cerjan C., Kosoloff D., Kosoloff R. and Rashef M. 1985. Anonreflecting boundary condition for discrete acoustic and elastic wave equation. *Geophysics* **50**, 705-708.

Chapman C.H. and Pratt R.G. 1992. Traveltime tomography in anisotropic media-I. Theory. *Geophysics Journal International* **109**, 1-19.

Charara M., Barnes C. & Tarantola A., 2000. Full waveform inversion of seismic data for a viscoelastic medium, in *Methods and Applications of Inversion, Lecture Notes in Earth Sciences,* **92**, Springer-Verlag.

Clayton R. and Engquist B. 1977. Absorbing boundry conditions for acoustic and elastic wave equations. *Bulletin of the Seismological Society of America* **67**, 1529-1540.

Coates R. T. and Schoenberg M., 1995. Finite-difference modelling of faults and fractures. *Geophysics,* **60**, 1514-1526.

Dines K.A. and Lytle R.J. 1979. Computerised geophysical tomography. *Proceedings of the IEEE* **67**, 471-480.

Francesca M. and Christopher J. B. 2002. Interface scattering versus body scattering in subbasalt imaging and application of prestack wave equation datuming. *Geophysics,* **67**, 1593-1601.

Gersztenkorn A., Bednar J.B. and Lines L.R. 1986. Robust iterative inversion for the one-dimensional acoustic wave equation. *Geophysics* **51**, 357-368.

Gilbert P. 1972. Iterative methods for three-dimensional reconstruction of an object from projections. *Journal of Theoretical Biology* **36**, 105-117.

Hastings F.D., Schneider J.B. and Broschat S.L. 1996. Application of the perfectly matched layer (PML) absorbing boundary condition to elastic wave propagation. *Journal of the Acoustical Society of America* **100,** 3061–3069.

Herman G.T., Lent A. and Rowland S.W. 1973. ART: mathematics and applications. A report on the mathematical foundations and on the applicability to real data of the Algebraic Reconstruction Technique. *Journal of Theoretical Biology* **42**, 1-33.

Hicks G. and Pratt R.G. 2001. Reflection waveform inversion using local descent methods: estimating attenuation and velocity over a gas-sand deposit, *Geophysics,* **66,** 598-612.

Hong T.K. and Kennett B.L.N. 2004. Scattering of elastic waves in media with a random distribution of fluid-filled cavities: theory and numerical modelling. *Geophysical Journal International,* **159**, 961-977.

Hudson J.A. 1981. Wave speeds and attenuation of elastic waves in material containing cracks. *Geophysical Journal of the Royal Astronomical Society,* **64**, 133-150.

Inoue H., Fukao Y., Tanabe K. and Ogata Y. 1990. Whole mantle P-wave traveltime tomography, *Physics of the Earth and Planetary Interiors,* **59**, 294-328.

Ivansson S. 1983. Remark on an earlier iterative tomographic algorithm. *Bulletin of the Seismological Society of America* **75**, 855-860.

Juhlin C. 1995. Finite-difference elastic wave propagation in 2D heterogeneous transversely isotropic media. *Geophysical Prospecting* **43,** 843-858.

Kachanov M. 1993. Elastic solids with many cracks and related problems. *Advances in applied mechanics,* **30,** 259-445.

Kerner C. 1990. Modelling of soft sediments and liquid-solid interfaces: modified wavenumber summation method and application. *Geophysical Prospecting* **38,** 111-137.

Komatitsch D. and Tromp J. 2003. A perfectly matched layer absorbing boundary condition for the second-order seismic waveequation. *Geophysics International Journal* **154,** 146-153.

Lailly P. 1984. The seismic inverse problem as a sequence of before stack migrations. Conference on Inverse Scattering, Tulsa, Oklahoma: Philadelphia, SIAM.

Levander A.R. 1988. Fourth-order finite-difference P-SV seismogram. *Geophysics* **53,** 1425–1436.

Liao Q. and McMechan G.A. 1996. Multifrequency viscoacoustic modeling and inversion. *Geophysics* **61**, 1371–1378.

Liu E., Hudson J. A. and Pointer T., 2000. Equivalent medium representation of fractured rock. *Journal of Geophysical Research*, **105(B2)**, 2981-3000.

Luo Y. and Schuster G.T. 1991. Wave equation traveltime inversion. *Geophysics* **56**, 645-653.

Lytle R.J. and Dines K.A., 1980. Iterative ray tracing between boreholes for underground image reconstruction. *IEEE Transactions on Geoscience and Romote Sensing*, **GE-18**, 234-240

Marfurt K.J. 1984 Accuracy of finite-difference and finite-element modeling of the scalar and elastic wave-equations. *Geophysics*, **49**, 533-549.

Mason I. 1981. Algebraic reconstruction of a two-dimensional velocity inhomogeneity in the High Hazle seam of Thoresby colliery. *Geophysics* **46**, 298-308.

McMechan G.A., 1983. Seismic tomography in boreholes, *Geophysical Journal of the Royal Astronomical Society*, **74**, 601-612.

Mora P.R. 1987. Nonlinear two-dimensional elastic inversion of multioffset seismic data. *Geophysics* **52**, 1211-1228.

Mora P.R. 1989. Inversion = migration + tomography. *Geophysics* **12**, 1575-1586.

Morgan J.V., Christeson G.L. and Zelt C.A., 2002. Testing the resolution of a 3D velocity tomogram across the Chicxulub crater, *Techtonophysics*, **355**, 215-226.

Peterson J.E., Paulsson B.N.P. and McEvilly T.V. 1985. Applications of algebraic reconstruction techniques to crosshole seismic data. *Geophysics* **50**, 1566–1580.

Pratt R.G. 1990a. Frequency domain elastic wave modelling by finite differences: a tool for crosshole seismic imaging, *Geophysics*, **55**, 626-632.

Pratt R.G. 1990b. Inverse theory applied to multi-source crosshole tomography I: acoustic wave-equation method. *Geophysical Prospecting* **38**, 287–310.

Pratt R.G. 1999. Seismic waveform inversion in the frequency domain, Part 1: Theory and verification in a physical scale model, *Geophysics*, **64**, 888-901.

Pratt R.G. and Worthington M.H. 1990. Inverse theory applied to multisource cross-hole tomography. Part I: Acoustic wave-equation method. *Geophysical Prospecting* **38**, 287-310.

Pratt R.G. and Goulty N.R. 1991. Combining wave equation imaging with traveltime tomography to form high resolution images from crosshole data. *Geophysics* **56**, 208-224.

Pratt R.G. and Chapman C.H. 1992. Traveltime tomography in anisotropic media--II. Application. *Geophysical Journal International* **109**, 20-37.

Pratt R. G., Song Z. M., Williamson P. and Warner M. 1996. Two-dimensional velocity models from wide-angle seismic data by wavefield inversion. *Geophysical Journal International,* **124**, 323-340.

Pratt R. G., Shin C., and Hicks G. J. 1998. Gauss-Newton and full Newton methods in frequency-space seismic waveform inversion. *Geophysical Journal International,* **133**, 341-362.

Pratt R.G. and Shipp R.M. 1999. Seismic waveform inversion in the frequency domain, Part 2: Fault delineation in sediments using crosshole data. *Geophysics* **64**, 902–914.

Pratt R.G., Hou F., Bauer K. and Weber M. 2004. Waveform tomography images of velocity and inelastic attenuation from the Mallik 2002 crosshole seismic surveys, in *Scientific Results from the Mallik 2002 Gas Hydrate Production Research Well Program, Mackenzie Delta, Northwest Territories, Canada,* ed. Dallimore, S.R. & Collett ,T.S., *Geological Survey of Canada Bulletin,* **585**, 14p.

Qi Q. and Geers T.L. 1998. Evaluation of the perfectly matched layer for computational acoustics. *Journal of Computational Physics* **139,** 166–83.

Rao Y. and Wang Y. 2005. Crosshole seismic tomography: working solutions to issues in real data travel time inversion, *Journal of Geophysics and Engineering,* **2**, 139-146.

Ravaut C., Operto S., Improta L., Virieux J., Herrero A. and Dell'Aversana P. 2004. Multiscale imaging of complex structures from multifold wide-aperture seismic data by frequency-domain full-waveform tomography: application to a thrust belt, *Geophysical Journal International,* **159,** 1032–1056.

Röhm A.H.E., Bijwaard H., Spakman W. and Trampert J. 2000. Effects of arrival time errors on traveltime tomography. *Geophysical Journal International* **142,** 270-276.

Santosa F. 1987. Inversion of band-limited reflection seismo-grams using stacking velocities as constraints. *Inverse Problems* **3**, 477–499.

Scales J.A. 1987. Tomographic inversion via the conjugate gradient method. *Geophysics* **52**, 179-185.

Scales J.A, Gersztenkorn A. and Treitel S. 1988. Fast l_p Solution of large, sparse, linear systems: application to seismic traveltime tomography. *Journal of Computational Physics* **75,** 314-333.

Schoenberg M. 1980. Elastic wave behavior across linear slip interfaces. *Journal of the Acoustical Society of America*, **68(5)**, 1516–1521.

Sears T.J., Singh S.C. and Barton P.J. 2007. Elastic full waveform inversion of multi-component OBC seismic data-application to Alba field, UK central North Sea. 69th Conference of the European Association of Geoscientists & Engineers, London, UK, C031.

Sheen D.H., Tuncay K., Baag C.E. and Ortoleva P. J. 2006. Time domain Gauss-Newton seismic waveform inversion in elastic media. *Geophysical Journal International* **167,** 1373-1384.

Shin C. 1995. Sponge boundary condition for frequency-domain modeling. *Geophysics* **60**, 1870-1874.

Shin C. and Min D.J. 2006. Waveform inversion using a logarithmic wavefield. *Geophysics* **71**, R31-R42.

Shipp R.M. and Singh S.C. 2002. Two-dimensional full wavefield inversion of wide-aperture marine seismic streamer data. *Geophysical Journal International* **151,** 325–344.

Sirgue L. and Pratt R.G. 2004. Efficient waveform inversion and imaging: a strategy for selecting temporal frequencies and waveform inversion. *Geophysics* **69**, 231-248.

Slawinski M., Wheaton C. and Powojowski M. 2004. VSP traveltime inversion for linear inhomogeneity and elliptical anisotropy. *Geophysics* **69**, 373-377.

Song Z.M. and Williamson P.R. 1995. Frequency-domain acoustic wave modeling and inversion of crosshole data, part I, 2.5-D modeling method. *Geophysics* **60**, 784-795.

Song Z.M., Williamson P.R. and Pratt R.G. 1995. Frequency-domain acoustic wave modeling and inversion of crosshole data, part II, inversion method, synthetic experiments and real data results. *Geophysics* **60**, 796-809.

Snieder R. and Spencer C. 1993. An unified approach to ray bending, ray perturbation, paraxial ray theories. *Geophysical Journal International* **115**, 456–470.

Stacey R. 1988. Improved transparent boundary formulations for the elastic-wave equation. *Bull Seismic Society America* **78(6),** 2089-2097.

Štekl I. and Pratt R.G. 1998. Accurate visco-elastic modeling by frequency-domain finite differences using rotated operators. *Geophysics* **63**, 1779–1794.

Tarantola A. 1984. Inversion of seismic reflection data in the acoustic approximation. *Geophysics*, **49**, 1259-1266.

Tarantola A. 1986. A strategy for nonlinear elastic inversion of seismic reflection data. *Geophysics* **51**, 1893-1903.

Tarantola A. ans Valette J. 1982. Generalized nonlinear inverse problems solved using the least-squares criterion. *Reviews of Geophysics and Space Physics* **20,** 219-232.

Tarantola A. 2005. *Inverse problem Theory and methods for model parameter estimation.* Soc. for Industrial & Applied Maths. ISBN: 0898715725.

van Wijk K., Scales J.A., Navidi W. and Tenorio L. 2002. Data and model uncertainty estimation for linear inversion. *Geophysical Journal International* **149,** 625-32

Varela C.L., Stoffa P.L. and Sen M.K. 1996. Automatic background velocity estimation in 2D media. 58th Conference of the European Association of Geoscientists & Engineers. X009.

Virieux J. 1986. P-SV wave-propagation in heterogeneous media: velocity-stress finite-difference method. *Geophysics* **51**, 889-901.

Virieux J. and Farra V. 1991. Ray tracing in 3-D complex isotropic media: An analysis of the problem. *Geophysics* **56**, 2057–2069.

Vlastos S., Liu E., Main I.G. and Li X.Y. 2003. Numerical simulation of wave propagation in media with discrete distributions of fractures: effects of fracture sizes and spatial distributions. *Geophysical Journal International* **152,** 649-668.

Vlastos S., Liu E., Main I.G., Schoenberg M., Narteau C. and Li X.Y. 2006. Dual simulations of fluid flow and seismic wave propagation in a fractured network: effects of pore pressure on seismic signature. *Geophysical Journal International* **166,** 825-838.

Wang Y. 2002. A stable and efficient approach of inverse *Q* filtering, *Geophysics* **67,** 657-663.

Wang Y. 2003a. Quantifying the effectiveness of stabilized inverse *Q* filtering. *Geophysics* **68**, 337-345.

Wang Y. 2003b. *Seismic amplitude inversion in reflection tomography.* Pergamon Press. ISBN: 0080442439.

Wang Y. 2006. Inverse *Q* filter for seismic resolution enhancement. *Geophysics* **71**, no3, V51-V60.

Wang Y. and Houseman G.A. 1994. Inversion of reflection seismic amplitude data for interface geometry, *Geophysical Journal International* **117,** 92-110.

Wang Y, and Houseman G.A. 1995. Tomographic inversion of reflection seismic amplitude data for velocity variation, *Geophysical Journal International* **123,** 355-372.

Wang Y. and Pratt R.G. 1997. Sensitivities of seismic traveltimes and amplitudes in reflection tomography. *Geophysical Journal International* **131,** 618-642.

Wang Y. and Rao Y. 2006. Crosshole seismic waveform tomography, I: Strategy for real data application. *Geophysical Journal International*, **166**, 1237-1248.

Wang Y., White R.E. and Pratt R.G. 2000. Seismic amplitude inversion for interface geometry: practical approach for application. *Geophysical Journal International* **142,** 162-172.

Washbourne J., Rector J. and Bube K. 2002. Crosswell traveltime tomography in three dimensions. *Geophysics* **67**, 853-871.

Worthington M.H. 1984. An introduction to geophysical tomography. *First Break* **2,** 20-26.

Wu H. and Lees J.M. 1999. Cartesian parametrization of anisotropic traveltime tomography. *Geophysical Prospecting* **137**, 64–80.

Wu R., and Toksöz M.N., 1987. Diffraction tomography and multisource holography applied to seismic imaging, *Geophysics* **52,** 11-25.

Yoon K.H. and McMechan G.A. 1992. 3-D finite difference modeling of elastic waves in borehole environments. *Geophysics* **57**, 793-804.

Zelt C., 1998. Lateral velocity resolution from three-dimensional seismic refraction data, *Geophysical Journal International* **135**, 1101-1112.

Zelt C. and Barton P.J. 1998. Three-dimensional seismic refraction tomography: a comparison of two methods applied to data from the Faeroe basin, *Journal of Geophysical Research,* **103** (B4), 7187-7210.

Zhou C.X., Schuster G.T., Hassanzadeh S. and Harris J.M. 1997. Elastic wave equation traveltime and waveform inversion of crosswell data. *Geophysics*, **62**, 853-868.

Zhou B. and Greenhalgh S.A. 2003. Crosshole seismic inversion with normalized full-waveform amplitude data. *Geophysics* **68,** 1320-1330.

Appendix A

Finite-difference elastic wave propagation

A.1 Finite-difference scheme

The linear elastodynamic equations in two dimensions are

$$
\begin{aligned}
&\rho\frac{\partial^2 u_x}{\partial t^2}=\frac{\partial \tau_{xx}}{\partial x}+\frac{\partial \tau_{xz}}{\partial z},\\
&\rho\frac{\partial^2 u_z}{\partial t^2}=\frac{\partial \tau_{xz}}{\partial x}+\frac{\partial \tau_{zz}}{\partial z},\\
&\tau_{xx}=c_{11}\frac{\partial u_x}{\partial x}+c_{13}\frac{\partial u_z}{\partial z}+c_{15}\left(\frac{\partial u_x}{\partial z}+\frac{\partial u_z}{\partial x}\right),\\
&\tau_{zz}=c_{13}\frac{\partial u_x}{\partial x}+c_{33}\frac{\partial u_z}{\partial z}+c_{35}\left(\frac{\partial u_x}{\partial z}+\frac{\partial u_z}{\partial x}\right),\\
&\tau_{xz}=c_{15}\frac{\partial u_x}{\partial x}+c_{35}\frac{\partial u_z}{\partial z}+c_{55}\left(\frac{\partial u_x}{\partial z}+\frac{\partial u_z}{\partial x}\right).
\end{aligned}
\tag{A-1}
$$

where (u_x, u_z) is the displacement vector, and $(\tau_{xx}, \tau_{zz}, \tau_{xz})$ is the stress tensor. In these equations, $\rho(x,z)$ is the density, and c_{11}, c_{13}, c_{15}, c_{33}, c_{35}, c_{55} are the six elastic constants relating stress to strain, for the two dimensional cases.

The linear elastodynamic equations can be transformed into the following first-order hyperbolic system as

$$
\begin{aligned}
&\rho\frac{\partial v_x}{\partial t}=\frac{\partial \tau_{xx}}{\partial x}+\frac{\partial \tau_{xz}}{\partial z},\\
&\rho\frac{\partial v_z}{\partial t}=\frac{\partial \tau_{xz}}{\partial x}+\frac{\partial \tau_{zz}}{\partial z},\\
&\frac{\partial \tau_{xx}}{\partial t}=c_{11}\frac{\partial v_x}{\partial x}+c_{13}\frac{\partial v_z}{\partial z}+c_{15}\left(\frac{\partial v_x}{\partial z}+\frac{\partial v_z}{\partial x}\right),\\
&\frac{\partial \tau_{zz}}{\partial t}=c_{13}\frac{\partial v_x}{\partial x}+c_{33}\frac{\partial v_z}{\partial z}+c_{35}\left(\frac{\partial v_x}{\partial z}+\frac{\partial v_z}{\partial x}\right),\\
&\frac{\partial \tau_{xz}}{\partial t}=c_{15}\frac{\partial v_x}{\partial x}+c_{35}\frac{\partial v_z}{\partial z}+c_{55}\left(\frac{\partial v_x}{\partial z}+\frac{\partial v_z}{\partial x}\right).
\end{aligned}
\tag{A-2}
$$

where (v_x, v_z) is the velocity vector: $v_x = \partial u_x / \partial t$, $v_z = \partial u_z / \partial t$.

If $c_{15} = c_{35} = 0$ and $c_{11} = c_{33}$, the elastic constants express the special case of an isotropic medium:

$$\begin{bmatrix} c_{11} & c_{13} & c_{15} \\ c_{13} & c_{33} & c_{35} \\ c_{15} & c_{35} & c_{55} \end{bmatrix} = \begin{bmatrix} (\lambda+2\mu) & \lambda & 0 \\ \lambda & (\lambda+2\mu) & 0 \\ 0 & 0 & \mu \end{bmatrix}, \tag{A-3}$$

where λ and μ are Lamé coefficients.

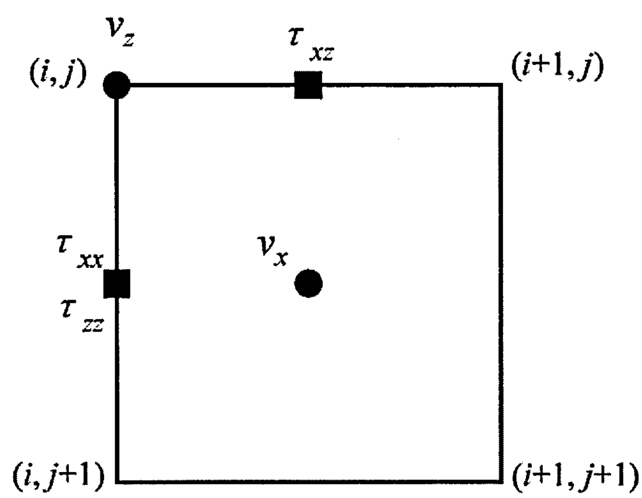

Figure A.1 Location of discretized variables on finite-difference cells. The cells are formed by four staggered grids with the normal stresses τ_{xx}, τ_{zz} defined on the same grid.

The variables $v_x, v_z, \tau_{xx}, \tau_{zz}, \tau_{xz}$ can be solved by using a staggered-grid approach (Levander, 1988). The locations for the variables $v_x, v_z, \tau_{xx}, \tau_{zz}, \tau_{xz}$ are uniquely defined for each cell as shown in Figure A.1.

Using the derivative operators D_{x+}, D_{x-}, D_{z+} and D_{z-} for the variables $v_x, v_z, \tau_{xx}, \tau_{zz}, \tau_{xz}$, the finite-difference scheme of equations (A-2) can be expressed as

$$
\begin{aligned}
v_x^{(\ell+1/2)}(i+\tfrac{1}{2},j+\tfrac{1}{2}) &= v_x^{(\ell-1/2)}(i+\tfrac{1}{2},j+\tfrac{1}{2}) \\
&\quad + \frac{\Delta t}{\rho}\Big[D_{x+}[\tau_{xx}^{(\ell)}(i,j+\tfrac{1}{2})] + D_{z+}[\tau_{xz}^{(\ell)}(i+\tfrac{1}{2},j)]\Big], \\
v_z^{(\ell+1/2)}(i,j) &= v_z^{(\ell-1/2)}(i,j) \\
&\quad + \frac{\Delta t}{\rho}\Big[D_{x-}[\tau_{xz}^{(\ell)}(i+\tfrac{1}{2},j)] + D_{z-}[\tau_{zz}^{(\ell)}(i,j+\tfrac{1}{2})]\Big], \\
\tau_{xx}^{(\ell+1)}\big(i,j+\tfrac{1}{2}\big) &= \tau_{xx}^{(\ell)}\big(i,j+\tfrac{1}{2}\big) \\
&\quad + \Delta t\Big[c_{11}D_{x-}[v_x^{(\ell+1/2)}(i+\tfrac{1}{2},j+\tfrac{1}{2})] + c_{13}D_{z+}[v_z^{(\ell+1/2)}(i,j)] \\
&\quad + c_{15}\Big(D_{z-}[v_x^{(\ell+1/2)}(i+\tfrac{1}{2},j+\tfrac{1}{2})] + D_{x+}[v_z^{(\ell+1/2)}(i,j)]\Big)\Big], \\
\tau_{zz}^{(\ell+1)}\big(i,j+\tfrac{1}{2}\big) &= \tau_{zz}^{(\ell)}\big(i,j+\tfrac{1}{2}\big) \\
&\quad + \Delta t\Big[c_{13}D_{x-}[v_x^{(\ell+1/2)}(i+\tfrac{1}{2},j+\tfrac{1}{2})] + c_{33}D_{z+}[v_z^{(\ell+1/2)}(i,j)] \\
&\quad + c_{35}\Big(D_{z-}[v_x^{(\ell+1/2)}(i+\tfrac{1}{2},j+\tfrac{1}{2})] + D_{x+}[v_z^{(\ell+1/2)}(i,j)]\Big)\Big], \\
\tau_{xz}^{(\ell+1)}\big(i+\tfrac{1}{2},j\big) &= \tau_{xz}^{(\ell)}\big(i+\tfrac{1}{2},j\big) \\
&\quad + \Delta t\Big[c_{15}D_{x-}[v_x^{(\ell+1/2)}(i+\tfrac{1}{2},j+\tfrac{1}{2})] + c_{35}D_{z+}[v_z^{(\ell+1/2)}(i,j)] \\
&\quad + c_{55}\Big(D_{z-}[v_x^{(\ell+1/2)}(i+\tfrac{1}{2},j+\tfrac{1}{2})] + D_{x+}[v_z^{(\ell+1/2)}(i,j)]\Big)\Big],
\end{aligned}
\tag{A-4}
$$

where the time derivative is a second-order approximation discretized at an interval of Δt. The derivative operators D_{x+}, D_{x-}, D_{z+} and D_{z-} are the forward and backward differences in the x- and z-directions. For example, the derivative operator D_{x+} is

$$
D_{x+}[v_z(i,j)] = \frac{1}{\Delta x}\left[-\frac{1}{24}v_z(i+2,j) + \frac{9}{8}v_z(i+1,j) - \frac{9}{8}v_z(i,j) + \frac{1}{24}v_z(i-1,j)\right].
\tag{A-5}
$$

Figure A.2 shows the active cells for updating all of the variables using fourth-order operators.

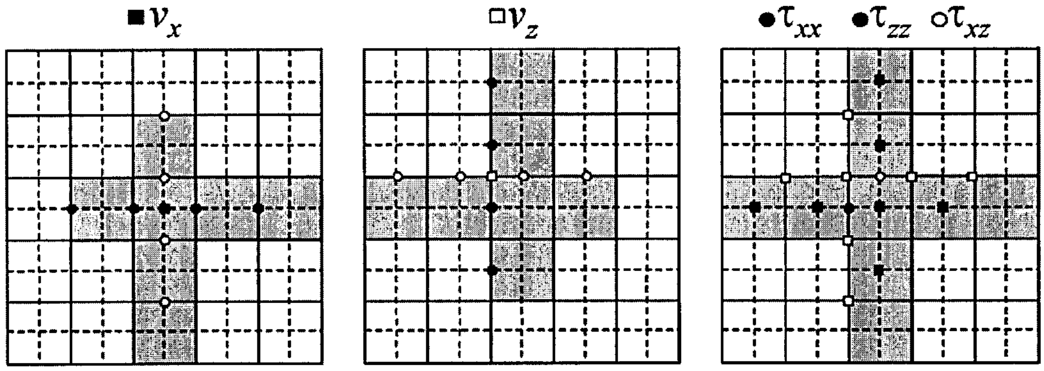

Figure A.2 Interaction and updating scheme for each discretized variable. Updated velocities are based upon the stress values in the shaded cells while the updated stresses use the velocity values in the shaded cells.

A.2 Boundary conditions

In limited-area numerical modelling of wave propagation in the earth, it is necessary to introduce artificial boundaries to keep computation down to a manageable size. These boundaries will cause significant reflection back toward the computational domain, as shown in Figure A.3.

In this simulation, a 250 × 250 m^2 region is discretized using a grid of 255×255 elements. The source time function is a Ricker wavelet with 20 Hz domain frequency, and is put at the middle point of the computational region. The *P*- and *S*-wave velocities are 3000 and 1730 m/s, corresponding to the elastic coefficients $c_{11} = 17.50$ Gpa, $c_{33} = 17.50$ Gpa, $c_{13} = 5.83$ Gpa, $c_{55} = 5.83$ Gpa, $c_{15} = c_{35} = 0.00$ Gpa, and $\rho = 1.95$ kg/m^3.

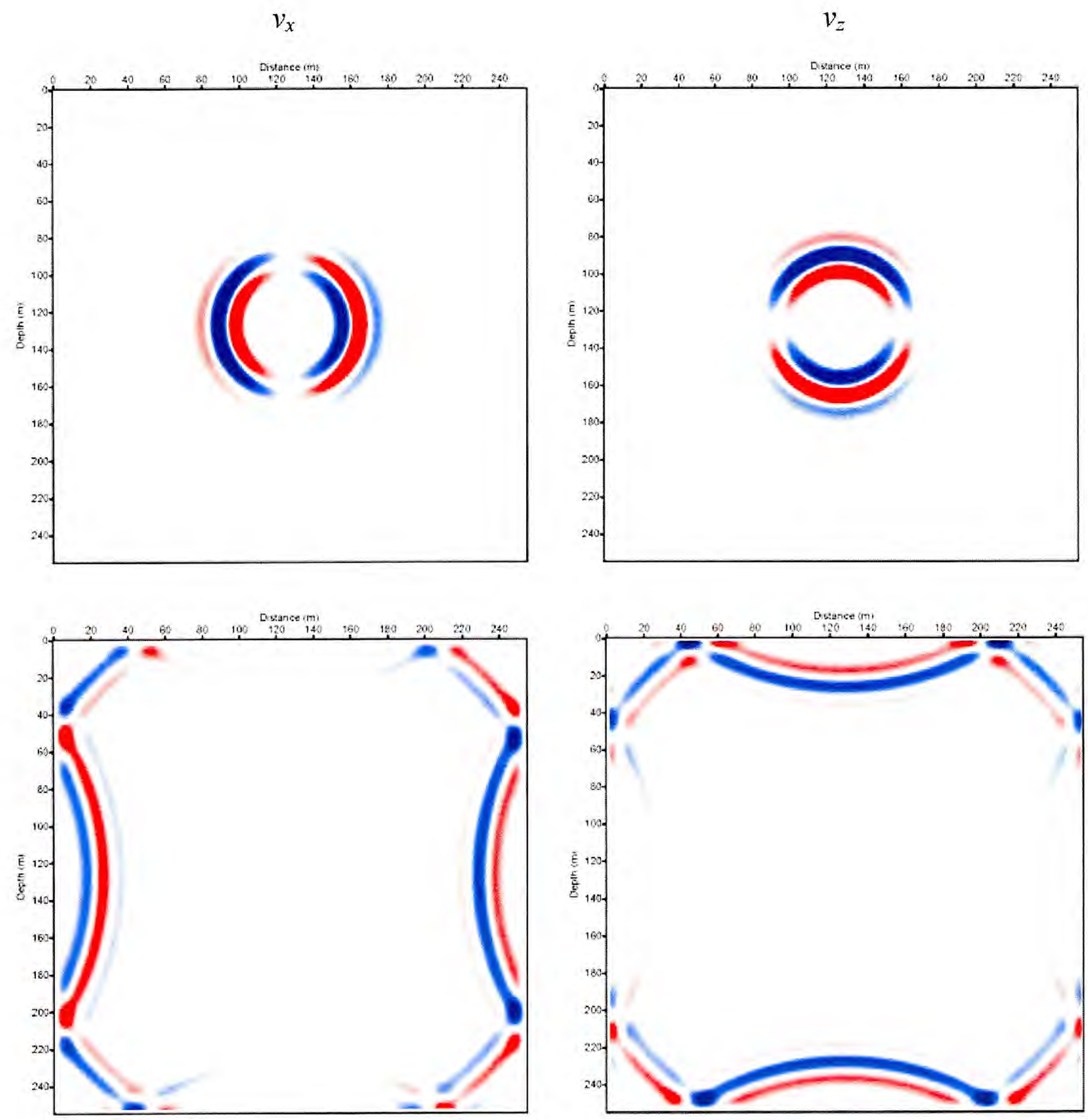

Figure A.3 Rigid boundary condition, which causes significant reflection back toward the computational domain, for an expanding circular scalar wave.

What we need is a solution near the boundary consisting of outgoing wave motions only. Therefore we need to set some boundary conditions that simulate the outward radiation of energy. Depending upon the problem, following boundary conditions can be used on the edges: absorbing boundary conditions for simulating an infinite medium, stress-free condition (free-surface), or zero-velocity conditions equivalent to zero-displacement conditions (rigid-surface) etc.

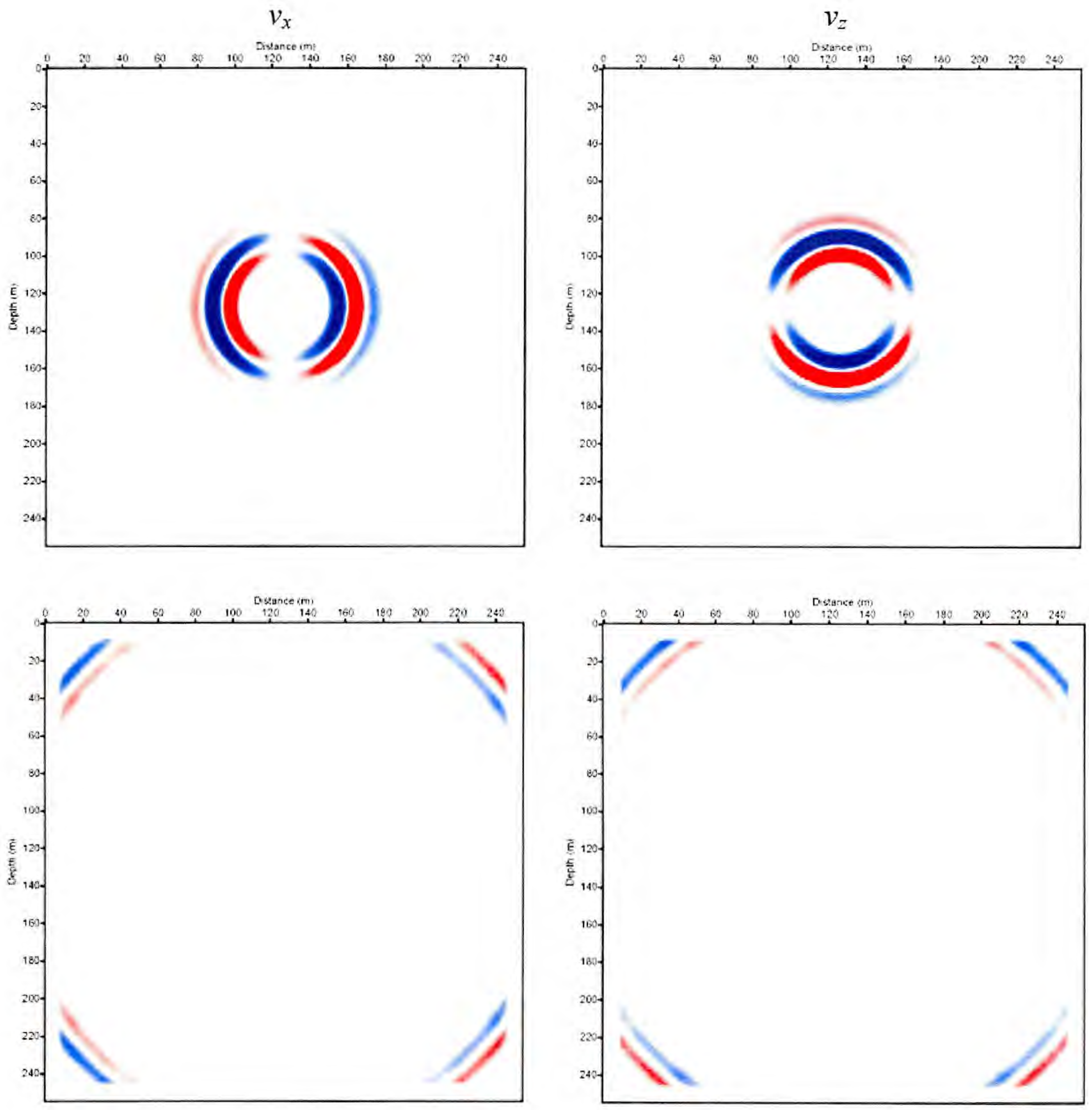

Figure A.4 Absorbing boundary condition, by tapering the normal and shear stress components over a thin strip along the boundary, for an expanding circular scalar wave.

A standard absorbing boundary condition is the radiation condition, which is the second-order condition, derived by Clayton and Engquist (1977) for elastic wave calculations involving two dimensions. This boundary condition is based on a paraxial approximation to the elastic wave equation, and radiation conditions may be satisfied explicitly (Clayton and Engquist, 1977; Stacey, 1988).

Marfurt (1984) and Cerjan *et al.* (1985) developed methods based on enlarging the computational domain, with the normal and shear stress components along the boundary tapered over a thin strip along the boundary (Cerjan *et al.,* 1985). The boundary strips used for tapering generally require a width of about 10 nodes, which results in less efficient use of memory. However, for anisotropic wave propagation, the radiation conditions become complex, and implementation becomes cumbersome, especially on parallel machines. Because of the ease of implementation, I chose a sponge boundary condition along those boundaries to absorb the incoming energy.

In figure A.3, the rigid boundary of the solution region acts as a perfect reflector. In figure A.4, the absorbing boundary conditions now allow both horizontal and vertical waves to pass through the grid perimeter without generating reflections.

For modelling a semi-infinite space, a free surface means that no normal or shear stresses are active. For a surface normal to the z -axis at $z = 0$,

$$\tau_{zz} = 0, \qquad \text{and} \qquad \tau_{xz} = 0. \tag{A-6}$$

Consistent with defining the normal stress on the top boundary, the two rows of fictitious nodes above the free surface boundary should be defined by making the normal stress anti-symmetric, to satisfy the following equations

$$\tau_{zz}(i,-1) = -\tau_{zz}(i,0), \qquad \text{and} \qquad \tau_{zz}(i,-2) = -\tau_{zz}(i,1). \tag{A-7}$$

At a stress-free boundary normal to the z -axis, the velocities are set to satisfy the following equations

$$\begin{aligned} c_{33}\frac{\partial v_z}{\partial z} + c_{35}\frac{\partial v_x}{\partial z} &= -\left(c_{35}\frac{\partial v_z}{\partial x} + c_{13}\frac{\partial v_x}{\partial x}\right), \\ c_{35}\frac{\partial v_z}{\partial z} + c_{55}\frac{\partial v_x}{\partial z} &= -\left(c_{55}\frac{\partial v_z}{\partial x} + c_{15}\frac{\partial v_x}{\partial x}\right). \end{aligned} \tag{A-8}$$

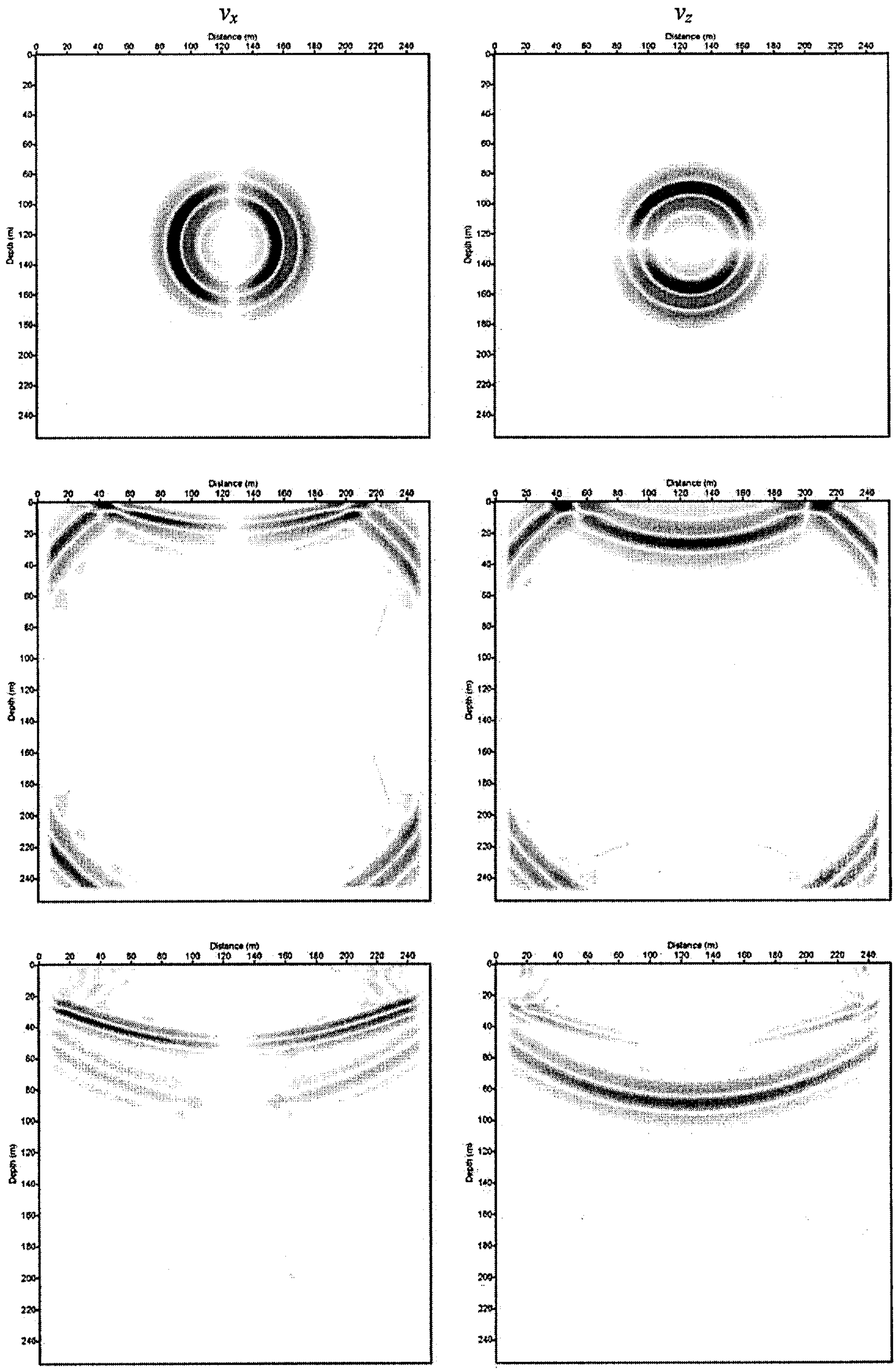

Figure A.5 A free-surface boundary condition defined on the top boundary, with the other three edge defined by absorbing boundary conditions as figure A.4, for an expanding circular scalar wave.

A.3 Initial conditions and source excitation

When time $t = 0$, stress and velocity are set to zero every where in the medium. Because of these initial conditions, propagating stress and velocity is also equivalent to propagating "time-integrated stress" and displacement (Virieux, 1986).

Alterman and Karal (1968) have solved source excitation. The excitation of any kind of source can be applied to velocity and stress. For an impulsive point source, which I used in the numerical simulations, the incident stress is obtained by convolving the infinite-medium Green's function with the source excitation as proposed by Alford *et al.* (1974). The convolution is obtained in the time domain. The impulsive excitation of a Ricker wavelet is

$$f(t) = \left(1 - 2\left(\frac{\pi f_d t}{2}\right)^2\right) e^{-\left(\frac{\pi f_d t}{2}\right)}, \tag{A-9}$$

where f_d controls domain frequency of the excitation.

A.4 Stability and dispersion properties

For homogeneous media, the numerical stability criterion is given by standard spectral analysis as

$$V_p \Delta t \sqrt{\frac{1}{\Delta x^2} + \frac{1}{\Delta z^2}} < 1, \tag{A-10}$$

where V_p is the P-wave velocity. For the special case $\Delta x = \Delta z$, the stability condition can be rewritten as

$$V_p \frac{\Delta t}{\Delta x} < \frac{1}{\sqrt{2}}. \tag{A-11}$$

The stability condition is independent of the S-wave velocity V_s, or of the elastic constants (Virieux, 1986).